ADVANCED L S

ACTIVITY REPORT 1997/98

March 1999
Ernest Orlando Lawrence Berkeley National Laboratory
University of California — Berkeley, California 94720

LBNL-43078

Available to DOE and DOE Contractors from the Office of Scientific and Technical Communication, P.O. Box 62, Oak Ridge, TN 37831.
Prices available from (615) 576-8401. Available to the public from the National Technical Information Service,
U.S. Department of Commerce, 5285 Port Royal Road, Springfield, VA 22161.

ADVANCED LIGHT SOURCE ACTIVITY REPORT 1997/98

March 1999
Ernest Orlando Lawrence Berkeley National Laboratory
University of California
Berkeley, California, 94720
LBNL-43078

This work was supported by the Director, Office of Science, Office of Basic Energy Sciences, Materials Sciences Division, of the U.S. Department of Energy under Contract No. DE-AC03-76SF00098.

Contents

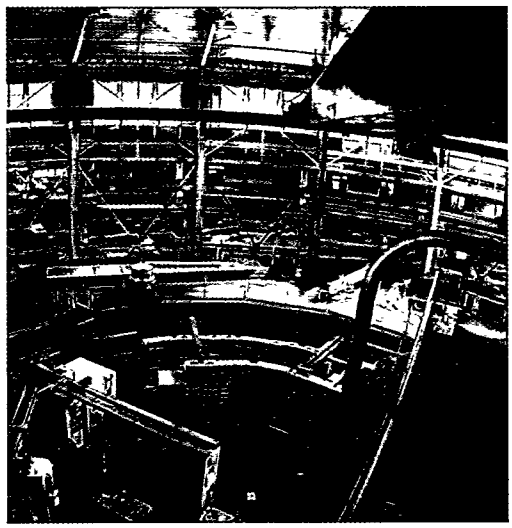

INTRODUCTION

Daniel Chemla
ALS Director

The Advanced Light Source has seen many changes and exciting developments in the 1997/98 period. First, the status of the ALS was elevated to that of a separate division within Berkeley Lab, and ALS management now reports directly to Laboratory Director Charles Shank. Second, Deputy Laboratory Director Pier Oddone was asked to head a task force to examine the user program at the ALS, compare it to the programs at other synchrotron radiation facilities, and recommend in its final report various improvements. Third, a very stimulating "Workshop on Scientific Directions at the ALS" was held in March 1998. In July 1998, I was appointed Director of the ALS Division. Finally, in October 1998, the Users' Executive Committee (UEC) organized an outstanding ALS User Meeting that highlighted recent research achievements.

I see my appointment as ALS Director as an exciting opportunity to start Phase II of the life of this outstanding facility. During Phase I, under the direction of Jay Marx and then Brian Kincaid, we built the ALS—on time and under budget—and then added a complement of beamlines and endstations. The machine works beautifully. It delivers photons as promised with an impressive degree of reliability. And we already have some outstanding experimental capabilities that have produced unique experimental results. I congratulate Jay and Brian, the ALS staff, and the initial complement of users on their great achievement in bringing this about.

Looking ahead to the future, we will continue to develop the ALS, enhancing existing capabilities and adding new insertion devices, new beamlines, and new endstations. In doing this, however, we must now address in a much more direct manner the fundamental driving force behind any new research tool: the capability to do the new science that it was designed to do and, in particular, that science which it is uniquely capable of doing. A first major step here was our most successful and stimulating March workshop, chaired by Yves Petroff, Director-General of the European Synchrotron Radiation Facility. Each of nine working groups developed a set of recommendations as to future desirable directions and the particular support and instrumentation needs associated with them. In many cases, these recommendations have suggested specific teams and proposals for new beamlines or experiments, which are now working their way through the funding agencies. The workshop thus began to set the agenda for the ALS well into the 21st century. I intend to continue that dialogue with the utmost vigor.

Our users are our key resource for the future. It is obviously these people, both the present complement and the new people who will undoubtedly join us, that will initiate and carry out the new scientific agenda. They are the primary reservoir of knowledge and creativity about using and managing the ALS for maximum positive scientific impact. Accordingly, I have put in place several mechanisms and processes to improve the interaction between the ALS and its user community.

The principal change is to involve the UEC much more directly in the strategic planning of the ALS and the day-to-day management of the facility. In order to better evaluate new scientific directions and establish priorities, the ALS Scientific Advisory Committee (SAC) has also been reconfigured. It includes a number of outstanding scientists, including its Chair, Professor Z.X. Shen. The new configuration provides a much broader representation of the user community. The SAC will thus help us to develop a scientific program that is absolutely top notch. This committee has already started reviewing the major programs of the ALS, including proposals for new construction and the existing Participating Research Teams. The ALS Program Study Panels, which give recommendations on beamtime allocation to independent investigators, are now also broader in their representation of the users, and their memberships will start to rotate. These changes, and others, have gone a long way toward implementing the recommendations of the Oddone User Task Force, which were presented at the SAC meeting in July 1998 and at the ALS User Meeting in October 1998.

In addition, the ALS Science Policy Board (SPB) was convened by Director Shank in early 1998. The board emphasized that the ALS needs to retain its world-leading activities in the vacuum ultraviolet and soft x-ray regions of the spectrum, but at the same time, it endorsed the decision to expand the scientific base of the ALS by increasing the number of intermediate-energy (up to ~10–20 keV) x-ray beamlines as a resource for users. These beamlines, such as the one serving our Macromolecular Crystallography Facility, often do not require ultra-high vacuum for experiments and can thus handle many more users in a given period of time.

To boost the number of intermediate-energy beamlines, a major program to install three superconducting bend magnets (superbends) in the ALS has been initiated. These superbends will allow the development of up to 12 high-brightness, intermediate-energy x-ray beamlines without significantly compromising our capabilities in the VUV/soft x-ray regime and without taking up any of the three remaining straight sections that can accommodate new insertion devices. This program has generated significant regional user interest, and proposals for about seven of these beamlines have already been submitted or are in preparation.

An additional fundamental change in the machine is the installation of a third-harmonic cavity, which will permit the stretching of bunches and lengthen lifetimes by about a factor of three. We anticipate that this will allow us to fill the ALS about every 12 hours instead of every 4 hours without any reduction in the integrated flux or brightness. This cavity will benefit the vast majority of the ALS user community and will be installed during mid-1999. Another option that will be explored is the operation of the cavity in reverse, to shorten the bunches.

The ALS's core scientific program in the VUV/soft x-ray area has also seen major expansion during this period. This growth involves two new insertion devices. One lower-energy undulator aimed at studies of atomic physics and complex materials is already in operation and producing exciting results, and a second, higher-energy elliptically polarizing undulator designed for studying the magnetic properties of materials will come into operation shortly.

I therefore believe that the ALS has made a fine start on Phase II of its life, and I am most encouraged by the positive feedback we have received from the national-level Basic Energy Sciences Advisory Committee as well as from our own advisory bodies, the SPB and the SAC. But much remains to be done, and I look forward to working with the user community and the ALS staff both to encourage further development of the scientific program and to expand the technical capabilities of the ALS so as to provide a light source for the 21st century. We intend to do everything possible to provide a facility that allows our users to do the most creative experiments they can design. Our goal is to see a continuing stream of outstanding scientific results—results that cannot be achieved anywhere but at Berkeley's Advanced Light Source.

Science Highlights

Neville V. Smith
Deputy Director for the Scientific Program

The scientific program at the ALS is now growing faster than ever. Rapid increases in the number of beamlines and the number of users are reflected in the quality and quantity of scientific output. We offer here a selection of highlights. These were solicited from and kindly provided by researchers whose peers have acknowledged their work to be outstanding. Most of the studies have already appeared or been accepted in a high-prestige scientific journal such as Science, Nature, or Physical Review Letters. In previous years, our highlights have been reported in a literary style intended for a broad audience. This time, the writing has a sharper scientific edge, having been written by the researchers themselves. We welcome your comments on this change of style.

The categories used for the highlights spring from a two-day workshop on "Scientific Directions at the Advanced Light Source," which we conducted in March of 1998. More than 300 scientists from 14 countries descended on Berkeley to share their wisdom. The bulk of the workshop was spent in parallel breakout sessions in which working groups addressed specific scientific areas: complex materials, magnetism and magnetic materials, polymers, biomaterials and soft matter, etc. Each working group was asked to respond to the following challenging questions:

- Where is the forefront of your discipline?
- What is its impact on the rest of science, technology, and society?
- What is the role of a VUV/soft x-ray facility like the ALS?
- What special tools are needed?

The participants rose to the challenge, and the workshop report sets the agenda for the ALS scientific program well into the next century. The report can be viewed on the World Wide Web at http://www-als.lbl.gov/als/workshops/scidirect/.

As our scientific program has grown, our user demographics have changed in significant ways. Now that the protein crystallography beamline is in high gear, we find that 25% of our users are in the life sciences. We have nurtured environmental science to the extent that it now constitutes 10% of our user community. This is all to the good, since it demonstrates that we are adapting to the scientific imperatives that will prevail in the 21st century. But let it be clear that these developments in no way diminish our commitment to excellence in the more traditional areas of VUV and soft x-ray synchrotron radiation science. A brand-new facility dedicated to high-resolution spectroscopy in condensed-matter physics and atomic and molecular physics has just started producing results. But more of this in our next Activity Report!

Site-Selective Spectroscopy of Strontium Ruthenate with Soft X-Ray Emission

What is it about high-temperature superconductors (HTSCs) that allows them to perform as superconductors at temperatures far above absolute zero? To help answer this question, researchers at Beamline 8.0 have studied strontium ruthenate compounds, low-temperature superconductors with structures similar to those of copper-containing HTSCs. They have succeeded in distinguishing spectroscopically between oxygen atoms in different types of sites in these compounds. Their results show that the nature of the interaction between oxygen and ruthenium atoms is different from that occurring in HTSCs and results in a different type of chemical bond.

One of the burning questions in contemporary solid-state science is the nature of the mechanism driving superconductivity in the high-temperature superconductors (HTSCs), first discovered more than a decade ago. Some of these ceramic-oxide materials with complex compositions and structures retain their superconductivity at temperatures up to 125 K. The Nobel-prize-winning Bardeen–Cooper–Schrieffer theory developed for conventional metallic superconductors is not applicable, but no one yet knows exactly what the alternative is. Clues come not only from direct examination of the materials themselves but also from studies of related materials with similar composition and structure. In connection with this, we studied Sr_2RuO_4, which has a critical temperature (T_c) of 1.5 K and is structurally similar to the cuprate HTSCs, in which Cu–O planes replace the Ru–O planes. Working at Beamline 8.0, we used the University of Tennessee at Knoxville–Tulane University soft x-ray fluorescence endstation to selectively examine the electronic structure of bonding electrons associated with oxygen in two different sites in the crystal structures of the strontium ruthenate compounds Sr_2RuO_4 and $Sr_2RuO_{4.25}$.

The salient features in the strontium ruthenate crystal structure are planes comprising only ruthenium and oxygen atoms. Although there are interactions between planes, they are much weaker than those between electrons in the same plane, so that the systems are quasi-two-dimensional. There are also oxygen atoms outside the planes (apical oxygens). Owing to the different chemical environments for oxygen in these two types of sites [O(1) in the planes and O(2) outside them], the photon energies needed to excite O(1) and O(2) oxygen 1s electrons into 2p states are slightly different. The spectra shown in Figure 1

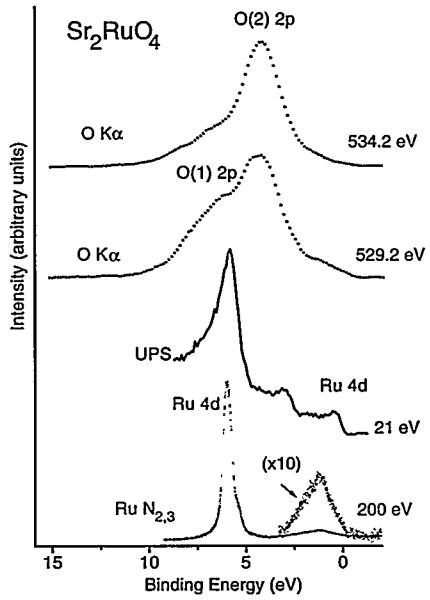

Figure 1

In strontium ruthenate compounds, researchers were able to distinguish spectroscopically between oxygen atoms in the ruthenium–oxygen planes and those outside the planes through excitation at different soft x-ray energies. With this capability, they demonstrated hybridization of ruthenium and oxygen electronic states. The top two curves show the distinctly different spectra for soft x-ray emission from oxygen in the strontium ruthenate compound Sr_2RuO_4. The bottom two curves show ultraviolet photoemission (UPS) and soft x-ray emission from ruthenium. The prominent peak at –6 eV in the ruthenium spectra matches the shoulder in the oxygen O(1) spectrum and is evidence for hybridization of ruthenium and in-plane oxygen electrons, as predicted by theory. A smaller peak near –1 eV also appears as a shoulder in the O(1) spectrum.

confirm that hybridization of ruthenium 4d and oxygen 2p states provides the principal bonding for the ruthenium–oxygen plane. The oxygen K-edge spectra provide a measure of the oxygen 2p density of states, and the ruthenium $N_{2,3}$-edge spectra provide a measure of the ruthenium 4d density of states. The spectra from the in-plane and out-of-plane oxygen atoms can be selectively measured by exploiting the chemical shifts of the oxygen 1s core levels. These spectra nicely match the calculated atom-decomposed partial density of electron states for the two oxygen sites. The in-plane oxygen spectra show a prominent shoulder with the same binding energy as the ruthenium 4d states, providing strong evidence that the oxygen 2p and ruthenium 4d electrons are hybridized. Comparing the x-ray spectra with angle-resolved photoemission spectra of Sr_2RuO_4, which can be used to distinguish ruthenium electron states of different symmetry [4d (t_{2g}) and 4d (e_g)], we found that the O(1) 2p states were mixed with d(t_{2g}) ruthenium states, thereby forming hybridized π bonds. Figure 1 graphically illustrates the fact that these 4d transition-metal compounds are indeed "extended-electron" systems, leading to strong hybridization, thus adding a new dimension to research in transition-metal oxides.

Investigators

E.Z. Kurmaev, D.A. Zatsepin, and N. Ovechkina (Institute of Metal Physics, Russian Academy of Sciences, Ural Division, Yekaterinburg); S. Stadler and D.L. Ederer (Tulane University); Y. Harada, S. Shin, M. Kasai, and Y. Tokura (University of Tokyo); M.M. Grush and T.A. Callcott (University of Tennessee, Knoxville); R.C.C. Perera (Berkeley Lab); T. Takahashi (Tohoku University); and K. Chandrasekaran, R. Vijayaraghavan, and U.V. Varadaraju (Indian Institute of Technology, Madras).

Funding

Russian State Program on Superconductivity; Russian Science Foundation for Fundamental Research; NATO Linkage Grant; National Science Foundation; U.S. Department of Energy, Office of Basic Energy Sciences; and Louisiana Education Quality Special Fund.

Publications

1. E.Z. Kurmaev et al., "Electronic structure of Sr_2RuO_4: X-ray fluorescence study," *Phys. Rev. B* **57**, 1558–1562 (1998).
2. E.Z. Kurmaev et al., "Electronic structure of ternary transition metal oxides and sulphides: X-ray photoelectron and x-ray emission spectroscopy study," *J. Electr. Spectr. Relat. Phenom.* **88–91**, 441–447 (1998).

Electronic Structure of the Hydrogen-Induced Metal–Insulator Transition in Yttrium

Yttrium metal becomes an optically transparent insulator when loaded with hydrogen. Scientists would like to understand the changes in the electronic structure that cause this metal–insulator transition as hydrogen is added. X-ray spectroscopy (emission studies combined with absorption studies) provides a way to probe the electronic structure. Measurements at the ALS confirm the emergence of an electronic-structure feature (band gap) characteristic of a transparent insulator with increasing hydrogen content. They also furnish clues about the influence of hydrogen on yttrium electronic states.

The discovery of hydrogen-induced optical switching, in which yttrium metal becomes transparent upon hydrogen loading, stimulated considerable interest in the optical properties of the lanthanide hydrides and in their underlying electronic structure. Although this metal–insulator transition is conceptually simple, the changes in the electronic structure are not fully understood.

Soft x-ray emission spectroscopy (SXES) allows direct probing of the local valence electronic structure in terms of the symmetry-selected *occupied* density of states. Furthermore, soft x-ray absorption spectroscopy (SXAS) allows one to probe the *unoccupied* density of states. The combination of

SXES and SXAS thus provides a means to study metal–insulator transitions. Moreover, the substantial attenuation length of soft x rays allows SXES to be applied to buried structures or to samples at ambient gas pressures. This capability is necessary for studies of hydrogen loading, since samples have to be either capped after hydrogen loading or exposed to hydrogen gas during measurement.

Our experiments were performed at Beamline 7.0 of the ALS. The yttrium $M_{4,5}$ emission spectra (transitions to $3d_{3/2}$ and $3d_{5/2}$ core states) were recorded with the Uppsala University SXES spectrometer installed at this beamline. The soft x-ray absorption spectra were recorded in fluorescence-yield mode with the same instrument. The data presented here were obtained for samples that were hydrogen loaded and capped in the preparation process. Three samples of different hydrogen loading were studied: yttrium metal (no loading), yttrium dihydride, and yttrium trihydride.

Figure 2 shows the SXES spectra for valence-to-3d core transitions in the three samples, along with the corresponding SXAS spectra. A sharp edge at the top of the valence band in yttrium is identified as the Fermi level. SXAS shows an onset at this energy, which implies an overlap between the top of the valence band and the bottom of the conduction band. The overlap reflects the metallic character of yttrium. A substantial change is observed in the x-ray emission with increasing hydrogen content. The total intensity increases, and a strong hybridization feature appears about 6 eV to 7 eV below the Fermi level. At the Fermi level, one still observes features of reduced intensity. In the trihydride spectrum, a further reduction in intensity is observed at the Fermi level, indicating a band gap with an estimated width of 2.5 eV. This observation is consistent with the reported transparency and slightly yellowish color of yttrium trihydride.

In the emission spectra for yttrium $4p_{3/2}$-to-$3d_{5/2}$ core–core transitions in the same three samples (Figure 3), one observes increased bandwidth for the hydrides and a shift to a lower transition energy. In a simple picture, we expect the inner, more localized state in the hydrides to be more

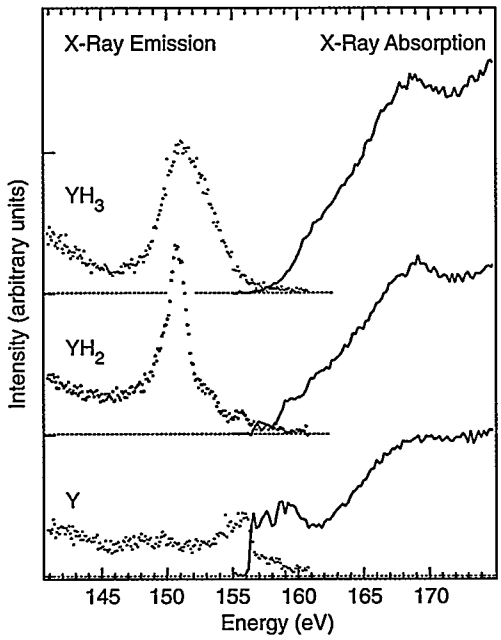

Figure 2

Soft x-ray emission (red) and absorption (blue) spectra, which probe, respectively, occupied and unoccupied states close to the Fermi level, demonstrate the emergence of a band gap with increasing hydrogen loading of yttrium.

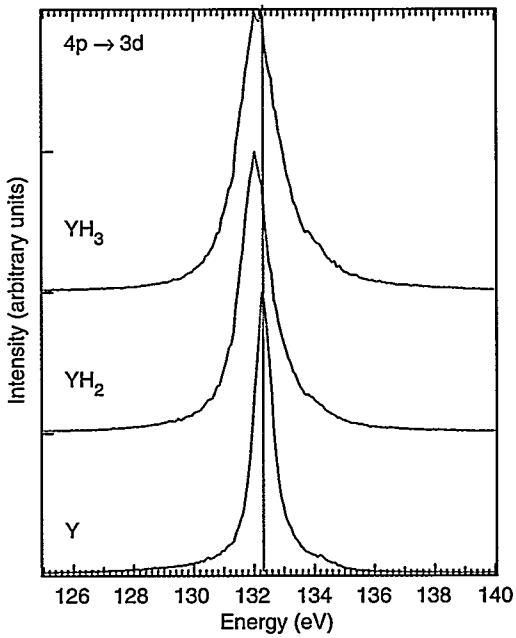

Figure 3

Soft x-ray emission spectra of yttrium $4p_{3/2}$-to-$3d_{5/2}$ core–core transitions in yttrium metal, yttrium dihydride, and yttrium trihydride show an energy shift and broadening that suggest electron charge donation to the yttrium sites.

affected by a change in charge density, so the energy shift suggests that the hydrogen uptake leads to electron *donation* to the yttrium sites. However, first-principles calculations of the electronic structure suggest a modified picture, in which, instead of electron charge transfer, a strong hybridization between the hydrogen 1s states and the yttrium states occurs. The hybridization causes shifts similar to what one would expect from a charge-transfer model.

Investigators

B. Hjörvarsson (Royal Institute of Technology, Sweden); J.-H. Guo, G. Andersson, R. Ahuja, O. Eriksson, C. Såthe, A. Agui, S.M. Butorin, and J. Nordgren (Uppsala University, Sweden); and R.C.C. Ward and M.R. Wells (Oxford University).

Funding

Natural Science Research Council, Sweden.

How Much Energy Does It Cost to Tilt a Hole?

One signature of the onset of superconductivity is the formation of electron pairs, but the electron-pairing mechanism for high-temperature superconductivity is one of the great unsolved problems of condensed-matter physics. A team of Swedish and Dutch scientists has used x-ray spectroscopy (resonant x-ray Raman scattering) to investigate electronic transitions within copper atoms in $Sr_2CuO_2Cl_2$, an insulating model compound for the copper-based high-temperature superconductors. Contrary to earlier conjecture, they found that these transitions have energies that are too high to be directly involved in the electron-pairing mechanism.

The common feature of high-temperature superconductors is their sandwich structure, in which the essential ingredient (the "bread") consists of copper-oxide planes. In these planes, each Cu^{2+} ion is surrounded by four oxygen atoms. The Cu^{2+} ions have nine 3d electrons in the ten available 3d orbitals, which leaves one 3d orbital unoccupied. This one unoccupied orbital is called a hole. We know from the angle dependence of x-ray absorption that this hole orbital is oriented in the plane with four lobes pointing toward the four neighboring oxygen atoms, because the electrons are repelled by the negative charge on the oxygen. In a coordinate system with x and y axes pointing toward oxygen atoms, this 3d orbital is called an x^2–y^2 orbital.

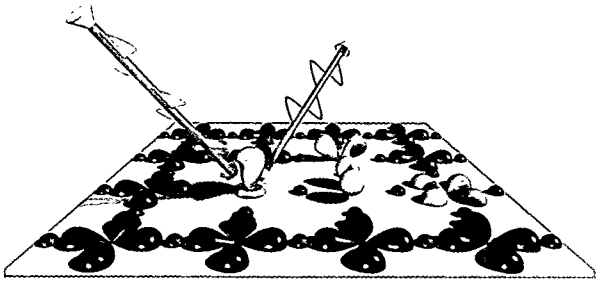

Figure 4

The common feature of high-temperature superconductors is a set of parallel copper–oxygen planes. In these planes, each Cu^{2+} ion is surrounded by four oxygen atoms (red). The unoccupied 3d orbitals of copper (holes) are shown in blue (ground state: x^2–y^2) and green (excited states: from left to right, z^2, xz, yz, and xy). In Raman scattering, the absorption of an x ray (shown in yellow) and the emission of an x ray (orange) result in the excitation of the copper d orbital from the ground state to an excited state with a different orientation.

Putting the hole in a differently oriented orbital costs energy. How large these energies are is a potentially important question for the theory of high-temperature superconductivity. If these energies are small (comparable to the thermal energy), excitations to these orbitals should be considered in whatever electron-pairing mechanism is operative in the superconductivity. However, these energies have not been measured. While the red color of ruby clearly reveals the 3d reorientations on chromium ions in this transparent gemstone, the black copper-oxide materials effectively hide these energies from experiments with visible light. A different method is needed.

In our studies, we reorient the 3d holes via a detour. We first excite an electron from the Cu 3p core level into the empty 3d orbital. This can be done with x rays at an energy of 75 eV. We then

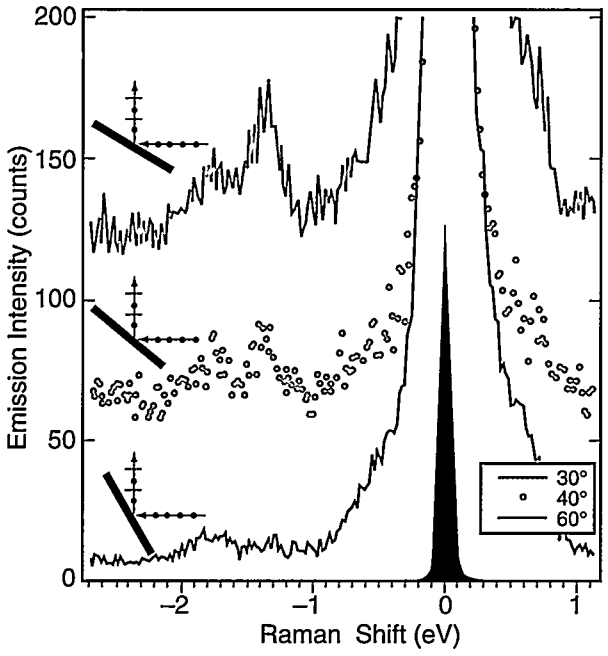

Figure 5

Raman scattering gives two low-intensity peaks, one at −1.35 eV and the other at −1.8 eV relative to the large elastic scattering peak (solid peak with an intensity reduced by a factor of 200). The intensity of the peak at −1.35 eV grows as the angle of emission decreases relative to the sample normal, i.e., as the component of the emission with polarization in the plane of the surface increases. From this information, the peak at −1.35 eV was assigned to the transition to the *xy* orbital, which lies in the plane of the surface, whereas the peak at −1.8 eV was associated with transitions to the *xz* and *yz* orbitals, which have components normal to the surface.

detect the x rays coming out. If the excited electron falls back into the 3p hole that it left behind, it radiates back the 75 eV that we put in. But there is also a large probability that one of the other 3d electrons falls into the core hole. If an electron falls back by radiating 73 eV, we know that the hole is now in a 3d orbital with a different orientation. The energy difference, 75 eV − 73 eV = 2 eV, is the same as that for reorienting the hole directly. By comparing the intensities emitted normal to the plane and parallel to the plane, we can also deduce the hole's orientation. We found the *xy* orbital at 1.35 eV, the *xz* and *yz* orbitals at 1.7 eV, and the z^2 orbital at 1.5 eV, all of them too far above the ground state x^2-y^2 to play a direct role in the electron-pairing mechanism for high-temperature superconductivity.

This x-ray detour for measuring excitation energies is an example of Raman scattering. Raman spectroscopy with visible light only became routine after the invention of lasers. For doing Raman scattering with x rays, we need a very bright light source that can be focused into a tiny spot. With the brightness afforded by the ALS, we have been able to use x-ray Raman spectra for measuring excitation energies that were not known before, thereby shedding light on an important problem in superconductivity. We believe that this technique can be used to address many other problems, such as colossal magnetoresistance, in complex materials dominated by strong Coulomb interactions between electrons (highly correlated systems).

Investigators

P. Kuiper, J.-H. Guo, C. Såthe, L.-C. Duda, and J. Nordgren (Uppsala University, Sweden); and F.M.F. de Groot and G.A. Sawatzky (Groningen University, The Netherlands).

Funding

National Research Council, Sweden.

Publications

1. P. Kuiper et al., "Resonant x-ray raman spectra of Cu *dd* excitations in $Sr_2CuO_2Cl_2$," *Phys. Rev. Lett.* **80**, 5204 (1998).
2. F. M. F. de Groot et al., "Local spin-flip spectral distribution obtained by resonant x-ray raman scattering," *Phys. Rev.* B **57**, 14584 (1998).

Quantum Well Interference in Magnetic Heterostructures

The study of ferromagnetic films separated by a thin nonmagnetic spacer led to the discovery of giant magnetoresistance (GMR), which in turn led to significant advances in magnetic data storage technology. The GMR effect depends on the relative alignment of the electron spins in the ferromagnetic layers. Another interesting discovery was that the spins oscillate in direction as the thickness of the spacer material increases. Pioneering photoemission experiments at other facilities have shown that this oscillation is associated with quantum-well-state effects in the spacer. New work by scientists at the x-ray photoelectron diffraction chamber on Beamline 7.0.1 has, in addition to confirming the quantum-mechanical origin of this oscillation, revealed additional, more subtle interference effects. By deepening our understanding of the physics of this phenomenon, this work opens the door to the possibility of manipulating wave functions as needed for nanometer-size magnetic components.

When two ferromagnetic layers are separated by a thin nonmagnetic spacer, the relative spin directions of the ferromagnetic layers oscillate as a function of the spacer thickness, with a periodicity of a few atomic layers. Moreover, as an external magnetic field is applied to switch the relative spin directions of the two ferromagnetic layers, giant magnetoresistance could be produced from this new class of magnetic nanostructures. These discoveries have great potential for applications involving magnetic sensors, and technological development demands an understanding of these phenomena at a fundamental level. The goal of our research is to explore the physical origin of this oscillatory coupling at the atomic scale.

The oscillatory behavior of the interlayer coupling led to the proposal of the Rudermann–Kittel–Kasuya–Yosida (RKKY) and quantum well (QW) theories to explain the origin of the magnetic coupling. The RKKY coupling is derived from the interaction of the electrons in the spacer layer with the magnetic moments at the interface of the ferromagnetic layer. The QW coupling arises from the formation of QW states in the spacer layers. The key difference between these two mechanisms is that RKKY coupling is an interfacial effect while QW coupling is not. We can experimentally distinguish between these two mechanisms by observing whether the QW states in the spacer layer are modulated by other layers outside the QW, i.e., by identifying interference effects between two QWs.

Although QW states in the spacer can be detected as peaks in photoemission intensity, detecting the interference effects, which are easily overwhelmed by thickness variations, requires a series of highly sensitive measurements with very small thickness increments. We overcame these difficulties by growing double-wedged samples (Figure 1) in which the copper QW thickness and its separation from the nickel reflection layer (cobalt thickness) could be varied independently. A scanning photoemission experiment was performed on this double-wedged sample,

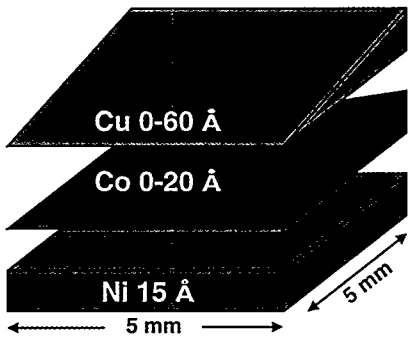

Figure 1

Double-wedged geometry allows for independent variation of the copper and cobalt thicknesses.

and the result clearly identified the interference between the copper QW states and the electron waves reflected by the nickel layer (Figure 2).

The results of this work imply that the electron spins can be controlled by the QW states in the magnetic nanostructures. Since the QW states depend on the band gap of the ferromagnetic layer, a natural extension of this work will be the engineering of band gaps to generate new properties for magnetic sensors.

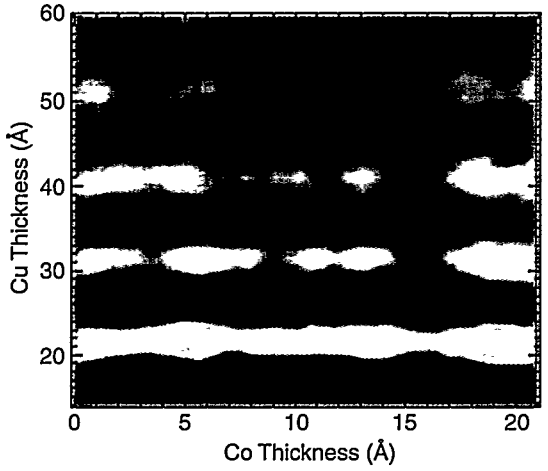

Figure 2

Photoemission intensity at the Fermi edge as a function of the copper and cobalt thicknesses. The oscillations with copper thickness identify quantum well states in the copper layer. The oscillations with cobalt thickness identify the interference between the copper quantum well and the electron waves reflected by the nickel layer.

Investigators

R.K. Kawakami, E.J. Escorcia-Aparicio, H.J. Choi, and Z.Q. Qiu (University of California, Berkeley); E. Rotenberg and N.V. Smith (Berkeley Lab); and T.R. Cummins and J.G. Tobin (Lawrence Livermore National Laboratory).

Funding

U.S. Department of Energy, Office of Basic Energy Sciences, and Hellman Family Faculty Fund at Berkeley.

Publications

1. R.K. Kawakami et al., "Observation of quantum well interference in magnetic nanostructures by photoemission," *Phys. Rev. Lett.* **80**, 1754–1757 (1998).

X-Ray Resonant Scattering from Magnetic Multilayers: A Way to Obtain Optical Constants at Core-Electron Excitations

Magnetic multilayers are now coming into use in high-density magnetic storage devices, but the basic understanding needed to fully understand and control the behavior of these artificially structured materials is not yet in hand. To help provide some of the information needed, an international team of researchers working at Beamline 6.3.2 has used circularly polarized x rays to measure the optical constants of the magnetic material, iron, in a magnetized iron/vanadium multilayer. The optical constants of a material determine its response to light and are therefore needed to match the predictions of theoretical models with the results of experiments.

Magnetic multilayers are currently the focus of considerable activity, owing to the giant magnetoresistance effect (dependence of the electrical resistance on the applied magnetic field) that is just beginning to be exploited in state-of-the-art devices for high-density magnetic data storage. We have used resonant scattering of circularly polarized soft x rays to measure the optical constants of iron near its 2p absorption edges in magnetic multilayers. The optical constants measure the response of a material to excitation by electromagnetic radiation and are therefore needed to fully reconcile theoretical models with the results of experiments, often conducted at core-electron resonances, that are aimed at understanding and controlling the behavior of these artificially structured materials.

We used a model system composed of alternate iron and vanadium layers, each about 15 Å thick. According to the same law that describes x-ray

diffraction, the reflectance of the multilayers is a maximum (Bragg peak) at an angle determined by the thickness of an iron/vanadium layer pair, the photon wavelength (or energy), and by the index of refraction of the material. Resonant scattering is a further enhancement that occurs when the wavelength is near an absorption edge. For our experiments, the relevant absorption edges are the L_3 and L_2 edges, at photon energies of about 707 eV and 720 eV, which correspond to the excitation of a 2p core electron into the partially empty 3d band of iron.

The optical constants are the absorptive, β, and dispersive, δ, components of the complex index of refraction, $n = 1 - \delta - i\beta$. X-ray absorption can directly yield the component β. If taken over a wide enough energy range, absorption can also indirectly reveal the dispersive component, δ, via a mathematical technique known as the Kramers–Kronig transformation. This method, however, requires approximate numerical procedures and parameterizations, which affect the results. Fortunately, detailed measurements of the angular position of the Bragg peak for photon energies around the absorption edges can provide a direct experimental evaluation of the index of refraction without the use of the Kramers–Kronig technique.

We performed x-ray scattering and absorption measurements at the iron 2p edges using circularly polarized radiation from soft x-ray metrology Beamline 6.3.2 at the ALS. With its high-precision reflectometer endstation, Beamline 6.3.2 offers a unique experimental facility that optimizes the parameters relevant to these measurements, including mechanical precision and stability as well as energy resolution, flux, and polarization state of the x-ray beam.

Resonant measurements (Figure 3) show a strong dependence of the scattered intensity on the sample magnetization, which was set to be either parallel or antiparallel to the helicity of the light. From these data and from the absorption curves measured under the same conditions, we were able to extract the magnetization-dependent optical constants δ and β for iron over the energy region including the 2p resonances. From the optical constants we could reconstruct all the components of the dielectric tensor, which is the quantity that measures the response of the material to electromagnetic fields. In particular, the diagonal elements give the response of the material to unpolarized radiation, while the off-diagonal elements of the dielectric tensor are directly related to the magnetic properties of the sample.

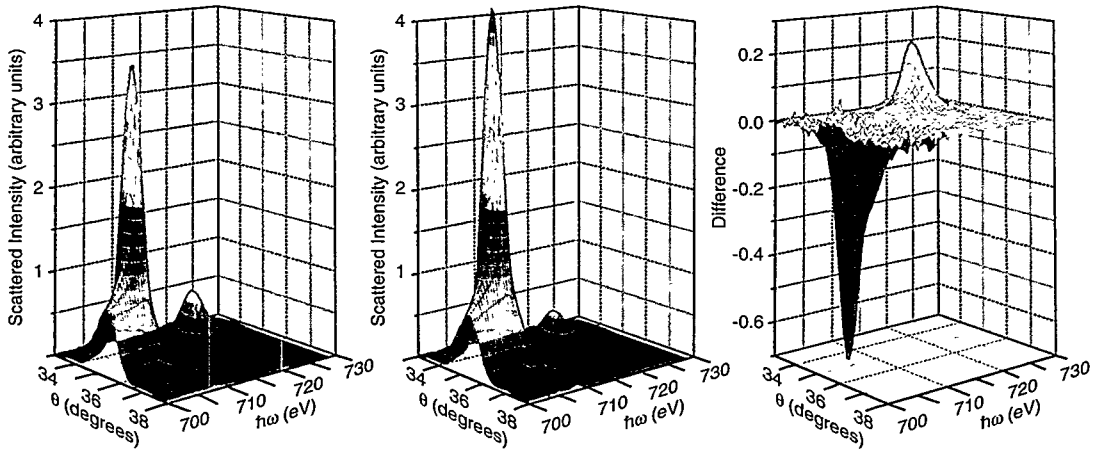

Figure 3

The optical constants for iron are derived from the angular position of the Bragg peak for photon energies near the L_3 and L_2 absorption edges. Measurements were made for parallel (left) and antiparallel (center) orientations of the sample magnetization and helicity of circularly polarized soft x rays. The observed difference (right) is related to the magnetic properties of iron in the iron/vanadium superlattice.

Investigators

M. Sacchi and A. Mirone (LURE and Centre Universitaire Paris-Sud); C.F. Hague and J.-M. Mariot (Université Pierre et Marie Curie); L. Pasquali (Università di Modena and Istituto Nazionale per la Fisica della Materia, Modena); P. Isberg (Uppsala University); and E.M. Gullikson and J.H. Underwood (Berkeley Lab).

Funding

Centre National de la Recherche Scientifique; Ministère de l'Education Nationale de la Recherche et de la Technologie; Istituto Nazionale di Fisica della Materia; U. S. Department of Energy, Office of Basic Energy Sciences.

Publications

1. M. Sacchi et al., "Optical constants of ferromagnetic iron via 2p resonant magnetic scattering," *Phys. Rev. Lett.* **81**, 1521 (1998).
2. M. Sacchi et al., "Resonant magnetic scattering of polarized soft x-rays: Specular reflectivity and Bragg diffraction from multilayers," *Phys. Rev. B* **57**, 108 (1998).
3. M. Sacchi and A. Mirone, "Resonant reflectivity from a Ni(110) crystal: Magnetic effects at the Ni 2p edges using linearly and circularly polarized photons," *Phys. Rev. B* **57**, 8408 (1998).

Transmission Imaging of Thin-Film Magnetization

Magnetic features in thin films can now be imaged with a new circularly polarizing filter that adds magnetic sensitivity to the existing scanning transmission x-ray microscope (STXM) at the ALS. Early studies have demonstrated high contrast for magnetic features in layers several nanometers thick with 200-nm or better lateral resolution. They have also revealed subtle details about the magnetization-reversal process in iron films. The high contrast, sensitivity to specific elements, and dependence on both angle and applied field make transmission x-ray imaging complementary to other techniques for imaging magnetization in magnetic nanostructures.

Imaging magnetic features with high sensitivity and a spatial resolution approaching nanometer or even atomic dimensions continues to drive the development of numerous types of magnetic microscopes. The first soft x-ray magnetic microscope operating in the scanning transmission mode has recently been developed at the ALS and is beginning to be used in studies of thin-film magnetization.

The scanning transmission x-ray microscope (STXM) on Beamline 7.0.1 provides high spatial and spectral resolution for soft x-ray imaging, but the linearly polarized undulator radiation does not by itself provide magnetic contrast. Incorporating a circularly polarizing filter in the STXM beamline, however, readily provides contrast for magnetization changes. Such a filter was developed to convert linear to elliptical polarization in the 700–900-eV range, a spectral region containing the 2p core levels of iron, cobalt, and nickel. Transmission through a magnetic film with saturated magnetization **M** selectively filters out one of the two circular components of opposite helicity contained in the incident linearly polarized beam, owing to the large magnetic circular dichroism at the $2p_{3/2}$ core levels of these elements. Reversing the magnetization direction in the filter reverses the helicity of the transmitted radiation and hence reverses the image contrast.

Demagnetized iron thin films were among the first samples imaged with the magnetic STXM, in part because they exhibit strong, distinct magnetic features. In addition, the demagnetized state represents a transition between saturated magnetization states and so provides information about the magnetization-reversal process. Figure 4 shows several images of a demagnetized, 23-nm-thick iron film. Figure 4a is a coarse image of the entire sample, which was sputter deposited through a 0.4-mm × 0.4-mm square aperture onto a silicon nitride membrane. Magnetization reversal in this sample proceeds via domain nucleation and growth through domain-wall motion, as revealed in the image by large 180° domains in which the magnetization reverses direction across domain walls.

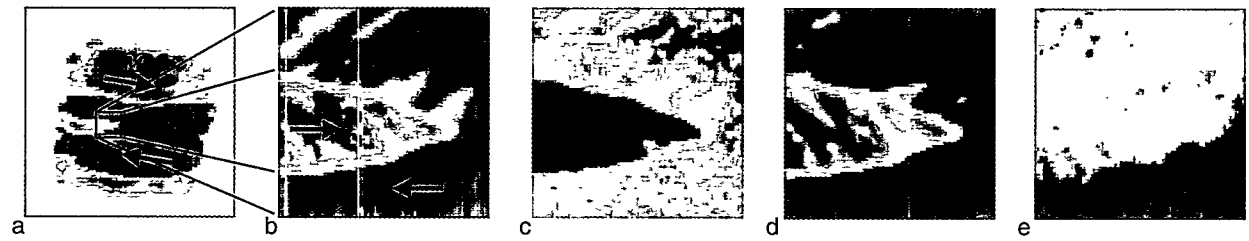

Figure 4

Magnetic STXM images of a demagnetized, 23-nm-thick iron film. (a) A coarse image of the entire sample showing large magnetic domains of opposite magnetization. Arrows indicate the nominal magnetization direction in each domain. (b–e) Higher magnification images of a 40-μm × 40-μm region comprising the tip of the blade-shaped domain seen in (a). Images (b) and (c), taken with opposite photon helicity, have reversed contrast. Image (d) is the division of (b) by (c) and effectively enhances the contrast of each. Image (e) is the multiplication of (b) and (c) and reveals regions where the ripple structure is pronounced.

Figures 4b–4e are higher magnification images of the same 40-μm × 40-μm region comprising the tip of the blade-shaped domain seen in Figure 4a. These higher resolution images reveal a ripple structure in the magnetization that extends into the larger surrounding domain above the tip. The ripple results from regular buckling of the magnetization vector from its preferred in-plane orientation to include some out-of-plane components in these regions. Thus, even this static image reveals that domain-wall motion is accompanied by a disturbance in the magnetization extending tens of microns away from the domain walls, somewhat like the crumpling of a piece of paper as it is forced to deform. Figure 4e highlights regions where the magnetization varies spatially from its nominal directions in the unperturbed domains and reveals regions where the ripple structure is pronounced.

Though the sequence of magnetization reversal in iron films was already known, these images reveal powerful capabilities of transmission x-ray imaging of magnetization that will make possible a variety of future studies. The contrast results directly from the projection of the magnetization vector along the wave vector (i.e., $\mathbf{k}\cdot\mathbf{M}$) and is readily expressed in analytical form. By varying the incidence angle, it is thus straightforward to determine the components of $\mathbf{M}$, thereby providing quantitative magnetization maps for comparison with theoretical micromagnetic models. The large, 20% contrast levels in the individual images clearly indicate that magnetization images of films on the order of one nanometer thick are feasible. The element specificity inherent in this technique provides a unique capability to unambiguously image magnetization distributions in individual magnetic layers of layered structures and hence to study the three-dimensional magnetization resulting from interactions between magnetic layers. Imaging studies as a function of applied magnetic field are also possible.

Investigators

J. B. Kortright, S.-K. Kim, T. Warwick, and G. Meigs (Berkeley Lab).

Funding

U.S. Department of Energy, Office of Basic Energy Sciences.

Publications

1. J. B. Kortright et al., *Appl. Phys. Lett.* **71**, 1446 (1997).
2. J. B. Kortright et al., *J. Magn. Magn. Materials* **191**, 79 (1999).

PEEM Studies of Thin-Film Bilayers and Blends of Polystyrene and Brominated Polystyrene

Polymeric films are featured in a wide variety of technologies, from optical coatings and low-dielectric electronic packaging to color printing and adhesives. In such applications, the way in which the molecules of a polymer film on a substrate tend to clump together when heated (dewetting) can make a difference in final product quality. For example, in colloidal paint systems, the dewetting process controls the dispersion of color pigments. Yet, compared to bulk properties, relatively little is known about how a polymer's surface composition changes during dewetting. Photoemission electron microscopy (PEEM) studies of polymer bilayers and blends enable researchers to gain quantitative information about the chemistry and dynamics of polymer films at surfaces and interfaces.

Thin films of polymers have considerable technological importance and are used in numerous applications. Understanding the dewetting and phase-separation phenomena of bilayers and blends is crucial for the use of polymers in such applications. Previous studies of blends of polystyrene (PS) and partially brominated polystyrene (PBrS) using scanning transmission x-ray microscopy (STXM) and atomic force microscopy have revealed a complex morphology that forms as the PS and PBrS undergo phase separation and as thin bilayers dewet. Despite these studies, the surface morphology and surface composition remained unknown. Therefore, surface-sensitive photoemission electron microscopy (PEEM) was used to investigate the surface composition during the dewetting of various PS/PBrS thin films.

The experiments were performed at Beamline 8.0. The PEEM microscope located at this beamline is a two-lens system operating at a nominal voltage of 10 kV. With this microscope, it is possible to obtain locally resolved, near-edge x-ray absorption fine-structure (NEXAFS) spectra with the spatial resolution of the microscope (200 nm).

Blends and bilayers of PS and PBrS on silicon substrates were used for these studies. The blends contained 50% PS and 50% PBrS and had a total thickness of 43 nm; the bilayers consisted of a 30-nm-thick PBrS layer on top of a 30-nm-thick PS layer. The samples were annealed for different durations at 180°C in a vacuum oven.

PEEM microscopy of a 2-day-annealed sample confirmed that the dewetting process starts locally in small areas. Figure 1 shows a PEEM image of a 2-day-annealed sample in which we observed a contrast variation in a small spot when the area was imaged at the PS π^* resonance and at the shifted PBrS π^* resonance energy. The image in Figure 1 was acquired at 286.3 eV (PBrS π^* resonance, spot dark). Local NEXAFS spectra were acquired in the spot and in two adjacent areas outside the spot for reference. The spectra (Figure 2) show that inside the spot the underlying PS

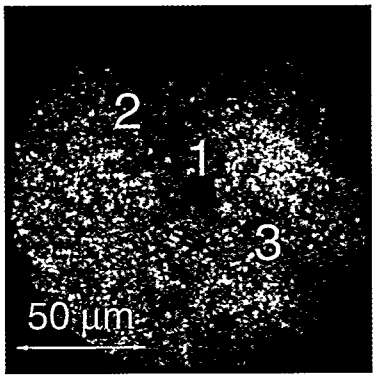

Figure 1

PEEM image of a 2-day-annealed polystyrene/partially brominated polystyrene (PS/PBrS) bilayer acquired at 286.3 eV. The image indicates the three areas where the local NEXAFS spectra in Figure 2 were acquired.

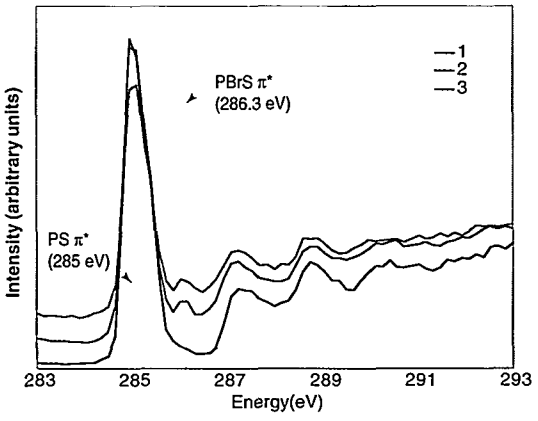

Figure 2

Local carbon K-edge NEXAFS spectra of the areas indicated in Figure 1. Spectra are offset for clarity. The large peak at 285 eV is the PS π^* resonance. The smaller peak at 286.3 eV is the PBrS π^* resonance; this peak is absent in the spectra taken within the spot.

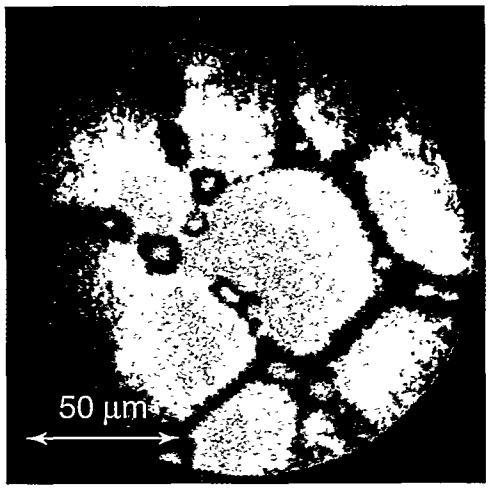

Figure 3

PEEM image of a 4-day-annealed PS/PBrS bilayer acquired at 286.3 eV.

layer is exposed as the PBrS dewets, whereas outside the spot the PBrS is still at the surface.

Images of bilayers annealed for longer durations (Figure 3) show the same network of spines previously observed with other methods. Contrast in the PEEM image is based solely on topography, and no chemical contrast was observed. In all areas, only PS was detected at the surface, revealing that the PS actually encapsulated the PBrS spines. In blends as well, only PS was detected at the surface, even prior to annealing.

The PEEM results showed that the dewetting of the PBrS polymer from the PS sublayer initially exposed a pure PS surface in small areas, while in most areas PBrS was still present at the surface. It was found that the PBrS spines formed in later stages of annealing were covered by a thin PS layer. Complementary results have been obtained with STXM. These types of studies allow the investigation of polymer dynamics and provide information about interfacial energies and the relative diffusion rates and viscosities of polymers in the presence of interfaces.

Investigators

Simone Anders, Thomas Stammler, and Clemens Heske (Berkeley Lab); Harald Ade (North Carolina State University); Dan Slep (Hilord Chemical Corporation); Jonathan Sokolov and Miriam Rafailovich (State University of New York at Stony Brook); and Joachim Stöhr (IBM Almaden Research Center).

Funding

U.S. Department of Energy, Office of Basic Energy Sciences, and National Science Foundation Young Investigator Award.

Publications

1. B. Tonner et al., "A photoemission microscope with a hemispherical capacitor energy filter," *J. Electr. Spectr. Relat. Phenom.* **84**, 211–229 (1997).
2. H. Ade et al., "Bulk and surface characterization of a dewetting thin film polymer bilayer," *Appl. Phys. Lett.* **73**, 3775 (1998).

Scattering of Coherent Soft X-Ray Light

Robert Brown discovered the thermally driven motion of small particles in solution in 1828, and Albert Einstein provided a theoretical understanding of Brownian motion in 1905. Now we can reliably measure the Brownian motion of small molecules in considerable detail by using dynamic laser-light scattering. Also inside molecules, there are interesting thermally driven motions that are thought to be crucial to chemical reaction rates, catalysis, and biological function. But how can scientists measure the molecular-scale motions of collective fluctuating systems? They cannot use laser-light scattering directly, because the spatial resolution is set by the wavelength of the light, and the wavelength of visible light is much greater than the size of the molecules. To probe atomic- or molecular-length scales, researchers can do the exact analogue of laser-light scattering by using the coherent x rays at Beamline 7.0.1.3.

Recently, there has been considerable interest in using hard x rays to probe atomic-scale motions at slow time scales. Because we wanted to measure fast fluctuations at molecular-length scales, however, we needed more coherent photons than we could obtain at a third-generation hard x-ray synchrotron. Since the available coherent flux is proportional to the spectral brightness of the source times the wavelength squared, and since all hard and soft x-ray third-generation sources have comparable spectral brightness, using longer wavelengths gave us higher coherent flux. We were able to obtain about 2000 times more coherent photons by working at the ALS with a wavelength of 44 Å than we would working at hard x-ray synchrotron radiation sources with 1 Å. Because we wanted to measure fluctuations at molecular-length scales, we could afford to use longer wavelengths.

Our goal was to develop this technique so that we could use it to probe fluctuations during phase transitions and to study the internal motions of biological molecules. Before applying it to the difficult problems of phase transitions and biology, however, we decided to apply it to a simpler problem: the fluctuations of freely suspended liquid crystal films. For this type of system, we were able to achieve the same time resolution as conventional laser-light scattering (about 1 μs) and 100 times better spatial resolution (44 Å vs. 6360 Å).

Our experimental setup is shown schematically in Figure 4. The crucial elements were the double-pinhole coherence filter, which converted the low-coherence raw undulator beam into the high-coherence incident beam necessary for the experiment; the liquid-crystal-film sample stage, which consisted of an oven to heat the liquid crystal into

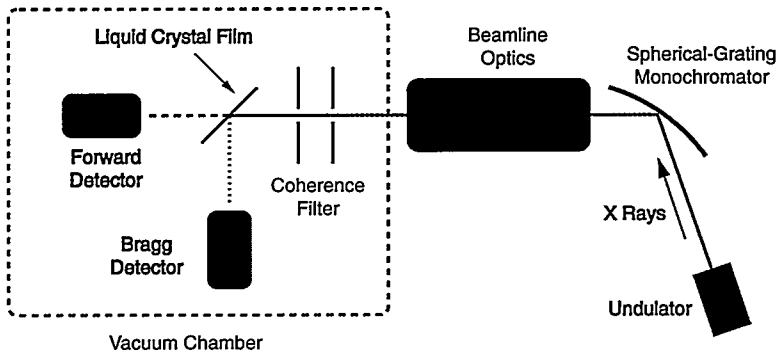

Figure 4

Experimental setup for measuring fast fluctuations at molecular time scales, showing the major beamline components and the vacuum chamber endstation (containing the double-pinhole coherence filter, liquid crystal film, and detectors).

the soap-like smectic-A phase plus the necessary position and rotation stages; and the high-speed, high-quantum-efficiency soft x-ray detectors that we developed for this experiment.

The idea behind our measurements is shown in Figure 5, an artist's illustration of the layer fluctuations in a liquid crystal film. The separations between the molecules and between the layers have been exaggerated so that we can see inside the system. Imagine reflecting photons from this fluctuating system; the intensity of the reflected beam will fluctuate in time due to the fluctuations of the sample. If the incident beam is spatially coherent, the reflected beam fluctuations are an average over all of the illuminated molecules. By measuring the reflected beam fluctuations at different reflection angles, which probe different Fourier components of the sample, we find the characteristic time of the sample fluctuations for each Fourier component.

With future access to the raw undulator beam (unfiltered by a monochromator), we will have 1000 times more coherent flux than we had for this experiment. Once suitable technique and source improvements are made, we should be able to go beyond the usual time-averaged x-ray snapshots to produce x-ray movies of the motion of molecules and atoms.

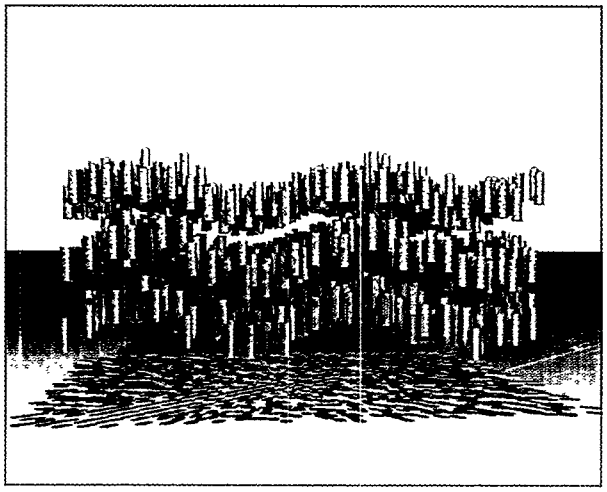

Figure 5

Artist's illustration of the layer fluctuations in a liquid crystal film. The separations between the molecules and between the layers have been exaggerated so that we can see inside the system (illustration by Dennis Yee).

Investigators

A.C. Price and L.B. Sorensen (University of Washington) and S.D. Kevan (University of Oregon).

Funding

U. S. Department of Energy, Office of Basic Energy Sciences; American Chemical Society Petroleum Research Fund; and University of Washington Molecular Biophysics Training Grant.

Publications

1. A. Poniewierski et al., "Dynamic correlation functions for finite and infinite smectic-A systems: Theory and experiment," *Phys. Rev. E* **58**, 2027–2040 (1998).
2. A. Price et al., "Coherent soft-x-ray dynamic light scattering from smectic-A films," *Phys. Rev. Lett.* **82**, 755–758 (1999).
3. A. Poniewierski et al., "Dynamic critical behavior of the Landau-Peierls fluctuations: Scaling form of the dynamic density autocorrelation function for smectic-A films," *Phys. Rev. E*, in press.

Grain Orientation Mapping of Buried Aluminum Wires with X-Ray Microdiffraction

In conductors that carry a high current density, the motion of the electrons can transfer enough momentum to physically move atoms in the conducting material. This phenomenon, called electromigration, is particularly significant in modern microelectronic devices, where voids in the conductors (aluminum wires buried within a silicon dioxide coating) can lead to line breakage and circuit failure. A fundamental understanding of this process requires quantitative structural data for micromechanical modeling. This can be achieved with a detailed knowledge of metallic grain orientation and lattice spacing within the grains of the conducting material. Researchers at the ALS have taken the first steps in gaining this information by using x-ray microdiffraction at Beamline 10.3.2 to measure the Laue diffraction patterns from single grains of aluminum on a substrate of silicon.

Electromigration is the physical movement of atoms in metallic interconnect lines passing current at high electron density (typically around 10^5 A/cm^2). Significant material movement results in voids that consequently lead to breakage and circuit failure in the metal lines. This problem gets more severe as line dimensions continue to shrink on integrated circuits. In spite of much effort in this field, electromigration is not well understood; however, it is strongly associated with the physical material properties (stress and strain) of the interconnect material. In addition, these aluminum wires are buried in an insulating coating (usually SiO_2). X rays are ideally suited to probe these buried metallic wires and establish the metallic grain orientation and strain along the wire length. Strain is determined by measuring small changes in the crystal plane d spacing. Because the aluminum grain size is typically about a micron, the instrumental challenge is to carry out x-ray crystallography on micron-sized samples.

Conventional crystallography uses a fixed photon energy and scans the sample angle. If this were done with a micron-sized sample and a micron-sized x-ray probe, the sample and x-ray beam would rapidly become misaligned, because the precision of regular goniometers is typically tens of microns. We have adopted the alternative approach of fixing the sample position and scanning the photon energy. The procedure is threefold: record the Laue pattern of the sample grain with white light, index its orientation, and then determine the photon energy of the individual Laue spots. This procedure allows the determination of the lattice spacing of the planes of interest.

In the experimental arrangement, the monochromator crystals are mounted off-axis, which enables us to switch between white and monochromatic light while continuing to illuminate the same spot on the sample. Spot sizes achieved to date are 0.8 μm FWHM. The sample is inclined at 45° to the white x rays, and the CCD is positioned above the sample to record a Laue pattern at 90° to the input beam.

A typical Laue image from a single aluminum grain on a silicon (100) substrate is shown in Figure 1. The

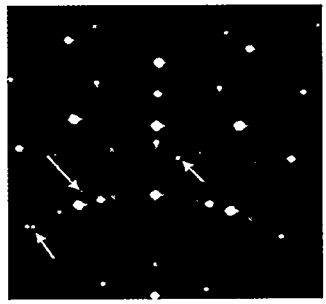

Figure 1

Laue pattern of a single grain in the aluminum interconnect (some spots indicated) and the Laue pattern from the silicon substrate. Time for this exposure was 0.5 s.

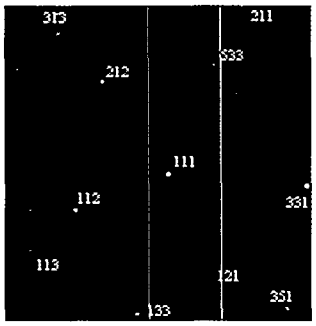

Figure 2

Laue pattern with indexation from just the aluminum grain after digitally subtracting the silicon Laue pattern.

bright symmetric spots are those of the silicon substrate, but the weaker asymmetric spots indicated are those of an aluminum grain misoriented with respect to the silicon substrate. By digitally subtracting the silicon spots, we get a Laue pattern that can be indexed as shown in Figure 2. With the spots indexed, the d spacing of the relevant planes can be measured by switching to monochromatic light and scanning the photon energy to determine the centroid of the peak reflectivity.

As an example, the photon energy of the central aluminum (111) spot was measured to be 7232 eV. Accurate Bragg angles for the separate spots are also required for accurate determination of d spacing. With the existing hardware, typical d spacings have been measured with an accuracy of 1 part in 1000, which confirmed the indexation; however, to measure strain within the aluminum grain, d-spacing measurements some 10 to 100 times better are required. This improvement is under way with the delivery of a new custom-built instrument capable of the required angular stability.

Investigators

A.A. MacDowell, H.A. Padmore, and A.C. Thompson (Berkeley Lab), C.H. Chang and J.R. Patel (Berkeley Lab and Stanford Synchrotron Radiation Lab).

Publications

1. C.H. Chang et al., "Grain orientation mapping of passivated aluminum interconnect lines with x-ray micro-diffraction," *Mat. Res. Soc. Symp. Proceedings* (1998), Vol. 524, pp. 55–58.
2. A.A. MacDowell et al., "Progress towards submicron hard x-ray imaging using elliptically bent mirrors and its applications," *SPIE Proceedings* (1998), Vol. 3449, pp. 137–144.

Funding

U.S. Department of Energy, Office of Basic Energy Sciences, and Intel Corporation.

Probing Impurity Localization at a Buried Interface: The CdS/Cu(In,Ga)Se_2 Thin-Film Solar Cell Heterojunction

Making solar energy practical depends on finding materials that make solar cells more efficient and production more cost effective. One material that may prove useful, a thin film of Cu(In,Ga)Se_2 dipped in CdS, has been characterized by researchers using complementary techniques. By applying both surface-sensitive and bulk-sensitive analyses, scientists were able to determine the location of beneficial impurities in the thin film and thus have found new reason for optimism about this material. What's more, they have demonstrated how these techniques can shed light on the workings of a host of other materials.

One of the most challenging tasks for future generations will be to solve the problem of how an increasing demand for energy can be met with a decreasing supply of natural resources. Among the possible solutions to this problem, the conversion of solar energy ranks as one of the prime candidates, because we have a virtually unlimited supply of solar fuel. However,

currently available solar cells are too expensive and are not efficient enough to produce electricity at costs that are competitive in the energy market.

One of the strategies to overcome this "market barrier" is to use materials with strong optical absorption, such as $Cu(In,Ga)Se_2$, which allow the production of highly efficient thin-film solar cells by low-material-input and industrially standardized preparation techniques. Photovoltaic conversion efficiencies of up to 17.7% on a laboratory scale and up to 11.75% for large-scale devices (51 cm^2) have been achieved with cells based on a $CdS/Cu(In,Ga)Se_2$ interface.

An international team of scientists from industry, academia, and government laboratories used Beamline 8.0 with the ellipsoidal mirror analyzer and soft x-ray fluorescence endstations to investigate the electronic structure of the buried $CdS/Cu(In,Ga)Se_2$ interface. This interface is responsible for creating the photovoltaic current when the solar cell is illuminated. Of particular interest are an understanding of the favorable influence of sodium impurities, which diffuse into the $Cu(In,Ga)Se_2$ film during production, and information about the abruptness of the $CdS/Cu(In,Ga)Se_2$ interface and its consequences for the electrical performance of the device.

By combining a surface-sensitive method (photoelectron spectroscopy, or PES) and a bulk-sensitive technique (x-ray emission spectroscopy, or XES), and by investigating a series of $Cu(In,Ga)Se_2$ samples with different CdS overlayer thicknesses, the location of the sodium impurities can be very accurately determined, as demonstrated in Figures 3 and 4. Without a CdS overlayer, all sodium is localized at the $Cu(In,Ga)Se_2$ surface. This information is derived from the fact that, for both bulk and surface-sensitive measurements, the sodium signal can be completely erased by a short ion-sputtering step, which removes the first few atomic layers from the surface (Figure 3a–c, Figure 4a,b). In the case of a

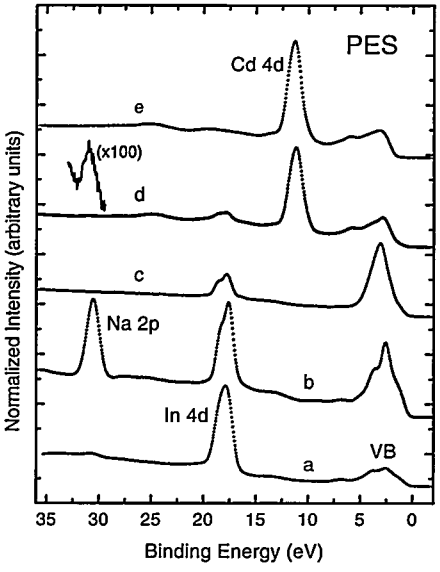

Figure 3

Photoelectron spectroscopy (PES) of $Cu(In,Ga)Se_2$, a potential material for use in highly efficient solar cells, (a) at hν = 800 eV; (b) at hν = 208 eV; (c) sputtered, at hν = 208 eV; (d) with 5-nm CdS dip, at hν = 208 eV; and (e) with 200-nm CdS dip, at hν = 208 eV. The sodium peak is evident in untreated samples but is not apparent in the sputtered sample. The CdS-dipped samples show hardly any sodium peak with this surface-sensitive technique.

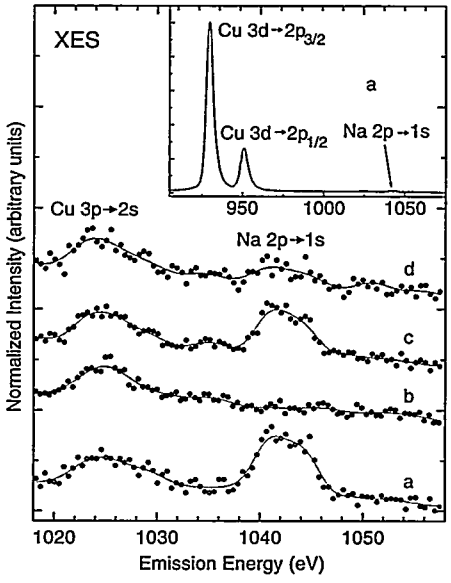

Figure 4

X-ray emission spectroscopy (XES) shows that sodium is still present in the CdS-dipped samples. As with photoelectron spectroscopy, comparison of (a) pristine $Cu(In,Ga)Se_2$ and (b) sputtered $Cu(In,Ga)Se_2$ shows that sputtering removed the sodium. Surprisingly, however, spectra for the samples with (c) 5-nm and (d) 100-nm CdS dips showed direct evidence that sodium is localized at the buried interface.

CdS overlayer, hardly any sodium signal can be detected in the surface-sensitive measurements (Figure 3d,e), whereas the bulk-sensitive XES experiments clearly show the presence of sodium (Figure 4c,d). For CdS overlayer thicknesses commonly employed in solar-cell production (15–30 nm), sodium is clearly detectable at the interface. This finding goes against the usual assumption that the sodium contamination at the Cu(In,Ga)Se_2 surface is removed by the CdS deposition in an aqueous solution. In contrast, sodium is localized at the buried interface, as depicted in Figure 5, and hence is expected to influence the electronic structure of the semiconductor junction and the overall solar-cell performance.

It is the unique combination of x-ray emission spectroscopy, photoelectron spectroscopy, and a high-brightness synchrotron light source such as the ALS that enables investigations of buried interfaces and impurities as in the present case. (The sodium content at the buried interface is less than 1% of a surface monolayer!) And even though today only very few experimental setups of this kind are available, it is easy to foresee a high demand for the investigation of buried interfaces in semiconductors, magnetic structures, organic light-emitting devices, and a large variety of other materials by these techniques.

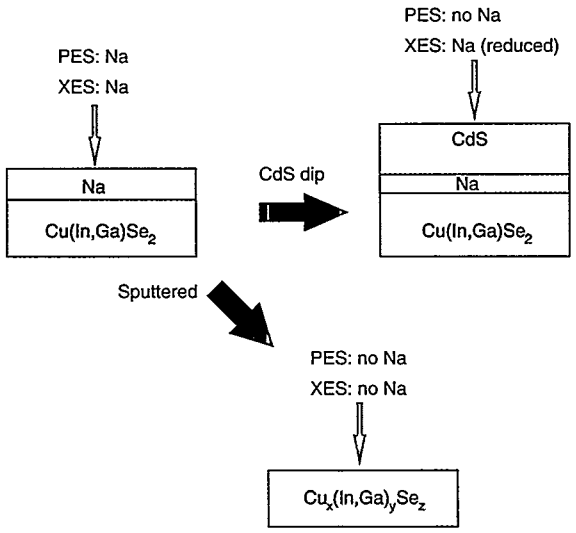

Figure 5

Changes to a thin film of Cu(In,Ga)Se_2 with sputtering and with CdS dipping, and how photoelectron spectroscopy (PES) and x-ray emission spectroscopy (XES) results reflect those changes.

Investigators

C. Heske (Berkeley Lab); D. Eich, R. Fink, and E. Umbach (Universität Würzburg); S. Kakar (University of California, Davis/Livermore); M.M. Grush and T.A. Callcott (University of Tennessee); T. van Buuren, C. Bostedt, and L.J. Terminello (Lawrence Livermore National Laboratory); F.J. Himpsel (University of Wisconsin-Madison); D.L. Ederer (Tulane University); R.C.C. Perera (Berkeley Lab); W. Riedl (Siemens AG Corporate Research and Development); and F. Karg (Siemens Solar GmbH).

Funding

The Bayerische Forschungsstiftung within the FORSOL project; U.S. Department of Energy, Office of Basic Energy Sciences; and the DAAD HSP-III program.

EUV Interferometry: Metrology for Future Microchip Generations

For 30 years, the density of circuit elements on microchips has doubled roughly every two years, resulting in progressively smaller, faster, and cheaper computers. Continuing this rate of progress into the next century requires extremely precise and accurate optical components that can focus light sharply enough to "etch" up to a billion circuit elements onto a square centimeter of silicon. Crafting such precision optical components requires equally precise and accurate measurement tools, such as the phase-shifting, point-diffraction interferometer (PS/PDI) that has been developed and tested at the ALS.

The size of the circuit features that can be mass-produced on a microchip depends on the wavelength of light used to etch the features onto the chips. Past reductions in feature size have been primarily achieved by using shorter wavelengths of light. However, industry experts predict that, in a few years, we will reach a wavelength at which the refractive lenses used for focusing will absorb light

rather than transmit it. Anticipating this roadblock, the semiconductor industry has developed a "road map" that explores several options for getting around this limit within the next decade. At the December 1998 Next Generation Lithography meeting organized by Sematech, extreme ultraviolet (EUV) lithography was identified as the leading advanced technology for implementation in the "post-optical" period.

Extreme ultraviolet lithography uses the reflection (as opposed to refraction) of light at 13 nm, a wavelength chosen to obtain optimum performance from curved multilayer mirrors. These mirrors are made by coating a substrate with a large number of alternating scattering and transmitting layers whose thicknesses are less than the distance over which the radiation is absorbed. The mirrors are curved to reduce and focus the circuit patterns onto the microchip, and the thicknesses of the layers are chosen so that the light waves reflecting from each layer add constructively. Since this is a resonant system tuned to 13 nm and is sensitive to changes in wavelength, angle of incidence, and layer thickness, aberrations caused by coating defects and thickness errors can only be measured by using 13-nm light. Furthermore, the required fabrication tolerances are incredibly stringent. To verify the shape of such a mirror, we need a measurement tool with an accuracy of 0.10 nm—about the size of a single atom!

The phase-shifting, point-diffraction interferometer (PS/PDI) is a measurement tool designed to meet these specifications. This interferometer is permanently installed on Beamline 12.0.1, which is the world's best available source of coherent 13-nm light. The beam first passes through a pinhole, which produces a spherical wave front. A diffraction grating splits the light into several beams that reflect off of the mirrors being tested. One beam (the test beam) passes through a window large enough to preserve the aberrations picked up from the test mirrors. Another beam (the reference beam) passes through a second pinhole that is small enough to "filter out" the aberrations, again producing a uniform, spherical wave. When the two beams interfere, they produce a pattern of light and dark fringes that yields information about flaws in the test mirrors.

To determine the interferometer's accuracy, the test-beam window was replaced with another pinhole, in effect producing two reference beams.

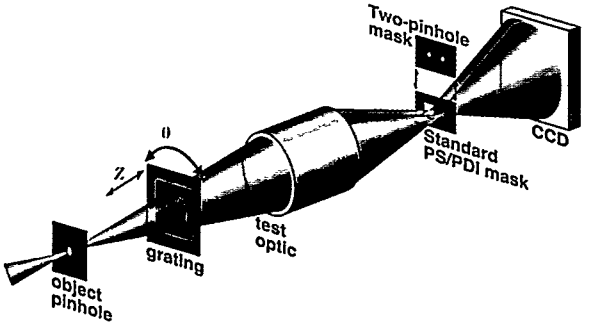

Figure 6

Schematic diagram of the phase-shifting, point-diffraction interferometer showing the light path from the source through the components of the interferometer to the screen that records the interference (fringe) pattern.

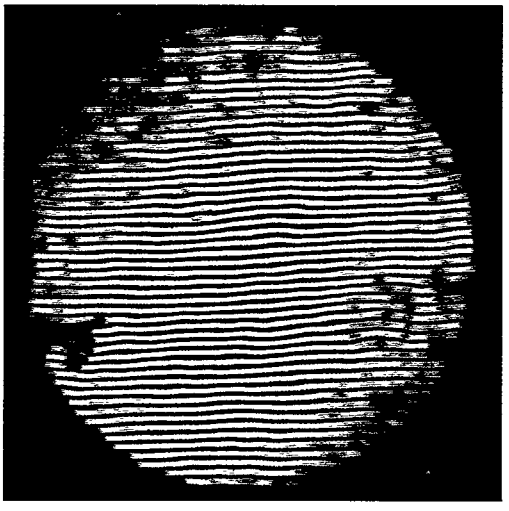

Figure 7

The fringe pattern from a test mirror contains information about figure errors in the mirror shape together with systematic errors inherent in the instrument itself. To separate out the latter, researchers use the fringe pattern from a "null" test with a second pinhole and no mirror to measure the interferometer accuracy.

The interference between the two reference beams reveals the systematic error introduced by the interferometer itself. This was found to be just under 0.05 nm, which is better than the design goal of 0.10 nm and well beyond the current state of the art in optical fabrication. Although any commercially viable chip manufacturing process would still be nearly a decade away, this achievement represents an important milestone that paves the way for the use of EUV light in producing the next generation of microchips.

Investigators

K.A. Goldberg, P. Naulleau, S. Lee, C. Chang, C. Bresloff, and P. Batson (Berkeley Lab) and J. Bokor and D.T. Attwood (University of California, Berkeley, and Berkeley Lab).

Funding

EUV Limited Liability Corporation under a CRADA with the Virtual National Laboratory (Lawrence Livermore National Laboratory, Sandia National Laboratories, and Berkeley Lab); additional funding from the Semiconductor Research Corporation and DARPA.

Publications

1 P. Naulleau et al., "Characterization of the accuracy of EUV phase-shifting point diffraction interferometry," *SPIE Proceedings* (1998), Vol. 3331, p. 114.

2. K.A. Goldberg et al., "High accuracy interferometry of EUV optical systems," *J. Vac. Sci. Technol. B* **16** (1998).

Multi-Atom Resonant Photoemission Demonstrated

In experiments at the ALS, researchers from the University of California at Davis and the Berkeley Lab have demonstrated a new x-ray spectroscopic technique called multi-atom resonant photoemission (MARPE). In the past, x-ray techniques such as x-ray absorption, x-ray emission, and photoemission have not been able to directly identify the atoms neighboring the absorbing atom, particularly for atoms that are close in atomic number. Now MARPE promises to provide much information about neighboring atoms, including their identities, bonding properties, and magnetic order.

Spectroscopic techniques that use x rays to excite core electrons at characteristic photon energies are well known for their elemental, chemical, and magnetic specificity as far as the absorbing atom is concerned. But these techniques do not permit directly probing element-specific properties for atoms neighboring the absorber, and they often require the atoms to have significantly different atomic numbers or necessitate the use of detailed theoretical modeling to deduce such information. Using the advanced photoelectron spectrometer/diffractometer on Beamline 9.3.2 at the ALS, our group has demonstrated a new technique called multi-atom resonant photoemission (MARPE) that promises to provide comparable information on neighboring atoms and to be applicable over virtually the entire periodic table (excluding only hydrogen and helium).

In normal resonant photoemission, which is a well-known intra-atomic process involving only a single atom, the photoelectron signal from a given core energy level (a bound-to-free transition) increases sharply when the photon energy matches that needed to excite a strong resonant transition from a lower-energy core level to its first excited state (a bound-to-bound transition), and this excitation is followed immediately by the reverse transition back

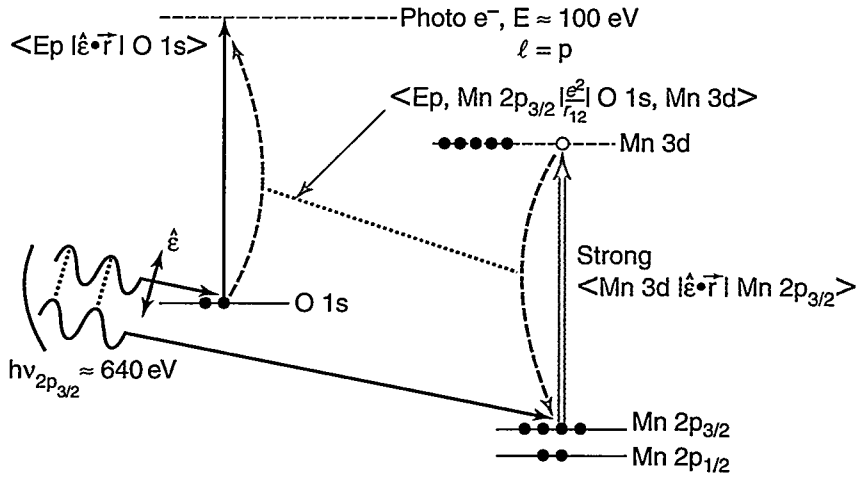

Figure 1

The principle of multi-atom resonant photoemission (MARPE). When the photon energy is tuned to a strong bound-to-bound excitation on a near-neighbor atom (orange), the intensity of the photoemission from the core level in the photoemitting atom (green) is significantly enhanced due to the electromagnetic disturbance on the neighbor propagating to the photoemitter.

to the lower level. This downward transition then contributes to the excitation of a photoelectron, thereby adding to the normal nonresonant signal. In multi-atom resonant photoemission, the process is interatomic and involves two atoms: photoelectrons are emitted from one atom, and the resonant transitions occur on neighboring atoms. The enhancement of the photoemission occurs because of a coupling between emitter and neighbor atoms due to the Coulomb interaction, so that the electromagnetic field generated in the downward resonant transition on the neighbor is transferred to the atom responsible for photoemission. Since the resonance occurs at a photon energy characteristic of each neighbor element (via a core-level excitation energy), the identity of the neighbor atom is established.

To demonstrate this effect, we have to date studied metal oxides (MnO, Fe_2O_3, and $La_{0.7}Sr_{0.3}MnO_3$) and the metallic alloy system Cr/Fe. In the case of MnO, we measured photoelectron spectra from the oxygen 1s core level. We found an enhanced signal—the signature of the MARPE effect—when the photons excited transitions from manganese 2p to manganese 3d levels (the 2p resonances). The enhancement of the peak intensity was about 40%, and the enhancement integrated over the relevant spectral region was about 11%, with the latter being in rough agreement with the value calculated from a simple extension of the theory for single-atom resonant photoemission of about 2.5%. We have recently made more accurate theoretical calculations that are in much closer agreement with experiment. We found larger effects in the other compounds, with peak values up to 105% and energy-integrated values up to 29% for several resonances in $La_{0.7}Sr_{0.3}MnO_3$. We also found enhancement of manganese photoemission due to lanthanum 3d resonances, a second nearest-neighbor interaction. Finally, the Cr/Fe alloy system shows similar effects, with interesting variations as a function of composition.

The next step is to explore the systematics of MARPE and its range of applicability. Possible applications include determining the relative numbers of each type of neighbor atom, bond distances, bond types, chemical shifts, and magnetic order and deriving this information for alloys, complex or strongly correlated materials, magnetic materials, semiconductors, environmental samples, buried interfaces, adsorbates, and perhaps gas-phase molecules. We have already verified that detection of secondary processes, such as x-ray fluorescence or Auger electrons, also reveals the effect. Fluorescence detection will make it possible to probe deeper below the sample surface than with photoemission, thereby yielding information about bulk properties and possibly extending the applications to systems of biological interest.

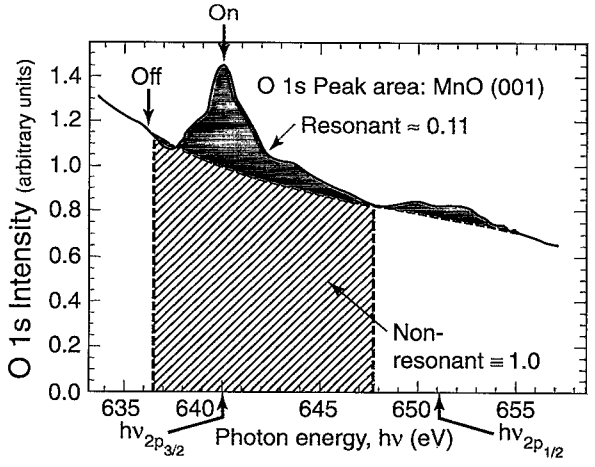

Figure 2

Demonstration of MARPE for O 1s emission from MnO when the photon energy (hν) is tuned to the Mn $L_{2,3}$ ($2p_{1/2}$ and $2p_{3/2}$) edges. The resonant enhancement is shown in orange, and the expected intensity in the absence of the resonance is in cross-hatched red. For the $2p_{3/2}$ resonance, the enhancement is 40% in peak height and about 11% in integrated peak area.

Investigators

A. Kay , S. Mun, C.S. Fadley and R. Denecke (University of California at Davis and Berkeley Lab); E. Arenholz, M.A. Van Hove, and Z. Hussain (Berkeley Lab); and J. Garcia de Abajo (Berkeley Lab and Universidad del Pais Vasco/EHU, Spain).

Publications

1 A. Kay et al., "Multi-atom resonant photoemission: A new tool for determining near-neighbor atomic identities and bonding," *Science* **281** 679 (1998).

2. J. Garcia de Abajo, C.S. Fadley, and M.A. Van Hove, "Multi-atom resonant photoemission: Theory and systematics," *Phys. Rev. Lett.*, in press.

Funding

U. S. Department of Energy, Office of Basic Energy Sciences; The Miller Institute; the Deutsche Forschungsgemeinschaft; and the Basque government.

Beyond the Chemical Shift: Vibrational Fine Structure in XPS of Adsorbed CO

The emission of an inner-shell photoelectron leaves a molecule in one of several different vibrational states, thereby causing the peaks of the photoelectron spectrum to divide up into several narrowly spaced peaks (fine structure). It had been assumed that vibrational fine structure for molecules adsorbed to metal surfaces would be broadened by interactions between the molecule and the surface and hence would not be resolvable. High-resolution measurements by a Swedish group at the ALS have shown that this is not the case. The researchers also observed a detailed dependence of the fine structure on the local geometry of the adsorbed molecule. These results provide a new tool for interpreting x-ray photoelectron spectra of adsorbed molecules.

Core-level x-ray photoelectron spectroscopy (XPS) has been a workhorse of modern surface science. The binding energies of atomic core levels are sensitive to the local chemical environments of the atoms. These variations in binding energy are called chemical shifts. Utilization of chemical shifts allows researchers to identify and characterize atoms and molecules adsorbed on surfaces. Distinct chemical shifts are found for different substrates and for different adsorption sites.

Core-level ionization in molecules gives rise to an electronic redistribution that modifies the molecular potentials. This change induces vibrational excitation in the core-ionized final state. In gas-phase measurements, many properties of molecules can be routinely assigned by using the characteristic vibrational fine structure of XPS main lines. For molecules adsorbed on a metal surface, however, the general assumption has been that the XPS main lines of the adsorbates are broadened by the coupling to the metal. For this reason, no detailed separation of the electronic and vibrational contributions was thought to be possible. Our work with CO adsorbed on Ni(100), however, shows that very small core-level vibrational splittings in adsorbates can be clearly resolved and that electronic and vibrational contributions can be separated (Figure 3).

In order to perform these experiments, the high photon flux and high energy resolution of a third-generation synchrotron source are crucial. Our measurements were performed on undulator Beamline 8.0.1 at the ALS with the Uppsala surface-physics endstation, which is equipped with a Scienta SES-200 hemispherical electron analyzer. The overall energy

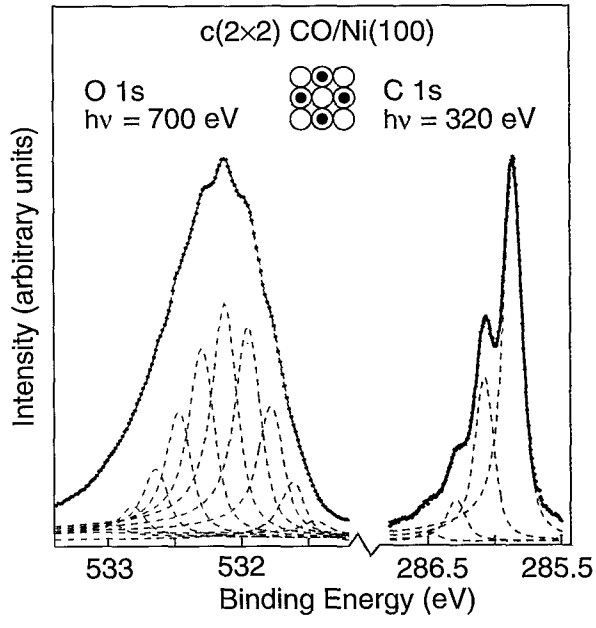

Figure 3

Vibrational fine structure in the carbon 1s and oxygen 1s photoelectron lines of CO adsorbed on Ni(100) in a c(2×2) superstructure. The fine structure (spacing between the peaks), which is due to the intramolecular stretch vibration, is 217.8 ± 2.2 meV in the carbon 1s line and 173 ± 8 meV in the oxygen 1s line.

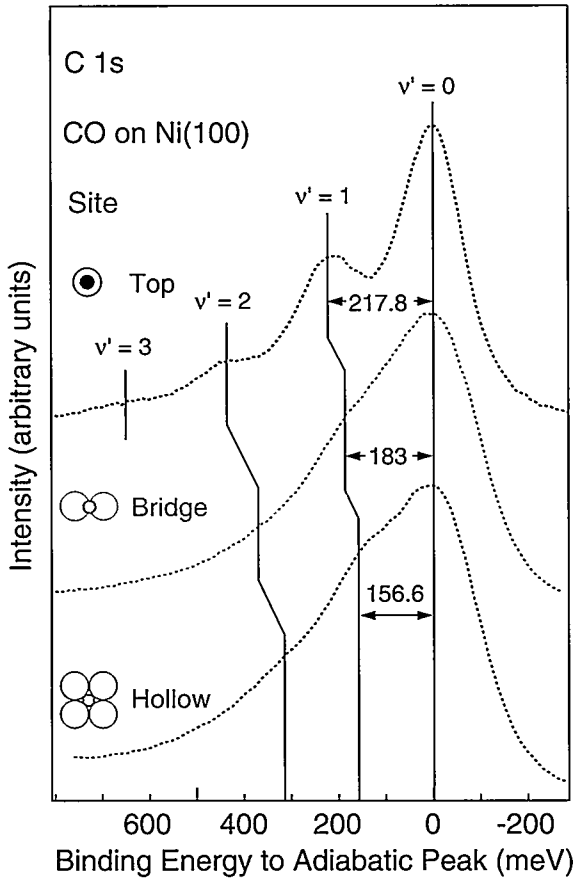

Figure 4

Vibrational fine structure as a function of substrate coordination. The fine structure in the carbon 1s line is shown for CO molecules in top, bridge, and hollow adsorption sites. The photon energy is 320 eV for the top site and 426 eV otherwise.

resolution was better than 10,000 between photon energies of 250 eV and 700 eV.

The observation of vibrational fine structure in the XPS main lines of adsorbed molecules leads to a significantly enhanced understanding of the core-ionized adsorbate. We can extract information about the electronic and geometric structure that exceeds what was previously possible with XPS. In general, we can extend the powerful tools of vibrational analysis from gas-phase to adsorbed molecules. On a fundamental level, we confirm that dynamic metallic screening is of paramount importance in describing core ionization of adsorbates on metals. The XPS main line is found to represent the fully screened final state. Moreover, we can determine the binding energy of the adiabatic transition experimentally, which makes a direct comparison to calculated binding energies easier.

In addition, we investigated how the vibrational fine structure of adsorbed CO depends on the substrate and on the adsorption site. This dependence is shown in Figure 4 for three different adsorption sites. From these measurements, we could extract the geometric changes upon core ionization within the CO molecule in different sites.

The most general conclusion we can draw from the present findings is that they provide a line-shape parameterization based on a few physically relevant parameters. In particular, this parameterization relates the XPS line profile to ground-state properties like bond lengths and force constants. We anticipate that this relationship will be useful for researchers trying to interpret core-level photoelectron spectra of adsorbed molecules.

Investigators

A. Föhlisch, N. Wassdahl, J. Hasselström, O. Karis, N. Mårtensson, and A. Nilsson (Uppsala University, Sweden) ; D. Menzel (Technische Universität München, Germany); and C. Heske (Berkeley Lab).

Publications

1. A. Föhlisch et al., "Beyond the chemical shift: Vibrationally resolved core-level spectra of adsorbed CO," *Phys. Rev. Lett.* **81**, 1730 (1998).
2. A. Föhlisch et al., "Vibrational fine structure in core level photoelectron lines of adsorbed molecules: System dependent effects," *J. Electr. Spectr. Relat. Phenom.*, in press (1998).

Funding

Swedish Natural Science Research Council (NFR) and Göran Gustavsson Foundation for Research in Natural Sciences and Medicine.

Macromolecular Structures of Humic Substances

Formed by the biochemical transformations of plant and animal residue, humic substances constitute a major fraction of the dissolved and particulate organic carbon in natural ecosystems. The ubiquitous presence of humic substances in soils, combined with their ability to provide multiple sites for reaction, makes them relevant in numerous geochemical processes, such as mineral weathering, nutrient bioavailability, contaminant transport, colloid stability, and global carbon and nitrogen cycling. The reactivity of humic substances depends on their functional-group chemistry and macromolecular structure (size and shape), which are influenced by the composition of the reacting media (solution chemistry, interactions with solid particles). ALS researchers used the high-resolution x-ray microscope at Beamline 6.1.2 to study how changes in reacting media affect the structure of humic substances.

Although significant information on the structural composition of humic substances has been previously obtained by using electron microscopy, nuclear magnetic resonance, and infrared spectroscopy, direct evidence of the structural transformations in humic substances associated with changes in solution chemistry has yet to be documented. To understand this correlation, we conducted experiments on humic substances isolated from river water (fluvial) and soil (terrestrial) samples, in addition to experiments conducted on undisturbed soils.

The macromolecular structures of humic substances were examined in situ by using the high-resolution x-ray microscope at Beamline 6.1.2. The observations were made under varying chemical conditions: pH (3–12), ionic strength (0.01–2 M NaCl, $CaCl_2$), organic molecule concentration (0.03–17 g/L as carbon), and complexing cations (1 mM copper (II), iron (III) nitrate, and chloride). The studies were also conducted in the presence of common soil minerals such as goethite, calcite, and clays (kaolinite, montmorillonite). The results suggest that the correlation between humic substances' macromolecular structure and solution chemistry can be summarized as follows.

First, the macromolecular structures are different under different solution chemical conditions, in contrast to the previously held belief that the molecules elongate in alkaline solutions and coil in acidic, high-ionic-strength solutions. Although some of the structures found in this study were also reported earlier in electron and atomic force microscopy studies of dried humic substances, such structures cannot be correlated with their solution chemistry by these methods, because sample drying causes significant chemical changes in the samples (e.g., increases in the concentration of the humic substances).

Second, the chemical conditions under which terrestrial and fluvial humic substances assume a particular configuration are different. This suggests that the observed structural differences are a reflection of the higher aromatic content and the low solubility of terrestrial humic substances relative to fluvial humics.

Third, except for the humic substances in alkaline solutions, no single specific macromolecular structure was found to represent humic substances under a set of chemical conditions. Dilute, alkaline humic substance solutions commonly exhibited small aggregates without any other structures.

The solution chemical conditions examined in this study are relevant to those found in nature (marine, fluvial, and soil). Changes in these conditions can cause dynamic structural transformations in humic substances and significantly influence organic molecule retention and preservation by natural systems. Further studies are in progress to evaluate the influence of soil mineral surface chemistry on the mineral-sorbed organic molecules.

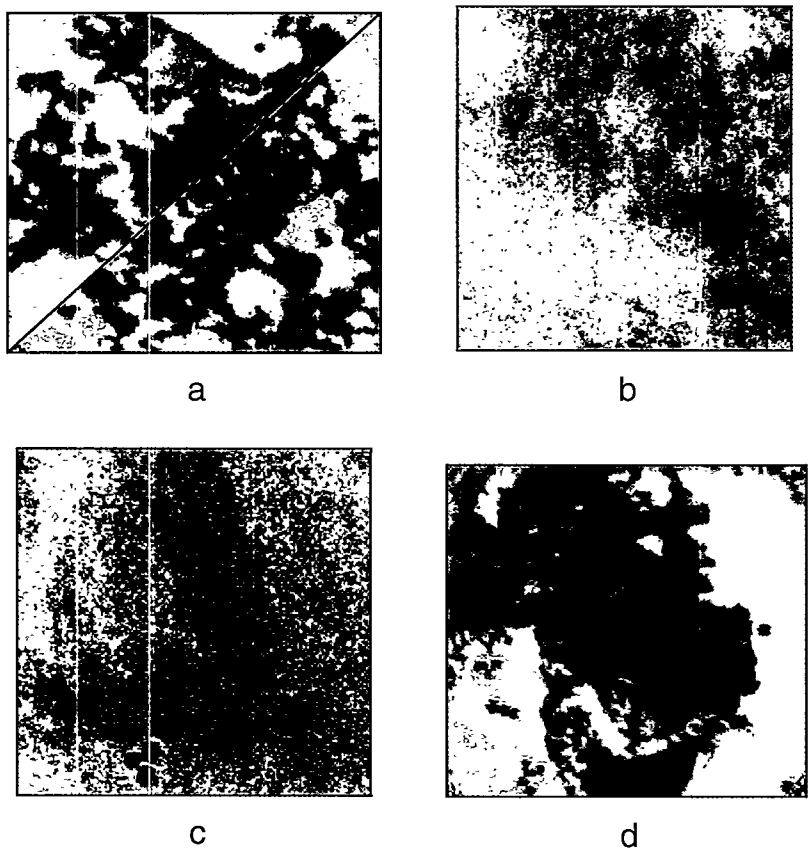

Figure 1

The macromolecular structures of humic substances were affected by solution pH, ionic strength (type and concentration of electrolyte), and the type (fluvial or soil) and concentration of the humic substances. Humics formed globular aggregates and coils in acidic NaCl solutions (a) and dispersed completely into small aggregates in alkaline solutions of pH > 7.0 (b). Additions of di- and trivalent cations to humic substances in solution not only promoted their precipitation at a low humic substance concentration, but also modified their molecular structures. For instance, at dilute Ca^{2+} and humic substance concentrations, fluvial fulvic acid formed thin net-like structures (c). The structures grew denser and formed coils as the humic substance concentration increased (d).

Investigators

S.C.B. Myneni, J. Brown, and W. Meyer-Ilse (Berkeley Lab) and G.A. Martinez (University of Puerto Rico).

Funding

Berkeley Lab, Laboratory Directed Research and Development Fund; U.S. Department of Energy, Office of Biological and Environmental Research.

Publications

1. S.C.B. Myneni et al., "Applications of soft x-rays in probing the chemistry of natural organic molecules," in *Proceedings of the 1998 American Chemical Society National Meeting* (Boston, 1998), Vol. 38, pp. 57–58.

BIOSCIENCES I: PROTEIN CRYSTALLOGRAPHY

Structural Genomics of *M. jannaschii*

The DNA sequence of a gene does not always yield the cellular function of the protein coded by the gene, but the three-dimensional structure of the protein can be a sensitive indicator of its function. For example, protein structures are classifiable in terms of a finite set of folds associated with a small list of functions. In the early stages of a pilot study of the bacterium Methanococcus jannaschii, *researchers using protein crystallography at the ALS have determined the structure of a protein of previously unknown function. The structure suggested a small number of possible functions from which biochemical assays were then used to determine the actual function.*

The goal of the Human Genome Project is to determine the DNA sequence of the human genome by the year 2005. One of the important objectives of determining the genomic sequences is to understand the cellular and molecular (biochemical and biophysical) functions of all the gene products (i.e., mostly proteins) encoded in the genomes, but the function of a protein cannot be readily inferred from the DNA sequence of a gene unless that sequence is significantly similar to that of a gene whose function is already known. The current estimate of the percentage of genes with gene products of known function varies from approximately 30% to 60%, depending on the genomes sequenced. Furthermore, an even smaller fraction of the genes have gene products with known molecular functions. In structural genomics, we look for clues to the function of a protein in its three-dimensional structure.

Determining the structures of all the gene products of an organism would be an overwhelming task. Fortunately, the current database of protein structures strongly suggests that most proteins are classifiable in terms of a finite set of folds, the "folding basis set," and that each fold may be represented by a small number of biochemical or biophysical functions. Accordingly, large-scale projects to determine the structures of a few representatives from each fold family can provide a foundation for the functional genomics by identifying molecular functions that can be combined with cellular functions derivable from mutational studies, transcription tracking, translation tracking, and interaction tracking.

To this end, we are using the Macromolecular Crystallography Facility (MCF) at the ALS in a pilot study of the fully sequenced model hyperthermophilic archaebacterium *Methanococcus jannaschii.* We have chosen several gene products from this organism—some with known cellular functions but without known molecular functions, and some without any known functions—and have begun to determine their structures. The long-term goal of this project is to determine the structures of representative gene products in order to establish a folding basis set for the approximately 1800 gene products expressed in the microbe. The principal focus on finding a large number of new folds makes phase determination by multiple-wavelength anomalous diffraction (MAD) analysis a necessity.

Early results have already allowed the roles of two "hypothetical" proteins (proteins for which there is no other protein in the database with a gene having a similar DNA sequence and a known function) to be tentatively identified from their structure alone. With data gathered at the MCF, for example, we have determined the structure of hypothetical protein MJ0577 from *M. jannaschii.* The crystal structure was solved and refined within a few days after data collection was completed. The set of high-quality experimental phases from MAD measurements at the MCF has proven to be the key factor for interpreting and modeling the structures of the protein and ligands. For example, MJ0577 was identified as an ATP-binding protein after examination of the electron density map showed bound ATP.

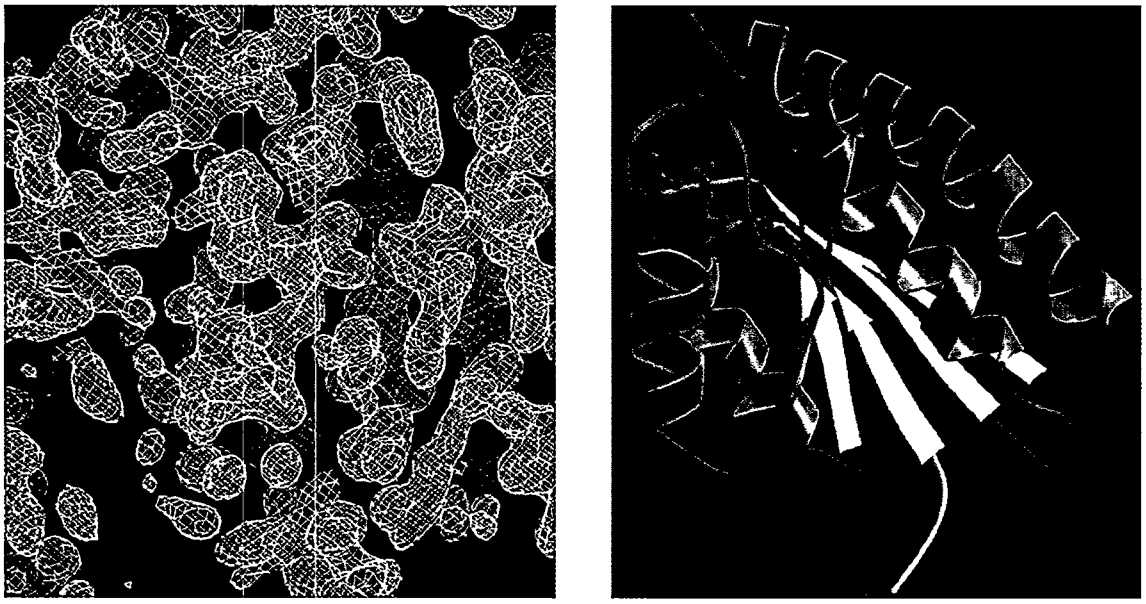

Figure 1

Structure of the hypothetical protein MJ0577 in the hyperthermophilic archaebacterium *Methanococcus jannaschii*, solved at the MCF. (Left) Electron-density map derived from MAD experimental phases clearly shows a bound ATP (yellow stick structure). (Right) The tertiary structure of MJ0577 is a nucleotide binding fold.

The discovery of the ATP immediately narrows down the possible biochemical function of this protein. Biochemical experiments showed that MJ0577 has no appreciable ATPase activity by itself. However, when *M. jannaschii* cell extract was added to the reaction mixture, 50% of the ATP was hydrolyzed to ADP in 1 hour at 80°C. This result indicates that MJ0577 requires one or more soluble components specific to *M. jannaschii* to stimulate ATP hydrolysis, suggesting that this is an ATP-mediated molecular switch analogous to Ras, a GTP-mediated molecular switch that requires GAP to hydrolyze GTP. In these studies, we have shown that MAD experiments can lead to very rapid protein structure determination. Furthermore, in the case of MJ0577, the three-dimensional structure of an unknown protein has provided direct information for functional (biochemical) assignment.

Investigators

T. Zarembinski, L.-W. Hung, J. Mueller-Dieckmann, K.-K. Kim*, H. Yokota, R. Kim, and S.-H. Kim (Berkeley Lab and University of California, Berkeley).

Funding

U.S. Department of Energy, Office of Biological and Environmental Research.

Publications

1. T. Zarembinski et al., "Structure-based assignment of the biochemical function of a hypothetical protein: A test case of structural genomics," *Proc. Natl. Acad. Sci.* **15**, 15189–15193 (1998).

*present address: Gyeongsang National University, Korea.

Structure Determination of Collagenase–Inhibitor Complexes from Microcrystals

Many pharmaceuticals contain molecules called inhibitors that bind to biomolecules in cells and thereby prevent malfunctioning or block invasion by disease agents. Structure-based drug design makes use of three-dimensional, atomic-resolution structures of biomolecules complexed with candidate inhibitors in order to devise pharmacological strategies for disease treatment. As part of a program to develop drugs for inflammatory diseases, researchers from Roche Bioscience have used protein crystallography to obtain high-resolution structures of human collagenase complexed with inhibitors.

Inhibitors of matrix metalloproteases (MMPs) are currently under evaluation for the treatment of cancer and arthritis, because abnormal expression or activity of individual MMPs has been associated with pathological processes, such as the joint destruction that accompanies rheumatoid and osteoarthritis and the metastasis and angiogenesis that support tumorigenesis. Only certain MMPs act within the context of each disease. For example, some members of the collagenase subfamily of MMPs are associated with osteoarthritis. Disease treatment therefore requires development of selective inhibitors of MMPs. The structures of the human collagenase with bound inhibitors provide the basis for understanding the selectivity profile of a novel series of MMP inhibitors that are being investigated as a part of the Roche Bioscience structure-based drug-design program for inflammatory diseases.

X-ray diffraction data from more than 15 collagenase–inhibitor complexes were collected from microcrystals at the Macromolecular Crystallography Facility at the ALS. Obtaining useful data from microcrystals required the use of bright synchrotron radiation. The crystals varied in size, but all had dimensions of several tens of microns to 100 microns and were characterized by resolution limits of 1.8–1.6 Å. Crystals this small were needed to allow for the efficient binding of the inhibitor after soaking, since larger crystals showed lower occupancy of the inhibitor. The space group was C21 with a dimer in the asymmetric unit. Dimensions of the unit cell were a = 135 Å, b = 36 Å, c = 95 Å, and β = 131°. Data sets typically yielded R_{cryst} values of 21–22% and R_{free} values of 25–27%.

Human collagenases generally consist of three distinct domains. The structural features most critical in determining MMP substrate specificity and thereby inhibitor specificity are contained within the catalytic domain. The catalytic domain has a five-stranded beta sheet and three alpha helices, as is found for other MMPs. The catalytic center, defined by beta-strand 4 and the central helix, consists of an active zinc site that is coordinated by three histidine residues and a glutamic acid. The only significant structural differences within the catalytic domains of the various MMPs are the conformations of surface loops, which form "specificity pockets." The specificity pockets for various forms of collagenases have different shapes and sizes.

Diphenylether sulfone compounds are examples of the collagenase inhibitors investigated. Figure 2 shows the structure of one of these complexes obtained with a resolution of 1.6 Å. For these

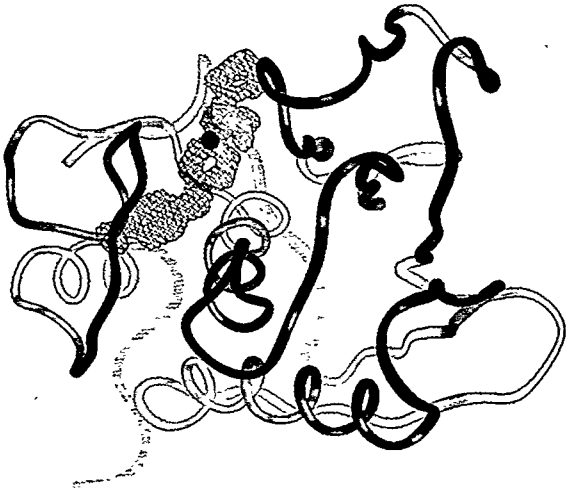

Figure 2

Structure of collagenase complexed with a diphenylether sulfone inhibitor. A resolution of 1.6 Å was obtained from a frozen microcrystal with dimensions of several tens of microns.

inhibitors, the catalytic zinc atom is coordinated with two oxygen atoms within the hydroxamic acid moiety of the inhibitor through a bidentate interaction. The oxygen atoms are 1.9 Å and 2.1 Å away from the zinc atom. The hydroxamate nitrogen is shown to be protonated. One oxygen atom of the sulfone group appears to serve as a hydrogen bond acceptor for the amide nitrogen of a leucine residue on beta-strand 4. These studies demonstrate that MMP inhibitor selectivity is principally determined by the size and shape of the specificity pocket and that induced fit is a factor in selectivity.

Investigators

M. Browner, B. Lovejoy, A. Welch, S. Carr, C. Luong, C. Broka, R.T. Hendricks, J.A. Campbell, K.A.M. Walker, R. Martin, and H. Van Wart (Roche Bioscience).

Funding

Roche Bioscience and the U.S. Department of Energy, Office of Biological and Environmental Research.

Structural Analysis of the Evolutionary Divergence of pNB Esterase

The pNB esterase protein is useful as a catalyst in the chemical synthesis of antibiotics. For such applications, the protein must be able to function in harsh environments. New forms of this protein with improved characteristics have been found through a process called "directed evolution," in which numerous variants of the original form were screened for the desired characteristics. To understand how the improvements arose, we need to know how the protein's structure changed during the evolutionary process. Scientists at the ALS performed multiple-wavelength anomalous diffraction (MAD) experiments at Beamline 5.0.2 to determine the structures of the original and evolved forms of pNB esterase, allowing an analysis of its evolutionary divergence. Among other things, their analysis indicates that early-generation mutations are stabilized by later-generation mutations in a cooperative manner, perhaps explaining how evolution is able to overcome detrimental intermediate states between well-adapted forms.

The protein catalyst pNB esterase has been the subject of two orthogonal directed-evolution screens, one for organic activity and another for thermostability, resulting in proteins with a 100-fold increase in activity and a 17°C increase in stability, respectively. These new proteins have characteristics that make them very useful commercially; however, understanding how these desirable characteristics arose requires structural data.

The structure of the organophile (Figure 3) was determined by a three-wavelength MAD experiment at Beamline 5.0.2. The crystals diffracted reasonably well, which, combined with the high-flux beamline and rapid-readout CCD detector, allowed 540° of data to be collected in three hours. The ALS was chosen as the site to carry out these studies because it provides the opportunity to use a tunable high-flux beamline, allowing initial experimental phasing of the model at high resolution (1.9 Å). The structures of the wild type and thermophile (Figure 4) were also solved with data collected at Beamline 5.0.2.

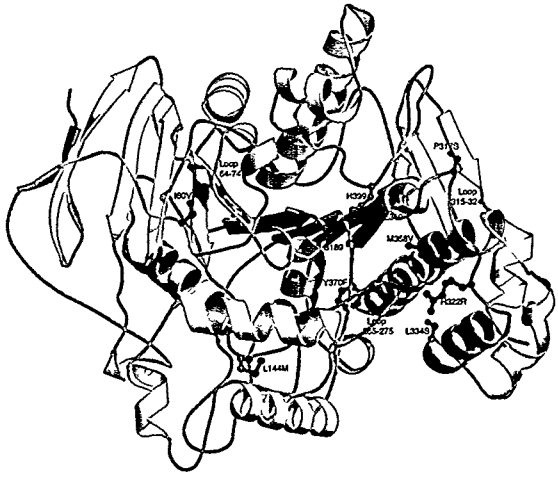

Figure 3

A MolScript ribbon representation of the organophile, showing the catalytic serine in gold, the mutations in red, and the loops that reorganize most significantly in gold.

The three structures, all solved to good resolution (1.5 Å, 1.6 Å, and 2.0 Å for the wild type, organophile, and thermophile, respectively), allow a structural analysis of evolutionary divergence in a setting where startpoint, endpoint, and pathway are all well characterized. Additionally, the three structures allow an analysis of the physical determinants of stability in harsh environments.

The wild-type and evolved esterases have similar overall folds, with an RMS deviation of 0.67 Å between the wild type and the organophile and 0.44 Å between the wild type and the thermophile.

Figure 4

A MolScript ribbon representation of the thermophile, showing the catalytic triad in gold, the mutations in red, and the loops that reorganize most significantly in gold.

Five generations and seven mutations were necessary to optimize the activity of the esterase in organic co-solvents, while eight generations and 13 mutations were necessary to optimize the activity at high temperature. The structures show that early-generation mutations were stabilized by later-generation mutations in a cooperative manner, which allowed the directed-evolution process to traverse complex fitness landscapes, perhaps explaining how evolution is able to overcome detrimental intermediates between well-adapted forms. This suggests that rational design must also consider the nonadditive effects of interacting mutations.

Stability in high-temperature and N,N-dimethylformamide co-solvent environments was found to result from a reduction in the flexibility of surface loops. The study also indicated that thermostability in pNB esterase appears to be caused by improved core packing, helix stabilization, and surface salt bridges, in agreement with other studies. A crystallographic analysis of the wild type and of the products of these screens revealed networks of mutations that collectively reorganized the active site, altering both enzyme activity and stability.

Investigators

B. Spiller (University of California, Berkeley) and R. Stevens (University of California, Berkeley, and Berkeley Lab).

Funding

U.S. Department of Energy, Office of Biological and Environmental Research.

BIOSCIENCES II: SOFT X-RAY MICROSCOPY

X-Ray Microscopic Visualization of Specific Labeling of Adhesive Molecule CD36 and Cytoadherence by *Plasmodium falciparum*–Infected Erythrocytes

As one of the world's most deadly infectious diseases, malaria needs no introduction. Researchers studying the parasites that cause malaria are investigating how the intruders affect their red-blood-cell hosts. One emerging tool for such studies is x-ray microscopy. Working at the imaging x-ray microscope on Beamline 6.1, a group of scientists has been able to probe the mechanism by which malaria parasites cause host red blood cells to adhere to the linings of small blood vessels. They investigated binding between receptors on the cells that line the vessels, including the molecule CD36, and adhesive ligands (binding molecules) on the surface of the infected red blood cells.

During infection with *Plasmodium falciparum* malarial parasites, new parasite-encoded antigens inserted into the red-cell (erythrocyte) membrane result in adhesive changes in the red cell. Adherence between infected red blood cells and venular endothelium (the lining of small veins) results in sequestration of mature parasites in the microvasculature, a condition that contributes to cerebral malaria, the most frequently fatal complication of malaria. Cytoadherence is the result of a specific interaction between receptors on endothelium, including CD36, and adhesive ligands that the parasite inserts into the infected erythrocyte membrane, including the antigenically variant family of molecules known as *Plasmodium falciparum* Erythrocyte Membrane Protein 1, or PfEMP1.

We used soft x-ray microscopy (at Beamline 6.1) to investigate cytoadherence of *P. falciparum*–infected erythrocytes to target cells that express CD36 in static *in vitro* cytoadherence assays. Using Immunogold beads enhanced with silver, we localized CD36 on the surface of intact melanoma cells and throughout Triton-extracted melanoma cells. We examined the orientation of parasites within erythrocytes that bound to target cells and the interactions between the red-cell membrane and the target cell, and we confirmed that fibrillar structures on the surface of melanoma and endothelial cells can be involved in the association between infected erythrocytes and melanoma cells or endothelial cells.

Figure 1

An infected red blood cell attached to an endothelial cell. A clearly visible tether is indicated by the arrow.

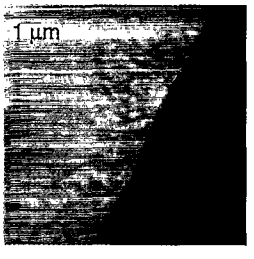

Figure 2

Hair-like structures at the surface of an endothelial cell.

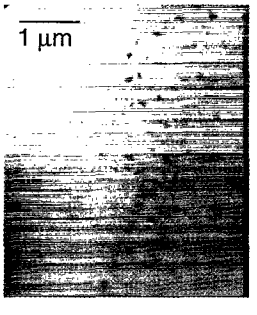

Figure 3

The distribution of CD36, labeled with antibodies that have gold particles attached, on the surface of an endothelial cell.

Our work provides the first published x-ray microscopic images of cytoadherent infected red cells and their interactions with the plasma membrane and surface structures of cells that express CD36. We have demonstrated that parasites may be oriented in various positions within the red-cell cytoplasm during cytoadherence and that fibrillar structures on the surface of the target cells may be involved in cell-cell adherence. Changes coincident with cytoadherence were not detected in either the parasite, the red-cell membrane, or the target cells.

Protein labeling that can be used with high-resolution x-ray microscopy of intact cells will be valuable in further studies of receptor–ligand interactions in malaria as well as in other biological systems. An eventual understanding of the complex biological interactions and mechanisms that result in cytoadherence and sequestration of malaria-infected red cells will contribute to prevention and/or reversal of adherence associated with cerebral malaria.

Investigators

J. Yeung, J.T. Brown, A. Nair, E. Meites, N. Mohandas, W. Meyer-Ilse, and C. Magowan (Berkeley Lab) and R.L. Coppel (Monash University, Australia).

Funding

National Institutes of Health and U.S. Department of Energy, Office of Energy Research. The OKM5 antibody was a gift from Ortho Diagnostics, Raritan NJ, and EA.hyb926 endothelial cells were kindly provided by Dr. Cora-Jean Edgell, University of North Carolina, Chapel Hill.

Publications

1. J. Yeung et al., "X-ray microscopic visualization of specific labeling of adhesive molecule CD36 and cytoadherence by *Plasmodium falciparum* infected erythrocytes," *Res. Commun. Mol. Pathol. Pharmacol.* **99**, 245–258 (1998).
2. C. Magowan et al., "Intracellular structures of normal and aberrant *Plasmodium falciparum* malaria parasites imaged by soft x-ray microscopy," *Proc. Natl. Acad. Sci.* (1997) Vol. 94, pp. 6222–6227.

Purely Spin-Aligned Autoionizing States that Decay to Orbital-Aligned Ionic States: Angular Momentum Sharing in Atomic Valence Electrons

An understanding of how energy, momentum, and angular momentum are distributed in an atom is fundamental to understanding the physics of matter. Though the dynamics of a nucleus and several electrons may seem simple, these many-body systems are incredibly complex, and probing them requires some ingenuity. Using linearly polarized light to excite multielectron atoms and measuring the polarization of the resulting fluorescence, investigators have been able to probe the ionic states formed immediately after photoionization and gain clues as to how the angular momentum of an incoming photon is distributed throughout the excited ion.

Scientists are still working to describe how the conserved quantities of energy, momentum, and angular momentum are distributed, or partitioned, among the parts of a multielectron atomic system. Quantifying this partitioning is important because it provides a direct measure of the degree and nature of the dynamic interactions among the electrons. Photoexcitation provides one of the purest probes for investigating these interactions in detail, since photons interact with and are absorbed by individual electrons. An experimentally observed deviation from independent particle behavior during the photoexcitation process often allows a clear interpretation regarding the character of many-body interactions. For example, quantifying how the single unit of angular momentum (spin) brought into a system by a photon is shared reveals the importance of relativistic spin-dependent interactions among electrons during the photoexcitation and decay processes.

We quantified the partitioning of angular momentum by measuring the polarization of fluorescence radiation from excited ionic states. The excited states were formed via autoionizing doubly excited states, which we produced with linearly polarized synchrotron radiation. To quantify the partitioning, we had to assign discrete Rydberg states with well-defined angular momentum to specific spectral features. Thus, our work required the high energy resolution of Beamline 9.0.1. Combining high resolution with polarization analysis provides dynamic information about energy and angular momentum sharing that cannot be obtained in any other way. Furthermore, the fluorescence approach is the only method for assessing the character of the angular momentum partitioning at energies in the immediate vicinity of the threshold for the residual ionic excitation with constant experimental efficiency and high resolution.

Figure 1 illustrates one application of our methods to atomic argon. From polarization measurements, we determined the alignment, a measure of the differences (anisotropy) in how many substates were formed with each of the magnetic quantum numbers allowed. Both spin and orbital magnetic substates can be aligned. We observed for the first time purely spin-aligned, doubly excited Ar $3p^4[^3P]4p(^2S)$ ns autoionizing states that autoionize into the residual $3p^4[^3P]4p(^2D_{3/2})$ Ar^+ state. The observed states violate the spin conservation expected with linear polarization. During autoionizing decay, the spin alignment of these doubly excited states was transformed into the orbital alignment of the $3p^4[^3P]4p(^2D_{3/2})$ Ar^+ state, as inferred from the polarization of the latter state's fluorescence. The total alignment parameter, plotted in Figure 1, was calculated directly from this measured polarization. It provides a measure of the electronic charge cloud's spatial distribution in this residual ionic state. Assuming the Ar+ states are described by LS coupling, we deconvoluted the measured J-state alignment (alignment of the state with respect to total

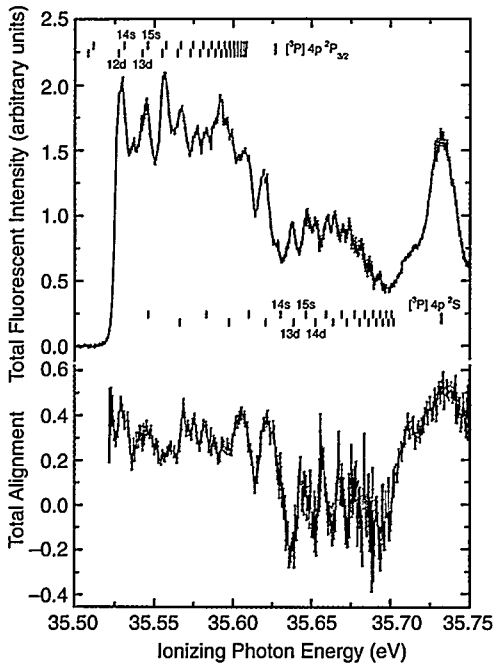

Figure 1

Total fluorescent intensity from the Ar^+ $3p^4[^3P]4p^2D_{3/2}$ state along with the total alignment derived from the linear polarization of this fluorescence. The ionizing photon energies were in the immediate vicinity of the threshold (at 35.52 eV) for production of this residual excited ionic state. The alignment parameter provides a measure of the electronic charge cloud's spatial distribution, which can be used to quantify the relativistic interactions between the autoionizing ns Rydberg electron, the $3p^4$ subshell, and the 4p valence electrons.

angular momentum) in Figure 1 into the charge-cloud distribution (alignment) of the $3p^4$ subshell and of the 4p valence electron. Since the subshells of $3p^4[^3P]4p(^2S)$ ns autoionizing Rydberg states are isotropic, our experimental determination of the anisotropic charge-cloud distributions in the $3p^4$ subshell and the 4p valence electron of the $^2D_{3/2}$ state provides a quantitative measure of the many-body relativistic interactions among the autoionizing ns Rydberg electron, the $3p^4$ subshell, and the 4p valence electrons.

Investigators

K.W. McLaughlin, O. Yenen, and D.H. Jaecks (University of Nebraska-Lincoln).

Funding

National Science Foundation.

Publications

1. K.W. McLaughlin, O. Yenen, and D.H. Jaecks, "Production of purely spin-aligned autoionizing states which decay to orbital-aligned ionic states," *Phys. Rev. Lett.* **81**, 289 (1998).
2. O. Yenen, K.W. McLaughlin, and D.H. Jaecks, "High resolution polarization analysis of the fluorescence from Ar^+ $[^3P]4p^2P_{3/2}$ formed in photoionization," *Phys. Rev. Lett.* **79**, 5222 (1997).

Angle-Resolved, Two-Dimensional Observations of Spin-Orbit Effects in the Photoionization of Neon

There are no exact calculations that can predict, in detail, the structure of atoms and molecules because the electrons in such atoms are not independent, as is customarily assumed in approximations, but rather interact with one another. One signature of such electron interaction, or correlation, is the observation of two excited electrons for one absorbed photon. Since one absorbed photon can excite only one electron directly, the observation of two excited electrons clearly demonstrates electron interaction. Such excitation experiments using the high-precision instrumentation and high-resolution photon sources at the ALS can reveal precise details about the structure and dynamics of atoms and molecules. These types of studies have been conducted successfully on simple targets, such as helium and lithium. The following describes a more complex study on a heavier atom, neon.

The simultaneous excitation of two atomic electrons by a single photon has been the subject of numerous experimental and theoretical investigations. These resonance states reveal higher-order, interelectron correlation effects and provide a more stringent testing ground for the accuracy of existing theoretical and computational methods. Helium,

because of its relative simplicity, has been studied extensively. Neon, however, is more complicated because of its occupied 2p subshell, which leads to a dense grouping of the Ne^+ $2p^4nl$ states and hence more complex resonances. Early photoabsorption results have demonstrated departure from LS-coupling predictions (which neglect spin-orbit effects) by observing the fine-structure splittings of the $2p^4(^3P)3s(^2P_{1/2,3/2})nl$ resonances. These results established the existence of certain spin-orbit effects, but they lacked additional information that would be provided by angle- and energy-resolved measurements. Furthermore, in the earlier cases, only *small* spin-orbit corrections were observed.

We have carried out detailed studies of the photoexcitation and decay mechanisms of doubly excited resonances in neon in order to probe spin-orbit effects in this relatively light system. We measured and identified unexpectedly large spin-orbit-induced effects for a parity-unfavored transition by using angle-resolved, two-dimensional photoelectron spectroscopy. We demonstrated that, for certain neon resonances, the angular distribution of photoelectrons and the ratio of partial cross sections to individual fine-structure levels both exhibit behaviors that deviate markedly from LS-coupling predictions. Such observations provide further quantitative evidence of the breakdown of LS coupling. These results have been corroborated and explained by ab-initio calculations.

We measured two-dimensional (photon energy vs. photoelectron energy) photoelectron spectra at two angles simultaneously, as shown in Figure 2, in order to efficiently observe any effects or features. The apparatus consisted of two highly efficient time-of-flight electron energy analyzers. The measurements were performed on the undulator beamline for high-resolution atomic and molecular studies (Beamline 9.0.1).

The important implication of the detection of prominent spin-orbit effects is that it is not safe to assume the validity of LS coupling, even for low-lying resonances in a system as light as neon. This result could only have been obtained through high-resolution, angle-resolved measurements coupled with the capability to view the data in two dimensions.

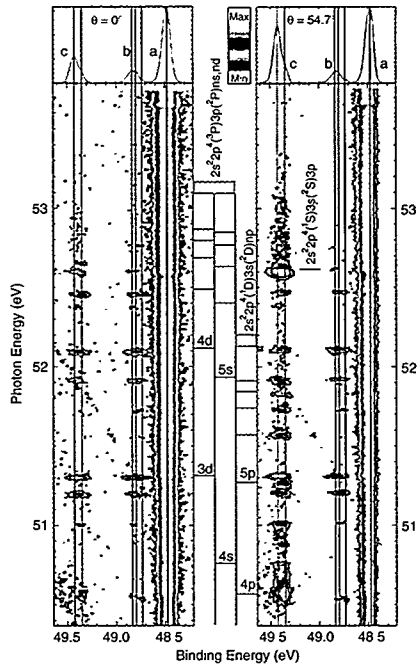

Figure 2

Photoelectron yield as a function of photon energy and binding energy (photon energy minus photoelectron energy) at 0° and at 54.7°. The upper graphs show the spectrum at a photon energy of 51.3 eV, and the vertical bars indicate the positions of the (a) $2s2p^6(^2S)$, (b) $2s^22p^4(^3P)3s(^4P)$, and (c) $2s^22p^4(^3P)3s(^2P)$ fine-structure levels. Looking along the vertical lines (c), it can be seen that several resonances appear at both angles while others disappear at 0°. Since these are parity-unfavored transitions in LS coupling, the appearance of any signal at 0° is an immediate indication of the breakdown of LS coupling.

Investigators

N. Berrah, A.A. Wills, T.W. Gorczyca, E. Kukk, O. Nayandin, and M. Alshehri (Western Michigan University); B. Langer (Fritz-Haber-Institut der Max-Planck-Gesellshaft, Berlin); Z. Pelfli (Clark Atlanta University); and J.D. Bozek (Berkeley Lab).

Funding

U. S. Department of Energy, Office of Basic Energy Sciences.

Publications

1. A.A. Wills et al., "Importance of spin-orbit effects in parity-unfavored photoionization of neon, observed using a two-dimensional photoelectron imaging technique," *Phys. Rev. Lett.* **80**, 5085–5088 (1998).

Beyond the Dipole Approximation: Surprising New Results in Soft X-Ray Photoemission

Photoelectron spectroscopy, in which photoionized electrons are distinguished by their kinetic energies, is a powerful technique, because it directly probes electronic structure in gaseous and condensed matter. It is even more powerful in an angle-resolved mode, where photoelectrons also are distinguished by their direction of emission. Electron ejection probabilities as a function of angle are excellent probes of quantum-mechanical photoemission channels, because they are sensitive to phase differences among these channels. For this reason, angle-resolved photoemission has been used for many years to provide stringent tests of our understanding of the interaction of radiation with matter and as a tool to probe physical and chemical structure. One of the basic approaches to interpreting angle-resolved photoemission spectra is the "dipole approximation," which predicts electron ejection patterns as a function of angle. New work performed at the ALS is helping to define the limits of this approximation and refine our understanding of photoemission.

A mainstay of angle-resolved photoemission is the (electric-) "dipole approximation," which ignores all higher-order photon interactions, such as electric-quadrupole and magnetic-dipole effects, and predicts simple electron ejection patterns as a function of angle. In the dipole approximation, a single parameter, β, completely describes electron angular distributions as a function of the angle, θ, relative to the polarization, **E**, of the ionizing radiation (Figure 3). The solidly colored regions in Figure 4 represent angle-dependent photoemission patterns (with the ejection probability in any direction proportional to the distance from the origin) for different values of β in its range from –1 to 2. For these dipole-approximation patterns, the angular distribution is always symmetrical around **E** and is isotropic for the special case of $\beta = 0$ (Figure 4a).

In the first step beyond the dipole approximation, higher-order photon interactions lead to nondipole effects in these patterns, described by two new parameters, δ and γ. A second angle, ϕ, relative to the propagation direction, **k**, of the ionizing radiation

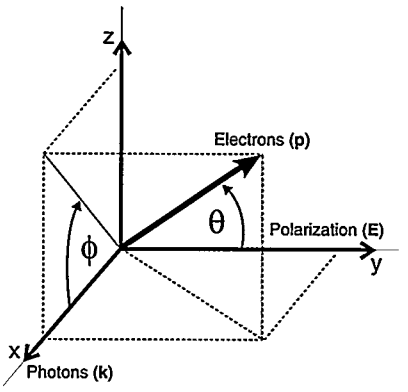

Figure 3

In the dipole approximation, β alone describes electron angular distributions as a function of the angle, θ, relative to the polarization, **E**, of the radiation. Higher-order photon interactions lead to nondipole effects, described by two new parameters, δ and γ, and a second angle, ϕ, relative to the propagation direction, **k**, of the radiation.

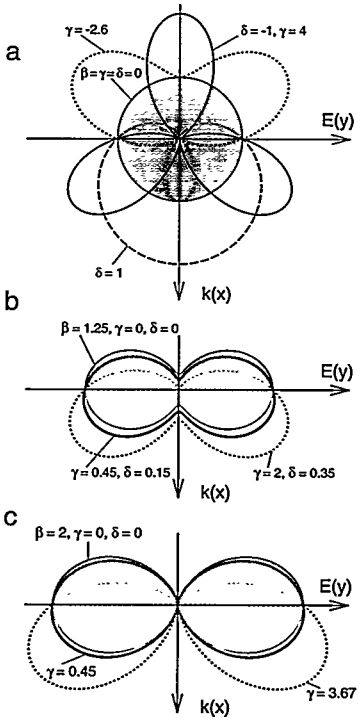

Figure 4

Angle-dependent photoemission patterns, with the ejection probability in any direction proportional to the distance from the origin. Solidly colored regions represent dipole-approximation patterns for different values of β. For these, the angular distribution is always symmetrical around **E** and is isotropic for the special case of $\beta = 0$ (a). The solid red and green curves represent nondipole angular-distribution patterns for 2p (b) and 2s (c) photoemission inferred from Figure 5.

(Figure 3), also comes into play, permitting forward–backward asymmetry. To demonstrate how significant nondipole effects can be for angular-distribution patterns, the dotted red and green curves and all three blue curves in Figure 4 exemplify extreme values for δ or γ. All curves show the same ejection probability along the y axis and in the y-z plane and also show large differences in the forward and backward directions.

To probe the limits of the dipole approximation, soft x-ray photoemission measurements on neon were made at Beamline 8.0. Two-bunch operation was necessary because electron kinetic energies were determined via time of flight (TOF), an efficient technique in which nearly all kinetic energies can be measured simultaneously. The extremely high flux from an ALS undulator was necessary to obtain sufficient signal for precise measurements of δ and γ. Two analyzers, placed at the "magic angle" (θ = 54.7°), where β has no influence, but at different angles ϕ to be sensitive to forward–backward asymmetries, sufficed to measure nondipole effects as a function of photon energy.

Figure 5 superimposes two neon photoemission spectra taken with the "magic-angle" analyzers, one in the y-z plane (orange), the other not (black). The spectra are scaled to each other by using neon KLL Auger lines, which must have isotropic angular distributions ($\beta = \delta = \gamma = 0$). Obvious intensity differences between the 2s and 2p photoemission peaks are due to nondipole effects. The solid red and green curves in Figure 4 represent nondipole angular-distribution patterns for 2p (b) and 2s (c) photoemission inferred from Figure 5. Other spectra show that intensity differences occur at energies as low as 250 eV. Changes in ejection probability as a function of angle are observable well below 1 keV, at photon energies much lower than generally expected for effects beyond the dipole approximation.

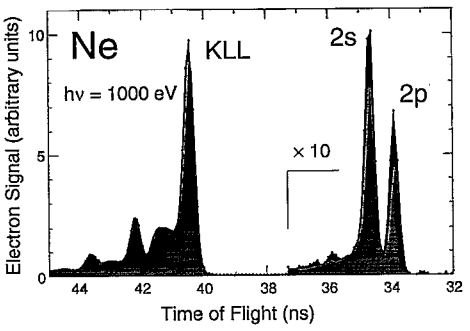

Figure 5

Superimposed neon photoemission spectra taken with the "magic-angle" analyzers, one in the y-z plane (orange), the other not (black). The spectra were scaled to each other by using neon KLL Auger lines. The intensity differences between the 2s and 2p photoemission peaks are due to nondipole effects.

More significantly, measurements on other atoms and molecules demonstrate that "low-energy" breakdown of the dipole approximation is a general phenomenon. It is likely that many applications of angle-resolved photoemission (e.g., most studies of atoms and molecules, band mapping in solids, photoelectron diffraction and holography, orientational studies of adsorbates, etc.) need to include nondipole effects in their analyses. More work to determine the range of validity of the dipole approximation is under way.

Investigators

O. Hemmers, P. Glans, D.L. Hansen, H. Wang, S.B. Whitfield, and D.W. Lindle (University of Nevada, Las Vegas); R. Wehlitz, J.C. Levin, and I.A. Sellin (University of Tennessee, Knoxville); and R.C.C. Perera (Berkeley Lab).

Funding

National Science Foundation; U.S. Department of Energy, Experimental Program to Stimulate Competitive Research; Research Corporation; and The Petroleum Research Fund.

Publications

1. O. Hemmers et al., "Beyond the dipole approximation: Angular-distribution effects in valence photoemission," J. Phys. B **30**, L727 (1997).
2. O. Hemmers et al., "Photoelectron spectroscopy and the dipole approximation," *Synchr. Rad. News* **9** (6), 40 (1996) and erratum **10** (3), 21 (1997).
3. O. Hemmers et al., "High-resolution electron-time-of-flight apparatus for the soft-x-ray region," *Rev. Sci. Instrum.* **69**, 3809 (1998).

Discrimination of Isomeric Photofragments: Photodissociation of Allene and Propyne

Traditional methods for determining the photodissociation products of a molecule are not always adequate, particularly for molecules that can form isomeric products. Such is the case with allene and propyne, molecules whose dissociation products play important roles in combustion and interstellar matter. By combining the well-established technique of photofragment translational spectroscopy with photoionization detection, researchers have succeeded in determining which radicals are produced when light breaks down these molecules. Their results confirm previous studies on allene and settle the debate over what happens to propyne.

For more than three decades, the photodissociation dynamics of molecules and radicals have been investigated by using photofragment translational spectroscopy (PTS). However, certain species cannot be distinguished by PTS with traditional detection methods, such as electron impact. Hydrocarbons, for example, often contain multiple inequivalent C–H bonds. Depending on which bond or bonds rupture, isomeric photofragments can be produced. In the current study, PTS has been coupled with electron impact and photoionization detection schemes to investigate the photodissociation dynamics of two isomers of C_3H_4, allene (CH_2=C=CH_2) and propyne (CH_3–C≡CH). Radicals formed from these parent molecules play important roles in combustion, flames, and the interstellar medium.

The presence of inequivalent C–H bonds suggests that the loss of H or H_2 may produce isomeric photoproducts. Previous work has shown that the C_3H_3 radical produced by eliminating one H from allene is the propargyl (CH_2CCH) radical. For the dissociation of propyne, however, some dissent remains as to whether the primary H-elimination photoproduct is the propargyl radical or the propynyl (CH_3CC) radical. The propargyl radical would be produced by cleavage of one of propyne's three

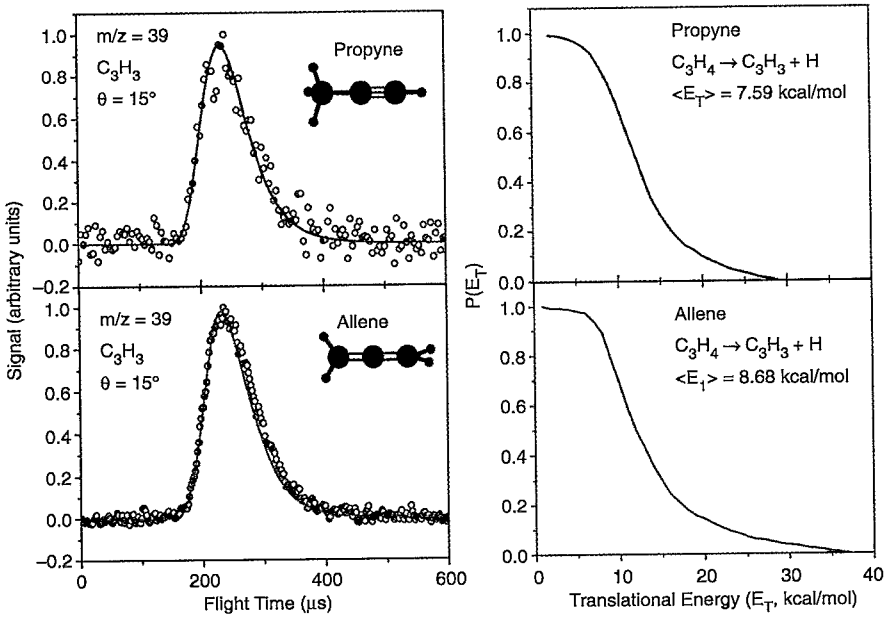

Figure 1

Time-of-flight (TOF) spectra for the m/z = 39 product (C_3H_3) from the 193-nm photodissociation of propyne and allene at 15° measured on the electron impact machine. Open circles represent the TOF data. Solid curves, representing the fit to the data, were obtained by forward convolution of the center-of-mass translational energy distributions shown at right. These probability distributions are too similar to distinguish between the isomers produced.

methyl C–H bonds (bond dissociation energy = 89 kcal/mol), while the propynyl radical would be produced by cleavage of the acetylenic C–H bond (130 kcal/mol).

Figure 1 shows the results for the H-loss channel obtained from a traditional electron-impact PTS machine with an ArF (193 nm, 148 kcal/mol) photolysis laser. Data were stored as angle-resolved velocity distributions in the laboratory frame of reference. Using forward convolution, we determined the center-of-mass translational energy distributions that best fit the data. Given the qualitative similarity of the translational energy distributions for propyne and allene dissociation products, one cannot distinguish between the isomers produced. Fortunately, the Advanced Light Source offers the possibility of photofragment discrimination based on ionization potential. The photoionization machine, located on the chemical dynamics beamline (Beamline 9.0.2.1), ionizes the photofragments with tunable vacuum ultraviolet (VUV) radiation (with photon energies ranging from 5 eV to 30 eV). The photoionization machine clears up the debate over the primary H-loss photoproducts, because the propargyl radical and the propynyl radical have significantly different ionization potentials (8.67 and 10.8 eV, respectively). Figure 2 shows the photoionization efficiency curves for the C_3H_3 product, confirming that the photolysis of allene yields the propargyl radical and indicating that photolysis of propyne produces the propynyl radical. Clearly, this is an excellent example of bond-selective chemistry, where the stronger acetylenic bond is broken preferentially over the weaker methyl bond. A 34-kcal/mol barrier prevents isomerization of propynyl radical to propargyl radical. As expected, the propynyl radical, which has at most 18 kcal/mol available energy in this experiment, does not rearrange to the propargyl radical.

For the H_2-loss channels, photodissociation of allene and propyne both yield the propadienylidene (CH_2CC) radical, as confirmed by photoionization efficiency experiments.

Overall, it is evident that coupling PTS with VUV ionization is a very powerful technique for the analysis

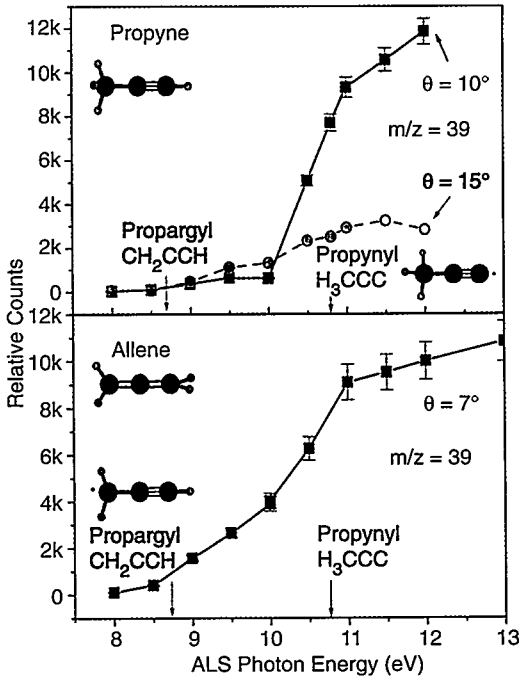

Figure 2

Photoionization efficiency curves for the C_3H_3 product. The ionization potential for the propargyl radical is shown in green, and that for the propynyl radical is shown in blue. The onset of ionization for allene occurs near the ionization potential for propargyl, as expected, whereas the ionization of propyne clearly begins at a higher energy.

of isomeric photoproducts. The current study shows that this technique allows one further step to be made away from the A + BC reaction scheme and toward a fuller understanding of complex chemical systems.

Investigators

W. Sun, K. Yokoyama, J.C. Robinson, D.M. Neumark (University of California, Berkeley, and Berkeley Lab) and A.G. Suits (Berkeley Lab).

Funding

U.S. Department of Energy, Office of Basic Energy Sciences.

Publications

1. W. Sun et al., J. Chem. Phys., in press.

Facility Report

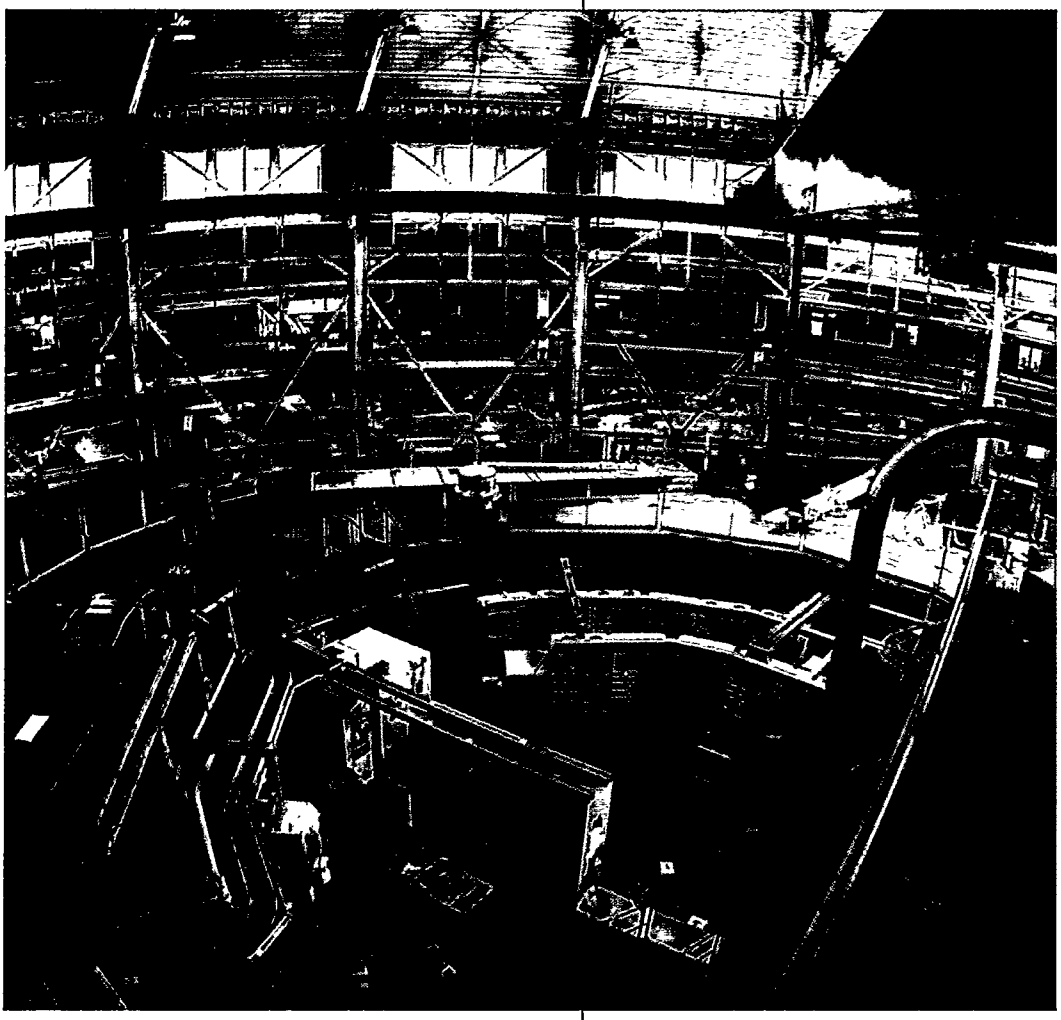

OPERATIONS

Bob Miller
Operations Group Leader

Reliable, efficient operation is the key prerequisite for a successful scientific program at a synchrotron light source. High-quality beams delivered according to a published schedule, along with an efficient, effective safety program are all required for researchers to make maximum use of their allocated beamtime. In 1997/98, the operations team once again maintained its exemplary record while making many improvements in beam quality. In addition, the ALS designed, constructed, and installed a new undulator for research on complex materials and atomic physics and began the installation of an elliptically polarizing undulator (EPU) and beamline designed to explore the spectroscopy of magnetic materials.

Reliability and Schedule

The research community at the ALS has become accustomed to reliable operation, and it was not disappointed during this period. As shown in Figure 1, the ALS delivered beam to the users 95% of the time scheduled for user operations in FY98, maintaining the reliability of the last several years.

In June 1998, the operations schedule was revised to provide more daytime, weekday beamtime for user operations. The maintenance and installation periods were reduced to one shutdown every two weeks, every other shutdown lasting two days. As a result, in one four-week period, two maintenance and installation shifts and two startup and tune shifts were converted into three user shifts and one accelerator physics shift. In addition, the accelerator physics shifts were rescheduled so that they begin after the day shift on every other Sunday. This allowed the percentage of weekday, daytime shifts dedicated to user operations to increase from 60% to 75%. A comparison of the new schedule to our previous schedule is shown in Figure 2 and Table 1.

This schedule is considered experimental, however, because it has a number of disadvantages compared to the previous schedule. Because user

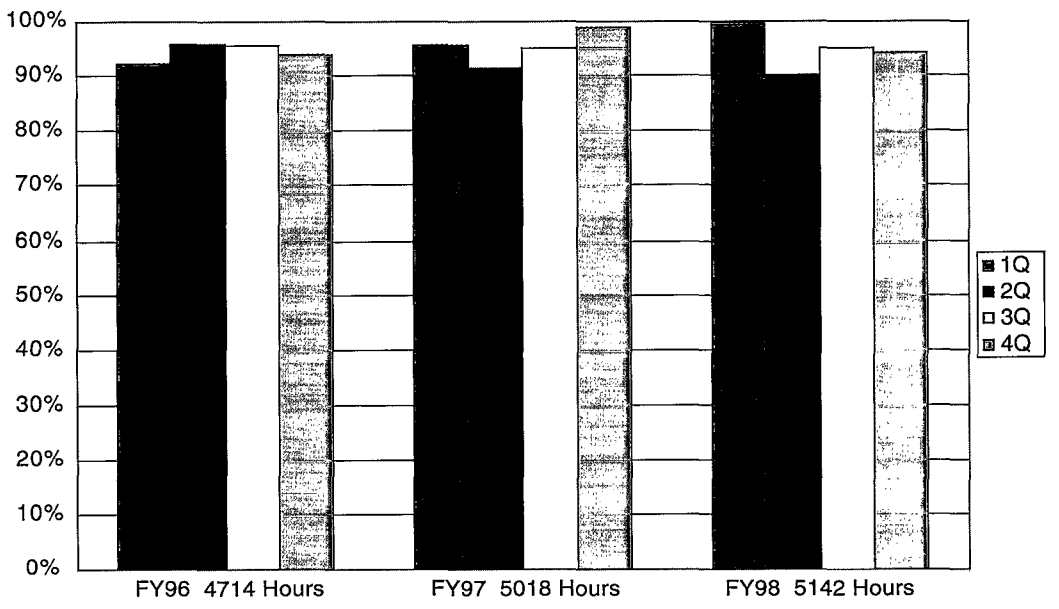

Figure 1
ALS operational efficiency (percentage of scheduled user beamtime actually delivered).

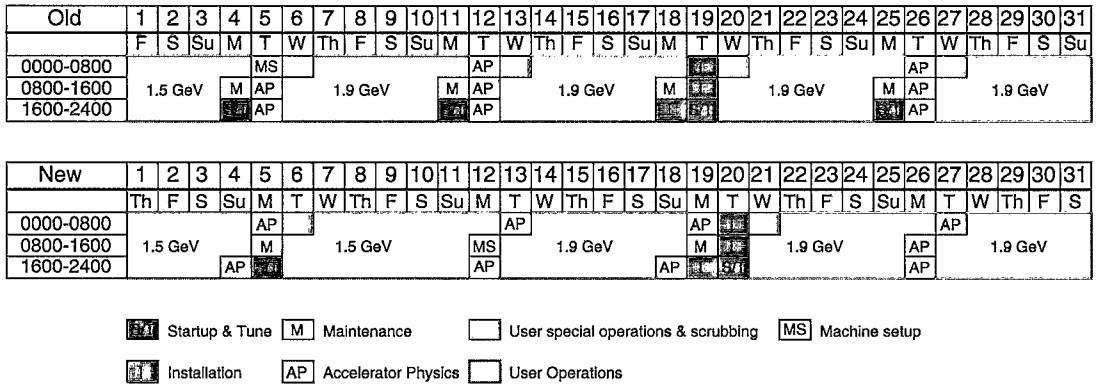

Figure 2

Comparison of the old shift schedule to the new, experimental shift schedule.

Table 1

Number of Shifts per Month for Accelerator Activities

PURPOSE	Number of Shifts OLD	NEW
User Operations	73	76
Accelerator Physics	8	9
Machine Setup	1	1
Maintenance & Installation	7	5
Startup & Tune	4	2
TOTAL	93	93

operations directly follow the maintenance and installation shutdowns, any problems resulting from changes made during the shutdowns would result in a loss of user beamtime, rather than accelerator physics beamtime. In addition, the reduced shutdown frequency means that the removal of failed components on beamlines will, in general, require an extra week, which could severely affect the users of that beamline. The operations schedule will be closely monitored and discussed with the Users' Executive Committee to arrive at an optimum algorithm.

Growth in User and Instrument Hours

We were able to slightly increase the number of operating hours from 5,018 in FY97 to 5,142 in FY98. Of the 5,142 hours scheduled, we delivered 4,864. In addition, we finished up the year with a total of 18 beamlines operating simultaneously, up from 12 at the end of the previous fiscal year. This increase in beamlines resulted in the delivery of 76,287 instrument hours (user hours multiplied by the number of simultaneous beamlines that can accept beam), an increase of 43% over FY97.

Figure 3 shows the number of user hours and instrument hours available from FY94 through FY98. The large increase in instrument hours in FY95 was due to the completion of the initial complement of ALS beamlines. In FY96, the increases in user hours and instrument hours were a

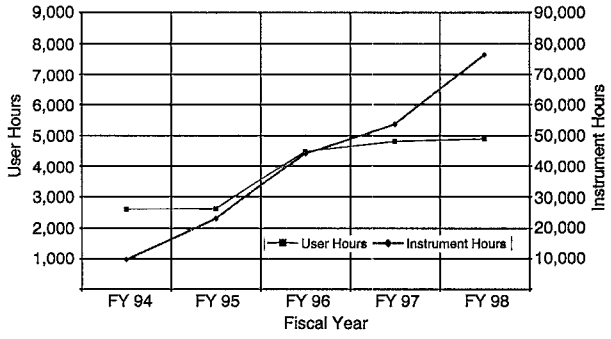

Figure 3

Number of user hours and instrument hours available from FY94 through FY98.

result of the additional operations funding of the Scientific Facilities Initiative (SFI). The SFI also enabled us to build new beamlines, and the installation of these beamlines resulted in the increase in instrument hours in FY98.

Facility Growth

Two shutdowns were scheduled during 1997/98 for the installation of new equipment. The first shutdown, in May 1997, was used to make two major changes in the storage ring. The vacuum chamber through the Sector 8 insertion device was modified to allow for a smaller gap. This enables the undulator to generate lower-energy photons at any particular electron-beam energy, thus minimizing the requests for operation at energies lower than 1.5 GeV. Because the overwhelming majority of ALS users prefer to have the storage ring operate at 1.9 GeV, reducing the need for low-energy operation benefits the overall user community. The second change during the spring 1997 shutdown was the installation of the vacuum chamber for the chicane in Sector 4. The chicane arrangement will allow two EPUs to be used simultaneously (Figure 4), providing the ALS with two bright insertion-device beamlines in one straight section. The EPUs will provide light of various polarizations, from linearly polarized (in the horizontal or vertical plane) to circularly polarized (left or right handed). Each of these devices (Figure 5) is half the length of our standard insertion device, so that two of them will fit into one straight section. In addition, the use of a shorter insertion device allows a C-shaped support structure to be used. This means that the undulators can be installed or moved during a short shutdown without breaking the storage-ring vacuum. Plans eventually call for three insertion devices to be installed in the Sector 4 straight section, two of them being able to operate simultaneously.

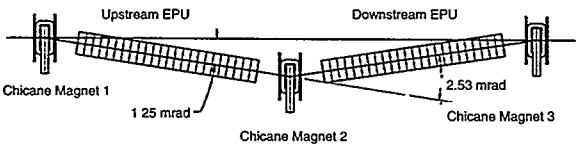

Figure 4

Chicane arrangement for the EPUs in the Sector 4 straight section.

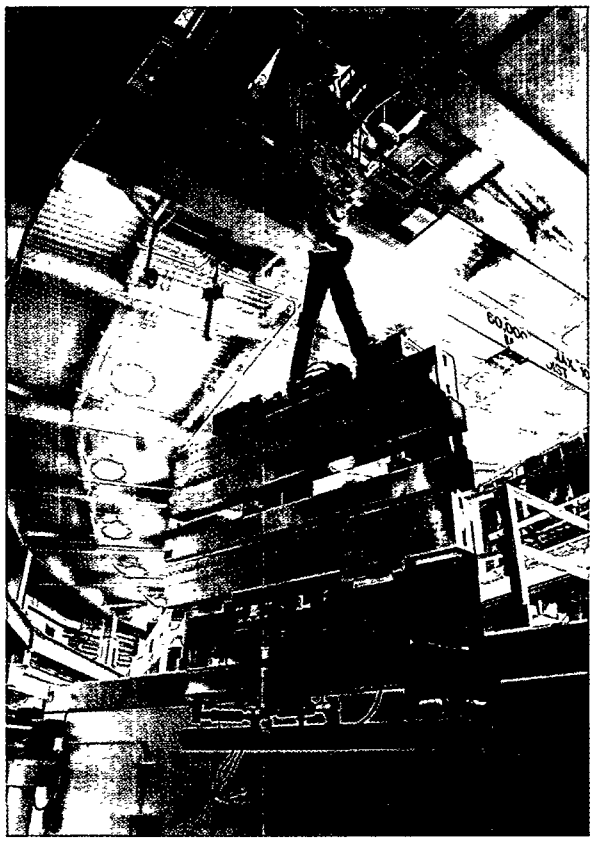

Figure 5

Elliptically polarizing undulator (EPU) hoisted for installation in Sector 4.

The second installation shutdown was scheduled in June 1998 to install the new undulator in Sector 10 (Figure 6). This project was another outgrowth of the SFI of FY96. A highly rated proposal by principal investigator Z.X. Shen of Stanford University was funded by the DOE to explore highly correlated materials, e.g., high-temperature superconductors. The program needed a new insertion-device beamline to maximize productivity. It was decided to build a new 10-cm-period undulator and to move

Figure 6

Installation of the Sector 10 undulator.

Beamline 9.0.1 to Sector 10 to accommodate this new program as well as the atomic physics program existing on Beamline 9.0.1. The undulator was partially built from parts purchased for the abandoned circularly polarizing wiggler (replaced by the EPU; see above). Moving Beamline 9.0.1, with its associated atomic physics program, enabled both the atomic physics program and the chemical dynamics program on Beamline 9.0.2 to increase their share of beamtime. Because the atomic physics program also received increased support from the SFI, the increase in beamtime has been extremely useful. The new beamline splits its time between the correlated materials program and the atomic physics program.

ACCELERATOR PHYSICS

Alan Jackson
Accelerator Physics Group Leader

For the majority of the ALS user community, 1997/98 could be characterized as a year of electron-beam stability. Our efforts from the previous year to master the intricacies of the transverse and longitudinal multibunch feedback systems, together with better control of the temperatures of the low-conductivity cooling water and storage-ring tunnel air, paid immense dividends in the stability of the beam during a fill. From this beginning, the Accelerator Physics Group embarked on achieving the next level of stability—improving the undulator feed-forward system that ensures that the electron beam remains stable as the undulator gaps are changed at the user's request, fine tuning the electron orbit for best transmission of the photon beams to the experiment stations, and ensuring that the beam comes back to the same place, fill after fill, day after day.

To a large extent, as we describe below under "Storage Ring Setup," this goal has been achieved. Since we do not have a stable platform at the micron level, however, we find it necessary to repeat our setup procedures at regular intervals—typically each week. Experimenters are certainly taking advantage of the enhanced stability by improving resolution and reducing sampling times. In doing so, they are discovering small (but, for some experiments, significant) photon beam motion in the frequency range between 1 kHz and 10 kHz. The Accelerator Physics Group is currently working with several user groups to identify and, we hope, eliminate the sources of this motion.

Advances have also been made toward delivering higher-quality beams for the single-bunch user community. During normal multibunch operation, we now offer a fill pattern known as the "camshaft fill." In this pattern, we fill 288 sequential rf buckets to about 1.3 mA/bunch (for a total of 380 mA), plus a single bunch at 20 mA that sits inside a string of 40 empty rf buckets. While this is useful for some experiments, we still operate in two-bunch mode for the traditional time-of-flight spectroscopy experiments. These users require that the unpopulated buckets be truly empty. This has been achieved at the ALS (as at other facilities) by taking advantage of the differences in the betatron oscillation frequency between bunches with different charge densities. Transverse kickers, driven at the discrete frequency of the low-charge bunches, drive out the unwanted electrons without affecting electrons in the two highly populated bunches. In this way, the bunch purity (the proportion of electrons in parasite bunches) has been improved from about 1:100 to better than 1:10,000. Also, the currents that can be accumulated in a single bunch, limited by the transverse mode-coupling instability, have been increased from around 20 mA to 35 mA by the use of active feedback.

In addition to the work aimed directly at improving the quality of beams for users, the Accelerator Physics Group has also started work on a series of new initiatives:

- Designing a third-harmonic cavity system to lengthen the electron bunches (without increasing the energy spread of the beam), which will result in longer beam lifetimes.
- Designing modifications to the ALS magnet lattice that will allow the insertion of superconducting bend magnets into the ALS to produce high-brightness, intermediate-energy x-ray beams.
- Developing methods for generating x rays in the 1-Å region of the spectrum with a pulse width of 100 fs FWHM.

Our group is also engaged in a series of investigations to better understand the performance characteristics of the storage ring. These include investigations of beam lifetime, fast beam motion, reduction of the horizontal and vertical emittance, vacuum-vessel impedance, the fast beam-ion instability, and other nonlinear beam dynamics in both transverse and longitudinal planes. These topics have been described in detail in the 1997 ALS Compendium of User Abstracts and Technical Reports.

ALS Storage-Ring Setup

The operational parameters of the ALS can be varied over a wide range to meet users' needs. The ALS storage ring is capable of operating from 0.75 GeV to 1.9 GeV with almost any fill pattern, utilizing from 1 to 328 rf buckets. The three most common modes of operation are 1.5-GeV multibunch, 1.9-GeV multibunch, and 1.9-GeV two-bunch (four weeks per year). The multibunch pattern typically consists of 288 contiguous bunches with a gap for ion clearing. Often one of the empty rf buckets can be filled to high current to create pseudo–one-bunch operation (camshaft mode). Substantial progress was made in 1997 toward automating the setup; however, it is still a very machine-time-intensive activity. A full machine setup takes approximately eight hours, which is roughly one-third of the time allotted for accelerator physics studies.

General Storage-Ring Setup

Many parameters have to be properly set in order for the storage ring to operate as designed. The storage-ring magnet lattice consists of 36 bends, 48 sextupoles, 72 quadrupoles, 4 skew quadrupoles, 94 horizontal correctors, and 70 vertical correctors. The other major systems include the rf system, the longitudinal-feedback system, and the transverse-feedback system. The main beam diagnostics consist of 96 arc-sector beam-position monitors (BPMs), 20 straight-section BPMs, the tune-measurement system, and the transverse and longitudinal beam-profile monitors (Beamline 3.1). To a large extent, the setup and operation of the ALS storage ring have been automated. The setup process consists of accurately setting the parameters in the sequence shown in Figure 1. Some steps in the process require iteration.

Special attention was given to the orbit in 1997. A particular orbit, known as the "golden orbit," was defined and then maintained all year. The procedure for defining the golden orbit is as follows: First, the orbit is aligned to the center of the horizontally focusing and defocusing (QF and QD) quadrupole magnet families. This minimizes the dispersion caused by going off center in these magnets. Using the electron beam, the quadrupole centers can be measured to the 50-μm level. Second, in order to steer the photon beams down the beamlines, local orbit perturbations (typically displacements of about 100 μm and angles of 30 μrad) are added to the ideal orbit. Finally, in the straight sections with small-gap vacuum chambers, the optimal orbit is the position that produces the maximum lifetime. Correcting back to the golden orbit at every setup has essentially eliminated user requests for local orbit correction.

A simple local-steering feed-forward algorithm to compensate for field errors that change as the insertion device gaps are moved has proven to be extremely effective. The rms orbit distortion due to gap changes after generating a feed-forward table is typically less than 10 μm. The difficulty with this method is that the feed-forward tables are strongly orbit dependent, so they need to be regenerated at every setup. Since each table takes about 15 minutes to generate, we are considering replacing this compensation method with one that relies on real-time closed-orbit feedback.

The setup and operation of the ALS storage ring are done with Matlab, a matrix-manipulation

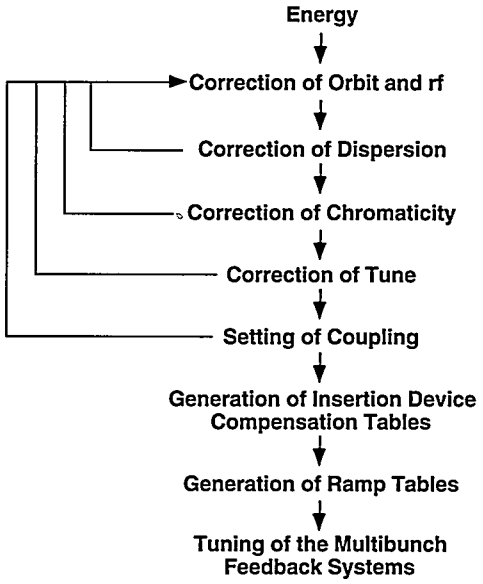

Figure 1

Storage-ring setup process.

language. By connecting Matlab to the ALS control system, the large number of built-in functions for numerical methods in Matlab immediately become available for accelerator optimization. Automating the operation of the storage ring using this one application has improved orbit repeatability considerably by allowing us to maintain tight control of the many potential sources of error, such as magnet hysteresis. This has also reduced the time it takes to refill the storage ring and has removed some of the human errors that occasionally creep into day-to-day operation.

Two-Bunch Setup

Some synchrotron light users require single pulses of light spaced by at least several hundred nanoseconds. To satisfy this community, the ALS operates in a two-bunch mode for about four weeks each year. In this mode, the ALS storage ring is filled with two bunches, diametrically opposite in the ring, with 328-ns separation. It is also important to the experiments that there be no parasite bunches in the ring. To optimize the machine performance, we are faced with the challenges of reaching high single-bunch current with a reasonable lifetime while maintaining the purity of the two-bunch fill.

One limit to high current is a single-bunch effect known as the vertical mode-coupling instability (VMCI), driven by the broadband transverse impedance of the vacuum chamber. The effect is characterized by a sudden increase in vertical oscillations, resulting in a large increase in the effective vertical beam size and a corresponding decrease in the brightness and stability of the beam. For the ALS, the threshold of this instability is currently about 16 mA/bunch. To achieve higher currents, we can damp the instability by increasing the lattice chromaticity (variation of betatron tune with electron momentum) from around 0.5 to 5.0. However, the higher chromaticity lowers the energy acceptance, thereby increasing the loss of electrons from Touschek scattering (large-angle intrabeam scattering) and lowering the lifetime. To avoid a lower lifetime, we have configured the vertical coupled-bunch feedback system to operate in single-bunch mode and tuned it to successfully reach greater than

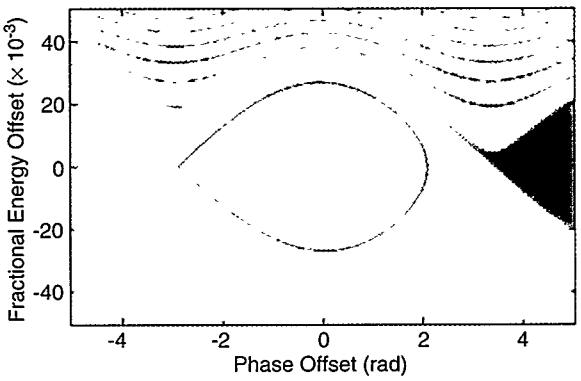

Figure 2

Bunch-to-bunch diffusion can occur with radiation damping, as shown in this particle tracking diagram. Ordinarily, only the central dark-green region would be stable; electrons scattered out of it would be lost. With radiation damping, such electrons can be captured by the tail of the next bunch (brown, right side), where they are trapped in stable synchrotron orbits.

30 mA/bunch, double the current of the high-chromaticity approach.

The second challenge in two-bunch operation is to achieve high bunch purity. The dominant mechanism through which parasite bunches are filled operates during the injection process. Imperfect bunching of the electron beam in the linac gun leads to a parasite bunch 8 ns from the main bunch with a charge as high as 1% of the main bunch. A more subtle mechanism, bunch-to-bunch diffusion, also comes into play (see the description in Figure 2). Rather than minimize the parasite filling during injection (which requires lowering the overall injection rate), we have developed a technique for cleaning out the parasite bunches immediately after injection. This technique takes advantage of the current-dependent vertical betatron frequency shift due to the transverse broadband impedance. At around 20 mA/bunch, the vertical betatron frequency has shifted about 15 kHz from the nominal frequency. This provides a selection mechanism for exciting only the low-current parasite bunches. We excite oscillations of the parasite bunches, utilizing the vertical kickers of the multibunch feedback system, to an amplitude large enough for them to be removed by a vertical scraper. Using this technique, we have reached purities of 1:10,000 and better.

New Initiatives

The ALS Third-Harmonic Cavity Project

The ALS beam lifetime is dominated by Touschek scattering. Electrons scattering off one another within a bunch have some probability of being scattered outside the machine momentum acceptance. The loss rate is proportional to the integrated charge density squared, and the lifetime depends approximately on the cube of the beam energy. This dependence on energy explains why the ALS loss rate is lower for 1.9-GeV operation compared to 1.5-GeV operation. Lengthening the electron bunch will reduce the charge density and increase the beam lifetime. The addition of a third-harmonic cavity system will increase the beam lifetime by controlling the longitudinal bunch shape.

With a single rf system, a quasi-harmonic potential well is formed. The quantum excitation from the emission of synchrotron radiation photons produces a Gaussian energy spread. This, in combination with the rf voltage, results in a Gaussian longitudinal charge distribution. To modify the distribution, a harmonic rf voltage with a frequency that is an integral multiple of the main rf frequency can cancel the slope of the main rf voltage at the bunch center. The optimum voltage to lengthen the bunch is $\sim V_{rf}/n$. A harmonic number of three was chosen for the ALS. The resulting total rf voltage is shown in Figure 3.

The use of the third-harmonic cavity will change the bunch potential from a quadratic form to a quartic, resulting in a non-Gaussian longitudinal distribution. This longitudinal distribution of the bunch density is shown in Figure 4. Initially, we plan to use the cavity in a passive mode. The cavity frequency is tuned slightly above the third harmonic to excite the appropriate voltage for bunch lengthening. The tuner is adjusted to maintain a constant cavity voltage. As can be seen in Figure 5, the optimum tuning position for improving the beam lifetime depends on the beam current. With a passive cavity, the lifetime will be fully optimized at only one beam current, and the longitudinal beam profile will change as the current changes. It is expected that the lifetime for 1.9-GeV operation will increase by a factor of about three when the cavity is installed.

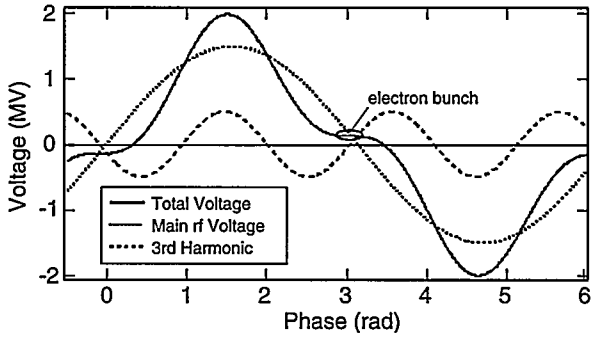

Figure 3

Effect of adding a third-harmonic rf voltage to the main rf voltage. For maximum bunch lengthening, the harmonic voltage should cancel the slope of the main rf voltage at the bunch center. Optimum voltage is $\sim V_{rf}/n$.

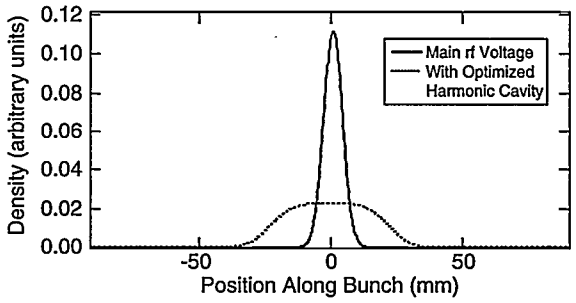

Figure 4

Non-Gaussian longitudinal distribution of the bunch density after addition of the third-harmonic cavity.

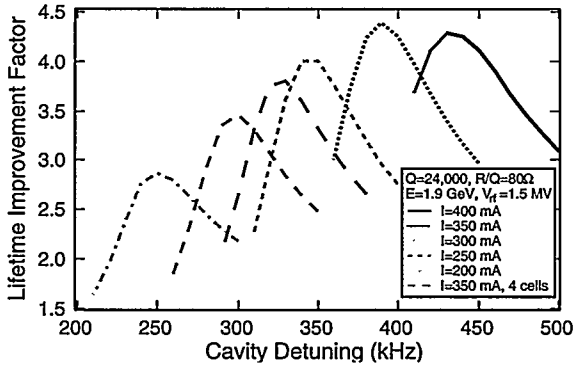

Figure 5

The optimum tuning position is found by plotting improvement in lifetime vs. resonant frequency for several beam currents.

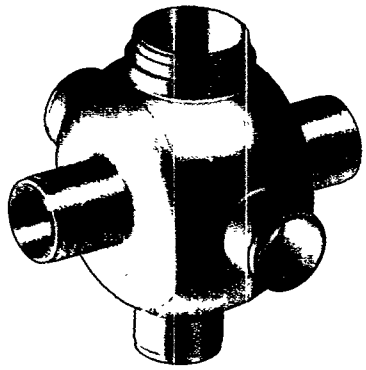

Figure 6

Third-harmonic cavity design: the bottom port is used for the main tuner, one side port for the secondary tuner, the other side port for the rf probe, and the input port is capped with an arc detector.

This project, led by Accelerator Physics Group member John Byrd, will actually involve installation of five 1.5-GHz copper cavities in the second half of the Sector 2 straight section, leaving space for a sixth cavity if needed. The cavities have been designed by the Beam Electrodynamics Group of the Center for Beam Physics in the Accelerator and Fusion Research Division (AFRD) and are being constructed at Lawrence Livermore National Laboratory by the same team that built the cavities for the B-Factory. The cavity design is shown in Figure 6. As mentioned above, the cavities will operate in a passive mode with their voltage excited by the beam and adjusted by tuning the cavity frequency. This mode of operation will allow for the "parking" of the cavities (tuning them off resonance so that they do not influence the beam) in case of problems. A support structure has been designed so that the cavities can be installed together on the existing support rails. Installation of the cavities is scheduled for June 1999.

Superbend Magnet Project

The ALS has found that the regional community is looking for a source of high-brightness x rays of higher energy than that provided by the existing bend magnets and undulators. To satisfy this demand without using up valuable straight-section real estate (i.e., building new wigglers), the ALS is planning to replace normal-conducting dipoles with superconducting dipoles. This will allow the ALS to provide a high-brightness source of intermediate-energy x rays from 10 keV to 25 keV. Figure 7 compares the fluxes and brightnesses of ALS bend magnets, the proposed superbend magnets, and a number of other sources.

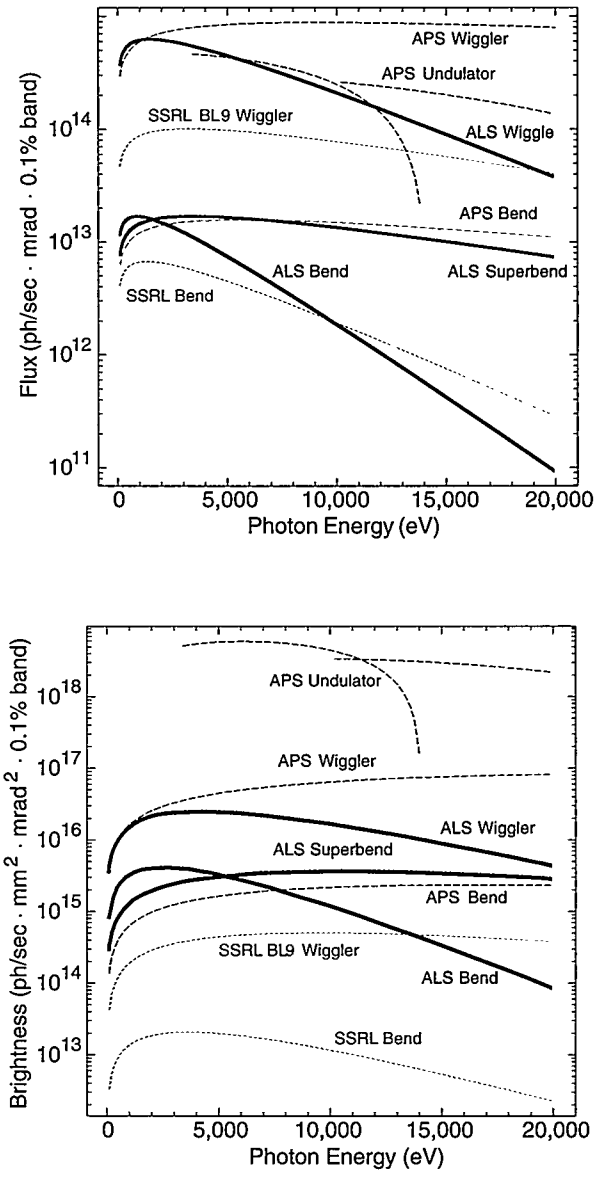

Figure 7

Flux and brightness comparisons: ALS bend and superbend magnets and wiggler, Advanced Photon Source (APS) sources, and Stanford Synchrotron Radiation Laboratory (SSRL) sources.

To produce the required high-brightness, higher-energy x rays, two conditions must be satisfied.

- For high-energy x rays, it is necessary to increase the dipole field. Increasing the field from 1.3 T to 5.0 T will increase the critical energy of the x rays from 3.1 keV to 12.0 keV.
- For high brightness, the beam size must be small at the dipole location. This is true at the location of the center bend magnet in each of the ALS sectors.

The plan is to replace the combined-function conventional dipole magnet in the center of three of the twelve ALS sectors with a 5-T superconducting dipole magnet and a pair of conventional quadrupoles. The three sectors will be chosen so that the dynamic aperture of the ALS, which depends upon the symmetry of the magnet lattice, remains large enough for efficient beam injection.

This project is based upon the successful completion of the Laboratory Directed Research and Development project to produce a superconducting bend magnet, which lasted from 1995 to 1998. That project, undertaken by the ALS Accelerator Physics Group in collaboration with the AFRD Superconducting Magnet Program and Wang NMR, has resulted in the production of a robust superconducting coil design using commercial magnetic resonance imaging technology.

This project has been endorsed by the ALS Science Policy Board, the ALS Workshop on Scientific Directions, and the ALS Scientific Advisory Committee. The goal is to install the superbend magnets in the first half of 2001.

Workshop on the Uses and Generation of Femtosecond Radiation

The goal of this workshop, held at Berkeley Lab in February 1998, was to develop a set of parameters for a femtosecond source that would be useful for specific experiments and to describe to the user community the different techniques that might eventually be used to meet their requirements. The workshop was indeed informative and very useful. Certainly, the cross-discipline interactions were very successful. However, it became clear during the discussion period that the experimenters present had not thought much beyond the extremely demanding experiments that they are doing right now, and we did not come away from the workshop with the hoped-for set of parameters that would be the basis for a new source. The workshop did, however, spur a number of investigators to think further about what they would need to push forward with their experiments. The types of experiments and the parameters required are as follows:

- Order–disorder transitions in ordered solids, e.g., silicon melting (using Bragg diffraction).
- Order–disorder transitions in amorphous materials, e.g., the molten carbon insulator–metal transition (using EXAFS).
- Chemical dynamics at surfaces or in solution, e.g., in laser desorption of CO from metal surfaces (using EXAFS).
- Protein–chromophore dynamics, e.g., bacteriorhodopsin isomerization (using diffraction).

The photon parameters required for these experiments are typically as follows:

- Energy: 1–20 keV
- Bandwidth: 10^{-3}
- Pulse width: <100 fs
- Flux: $>10^4$ photons/pulse
- Repetition rate: ~100 kHz
- Sample size: 100 μm
- Angle subtended: <1 mrad
- Synchronization: to within 100 fs

Some novel source concepts, involving both linac- and ring-based systems, also evolved during and immediately after the workshop. These will be pursued in the coming year.

EXPERIMENTAL SYSTEMS

H.A. Padmore
Experimental Systems Group Leader

The Experimental Systems Group (ESG) has two main functions. First, it designs and constructs beamlines and endstations in response to specific needs of the user community. Second, it engages in scientific outreach, developing the techniques of synchrotron radiation research and introducing them to new user communities. The latter involves identifying and working with potential new user groups to demonstrate an application of a synchrotron radiation technique, developing the technique where appropriate, and assisting in the production of proposals to funding agencies. If successful, the work continues on to the construction phase. Upon completion of construction, ESG continues to work with the group, again developing new experimental techniques where required. In this way, we can lower the "technological potential barrier" to new groups becoming involved with the ALS. This is particularly true in the area of microscopy, where often the instrumentation is complex and, without actively fostering new user groups, the barriers to trying a technique and building a program might be too high. We have had a number of successes in this area during the past year, and in this section I will give a few highlights of the work carried out by the group.

Beamline 7.3.1.1: Photoemission Electron Microscopy for Magnetic Materials

A new photoemission electron microscope, PEEM2, has been designed, built, and installed at Beamline 7.3.1.1. The microscope was funded by a Cooperative Research and Development Agreement (CRADA) between DOE and IBM. The ALS team is led by Simone Anders as part of a collaboration with Joachim Stöhr at IBM Almaden and Michael Scheinfein at Arizona State University. The main applications of the instrument are the study of magnetic materials and multilayer structures of interest to IBM, such as spin valves, magnetic storage media, and magnetic RAM, and basic research in magnetic materials. PEEM2 will be available 50% of the time for independent investigators. Outside user applications will include the study of polymers, aspects of the tribology of magnetic storage media, geological studies, and many other areas.

Beamline 7.3.1.1 is a bending-magnet beamline specifically designed for spectromicroscopy of magnetic materials with PEEM. The beamline is designed to produce the highest possible flux density in the illuminated field of the microscope. It is equipped with an entrance-slitless, vertically focusing, spherical-grating monochromator, covering the energy range from 180 to 1300 eV. A 1-m-long elliptical mirror focuses 2 mrad of light horizontally to

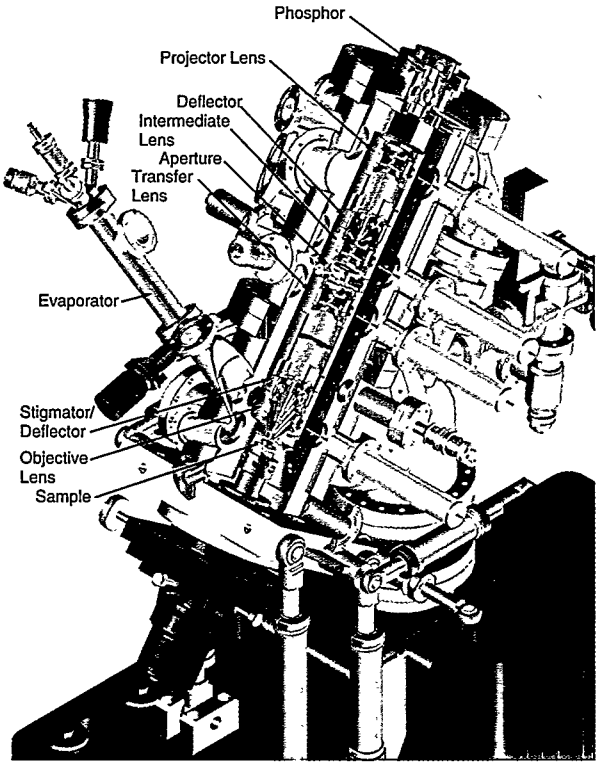

Figure 1
Layout of the PEEM2 photoemission electron microscope.

30 mm with a photon flux of 3×10^{12} photons/s in a field size of 30 μm. As the system is used without exit slits, the field size sets the energy resolution, and over a field of 30 μm, a monoenergetic beam with a resolving power of 1800 is defined. A mask and a chopper allow selection of light above, below, or in the orbit plane of the storage ring so that left or right circularly polarized radiation as well as in-plane linearly polarized radiation can be selected.

The PEEM2 microscope is a four-lens, electrostatic system equipped with a stigmator and two deflectors to correct for misalignment and machining errors in the lenses (Figure 1). A flexure stage provides a mechanism to exchange apertures easily. Four apertures are available (with 2-mm, 12-mm, 20-mm, and 50-mm diameters). The aperture selected determines the spatial resolution and throughput of the microscope. The detector uses a phosphor on a fiber-optic plate, which is directly coupled to a slow-scan CCD camera. The fastest image acquisition speed is 4 images per second, which is sufficient for fast focusing when the camera is in "binning" mode (i.e., when grouping pixels for faster readout). The sample stage contains a heater that can bring sample temperatures up to 1200°C and accommodates samples of arbitrary size with an accessible area of 1 cm^2. PEEM2 is also equipped with an ultraviolet lamp, so all possible contrast mechanisms (topology, work function, element, chemical state, magnetic circular and linear dichroism, and bonding orientation) are available.

PEEM2 is equipped with a sample preparation chamber and automated sample transfer. The sample transfer system includes a fast load lock and a three-sample parking stage for fast sample exchange. The sample preparation chamber is equipped with four evaporators and a movable sample stage and shutter to allow the growth of wedge structures. The sample stage for the preparation chamber incorporates the same heater used by the microscope sample stage. The preparation chamber is equipped with a sputtering gun for sample cleaning, a low-energy electron diffraction system for sample analysis, and a magnet to magnetize and demagnetize samples. The microscope sample stage is retractable so that the x rays can be directed into a chamber downstream of the microscope. This chamber is equipped with near-edge x-ray absorption fine structure (NEXAFS) spectroscopy and x-ray magnetic circular dichroism (XMCD) spectroscopy setups for taking reference spectra to compare with micro-scale XMCD data and for conducting more general XMCD spectroscopy.

The microscope has been tested with ultraviolet and x-ray radiation. Figure 2 shows 18-μm cobalt squares on silicon for the testing of XMCD contrast. The magnetic domains and the reversal of contrast are clearly visible. The resolution obtained thus far is 35 nm, although we expect to get still closer to the design resolution of 20 nm with more precise alignment.

In parallel with the work on PEEM2, work is proceeding on the design and construction of an

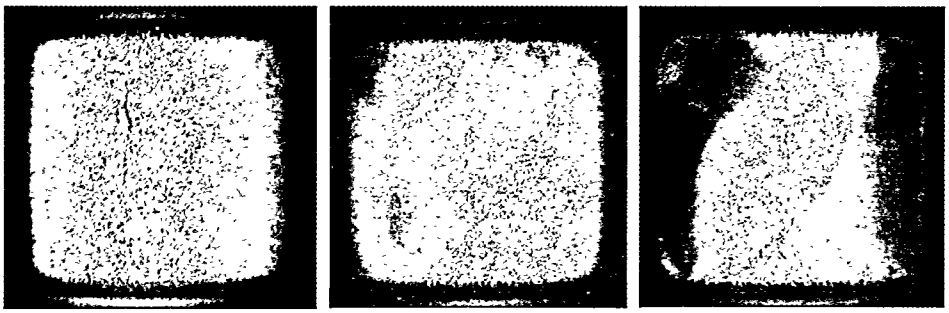

Figure 2

PEEM images of 18-μm cobalt squares on silicon, imaged with (a) radiation above the cobalt L_3 absorption edge and (b) left and (c) right circularly polarized light at the cobalt L_3 absorption edge.

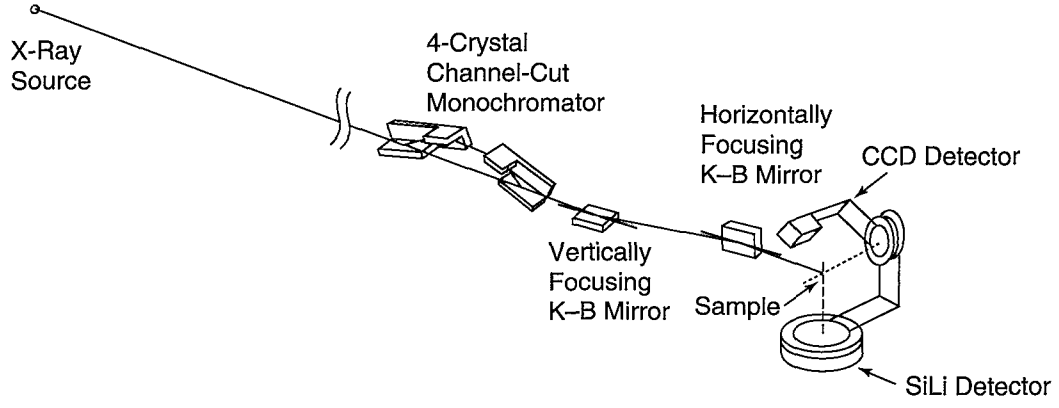

Figure 3

Layout of Beamline 10.3.2.

aberration-corrected microscope. The correction scheme corrects for the intrinsic spherical and chromatic aberration of the transmission lenses by using an electron mirror. This work has been funded so far by Berkeley Lab Laboratory Directed Research and Development (LDRD) funds and is expected to yield a microscope with greater transmission that is capable of 2-nm resolution.

Beamline 10.3.2: From Microdiffraction to Microfocused X-Ray Absorption Spectroscopy

In order to demonstrate the feasibility of x-ray diffraction for strain measurement in thin films at a spatial resolution of 1 μm, a group led by Alastair MacDowell constructed a microfocus system in the Beamline 10.3.2 hutch. This work was originally funded by an LDRD grant and is now attracting support from Intel Corporation for its application to the study of electromigration. The beamline optics consist of a four-crystal monochromator followed by a Kirkpatrick–Baez mirror pair (Figure 3). The sample area is configured with a sample scanning stage, a simple goniometer, and an x-ray CCD camera.

The four-crystal monochromator has the unique property that, when it is rotated to zero angle, the white beam can pass straight through, along the same line as the monochromatic light that would be generated by rotating the crystals to intercept the beam. The white or monochromatic light is then focused by a pair of elliptically bent mirrors with a demagnification of 300:1 in the vertical direction and 60:1 in the horizontal direction. The beam size in an ALS center bend magnet at 1.9 GeV is 20 μm (vertically) by 240 μm (horizontally), so the image size should be 0.33 μm by 0.8 μm. In fact, we measure a beam size of 0.8 μm in both planes, presumably because of an excessive tangential slope error in the vertical direction. The use of white light is crucial for diffraction experiments, as it allows us to find the orientation of an individual microcrystal from the Laue diffraction pattern without moving the sample, unlike in conventional rotation crystallography. Once the orientation is known and the Laue pattern indexed, measuring strain only requires knowledge of the exact photon energies of six independent reflections, and this can be gained with the four-crystal monochromator. Based on initial results with this apparatus, a dedicated system for microdiffraction has been designed and is in the process of being set up on Beamline 7.3.3.

The microfocusing optics and four-crystal monochromator can also be used for microfocused x-ray absorption spectroscopy (μ-XAS), and a program in earth and environmental science is now under way on Beamline 10.3.2. It is led by Geraldine Lamble of the Earth Sciences Division. Although the resolution is not as high as some of the soft x-ray microscopes at the ALS, other features of the system make it particularly useful for earth science. The main features of the system are that the sample can be in air, it can be

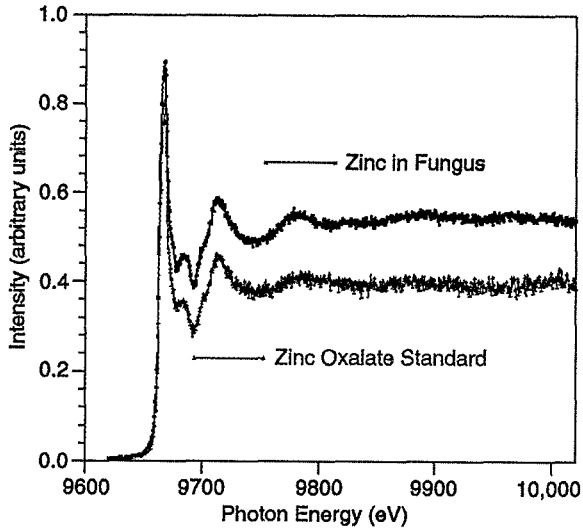

Figure 4

X-ray absorption spectrum of zinc in a fungus, taken at a spatial resolution of 0.8 μm. By comparing to spectra for model compounds, the compound in the fungus was identified as zinc oxalate.

wet, and fluorescence detection can be employed for detecting trace elements. The sample is first optically registered with the x-ray beam, and then white or monochromatic light is used to scan for elements of interest. Once the area of interest is located, the monochromator is tuned to a specific elemental edge, and the fluorescence signal is recorded as a function of photon energy through the absorption edge. As an example, Figure 4 shows data taken from a 0.8-μm area of a hyperaccumulating zinc fungus. By comparing spectra to those from model compounds, the compound in question was identified as zinc oxalate.

This system has now been used by a wide range of groups, and it is clear that the use of such microfocused beams for spectroscopy will have a significant impact in environmental and earth sciences. The present system was designed for high spatial resolution, however, and many experiments could clearly be conducted with beams as large as 10 μm. A system optimized for this resolution would give approximately 100 times the signal we now have. We have designed a system that will allow such a flux/resolution tradeoff. The key difference between it and the existing system is that a 1:1-focusing relay mirror (sagittally focusing in the vertical direction) will relay light to a pair of slits, and the Kirkpatrick–Baez mirror system will refocus the beam from these slits to the sample. By opening or closing the slits, one can increase or decrease the focused spot size with a commensurate change in intensity. A similar system has been implemented on Beamline 7.3.3.

Beamline 7.3.3: The Future of X-Ray Diffraction

The diffraction work on Beamline 7.3.3. is led by Alastair MacDowell and Richard Celestre. The purpose of this work is twofold: to develop the techniques and applications of microdiffraction and to develop and extend the use of x-ray diffraction to new areas. Two examples of this work are given below. In the next year, this work will be extended with installation of a dedicated microdiffraction system similar to that prototyped on Beamline 10.3.2. With that prototype, we demonstrated single-crystal diffraction at submicron spatial resolution on aluminum–copper thin films. The new, state-of-the-art facility will include a sophisticated diffractometer and CCD camera system made available by funding from Intel Corporation.

The explosive growth of synchrotron-based protein crystallography has been fueled by the rapid growth of structural biology. The ability to rapidly determine and manipulate protein sequences has led to a similar need to rapidly determine the folded structure of proteins. We are investigating ways in which some of the most challenging problems can be attacked by using optimized x-ray optics while minimizing the cost of the overall system. The aim of this work is to devise systems that can be quickly and inexpensively replicated to satisfy this ever-increasing need.

One of the most challenging problems is the solution of the structure of microcrystals. In a collaboration with Robert Glaeser (UC Berkeley) and Peter Wailian (Berkeley Lab), we have built a focusing system optimized for microcrystals with a moderate unit-cell size (e.g., 100 Å).

Beamline 7.3.3 consists of a 1:1-focusing toroidal mirror that directs light to the entrance of a large hutch. The optical arrangement inside the hutch sits on an optical table for flexibility and can easily be reconfigured. In tests with cryofrozen crystals, we refocused the 240-μm (horizontal) by 120-μm (vertical) image to 240 μm by 35 μm with a 1:1 horizontally focusing, multilayer monochromator and a 4:1-demagnifying, grazing-incidence mirror. The light was collimated by a slit in the horizontal direction, and data were collected with an Area Detector Systems Corporation 2 × 2 CCD x-ray detector. The detector was borrowed from the Macromolecular Crystallography Facility (MCF), and we are grateful to Carl Cork and other MCF staff for their assistance with the data acquisition system. The optical system we used optimizes both the vertical focusing of light onto the crystal and the bandpass required. In this case, the divergence from the source was around 3 mrad (horizontal) by 0.2 mrad (vertical). This means that, if needed, the light could be demagnified in the vertical direction by a factor of 15 without degrading the diffraction pattern resolution. In the case of the ALS, this means that all of the light can be collected in the vertical direction and focused onto the smallest of microcrystals without loss. The wavelength resolution is determined by the unit-cell size and the diffraction order required to record the diffraction pattern at the required resolution. In the case of a 100-Å unit cell recorded to 2-Å resolution, the fractional wavelength resolution should therefore be 2/100. We used a multilayer mirror with a 1/230 bandpass and a peak reflectivity of 40%. This multilayer was bent to a cylindrical shape, and the back face was cooled by using a liquid–metal interface.

Figure 5 shows a diffraction pattern from a microcrystal (approximately 80 μm × 60 μm × 5 μm) of a membrane protein, bacteriorhodopsin. The pattern was recorded over one degree of rotation, and data were accumulated for 100 s. The intensity was around 8×10^6 photons/s·μm^2, and diffraction to 2 Å can be seen. Thus, even with a low-power bending magnet, useful data can be collected on challenging systems. With further optimization, a factor-of-10 increase in intensity could be expected. This sort of technology by itself offers tremendous potential for high-performance, bending-magnet protein crystallography beamlines, but combined with the high intensity of superbend beamlines, it will offer outstanding performance.

All of these performance values need to be assessed in light of the fundamental limits set by primary radiation damage. Our cryofrozen crystals started to show deterioration after an exposure of 10 frames (10° of rotation, in this case). A higher dose rate would shorten the overall duration of data collection, but as several crystals would be needed for a complete data set, increasing the flux further would not linearly reduce the total time because of the large amount of time required for mounting and aligning the microcrystals. The higher flux afforded by superbends will therefore become particularly useful for multiple-wavelength anomalous diffraction (MAD) studies of microcrystals and for large-unit-cell crystals where higher angular collimation is required.

The beamline has also been used for powder diffraction. Working with the UC Berkeley research group of Paul Alivisatos, we have been investigating

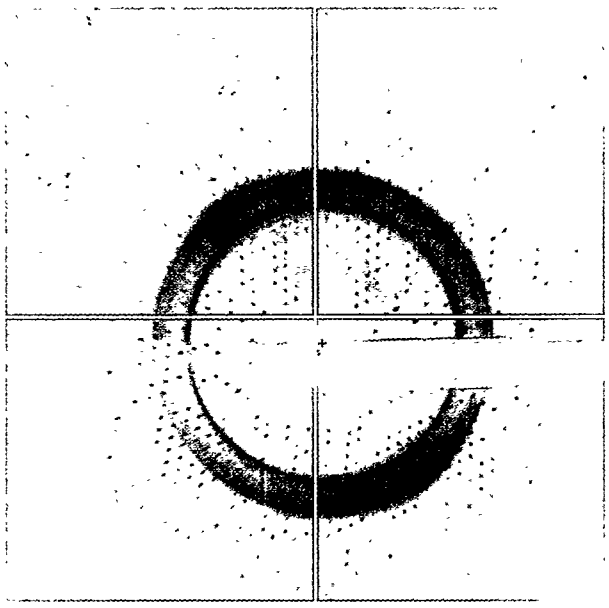

Figure 5

Diffraction pattern of bacteriorhodopsin recorded with a microfocused, wide-bandpass beam.

the use of bending-magnet beamlines for powder diffraction from semiconductor nanocrystals at high pressure. The pattern shown in Figure 6 is from 50-Å CdSe nanocrystals in a high-pressure diamond anvil cell. It was recorded in 100 s with a germanium (111) monochromator operating at 12.6 keV. The background is exceptionally low because of good collimation and shielding. The exposure, though short already, can be reduced substantially by increasing the bandwidth of the light, using a multilayer monochromator rather than a crystal monochromator. As the nanocrystals only have a few unit cells per particle, both angular and wavelength resolution can be relaxed without affecting the intrinsic resolution of the powder pattern. Using a 1/230-bandpass curved-crystal monochromator, we have demonstrated fluxes a factor of 10 higher in intensity than those with the germanium (111) monochromator, and this will translate into very short data acquisition times. This opens up the possibility of dynamic experiments, for example, where pressure is cycled to map out the lattice-spacing hysteresis loop. This work is being extended to look at the possibility of using a diamond anvil cell with a transverse geometry and a low-Z gasket. This would enable us to study high-pressure reactions with a vertically microfocused beam while monitoring chemical state with a scanning or dispersive monochromator.

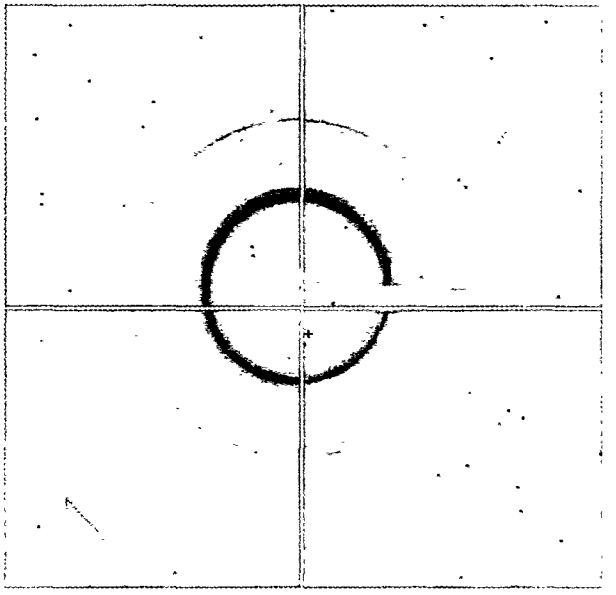

Figure 6

Powder diffraction pattern of 50-Å CdSe nanocrystals in a diamond anvil cell.

SCIENTIFIC SUPPORT

Zahid Hussain

Scientific Support Group Leader

The Scientific Support Group (SSG) is headed by Zahid Hussain, with John Bozek as Deputy, and consists of a team of scientists, postdoctoral fellows, students, and associate beamline scientists. The SSG has the following mission:

- Provide scientific and technical support to users for carrying out their experiments independently or in collaboration.
- Work toward making beamlines and endstations more user friendly, effective, and efficient.
- Develop technical specifications for the beamlines and have beamline data sheets and beamline manuals available.
- Provide access to state-of-the-art and user-friendly data analysis tools, a "seamless computing environment," for analysis of experimental data.
- Assist users in developing novel or better experimental equipment and provide technical help in putting together proposals for new funding.
- Develop communications with users to involve them in building and improving the scientific program and maintaining the ALS's status as a world-class user facility.
- Perform outreach to broaden the ALS user base.

Following are brief descriptions of some of the projects in which SSG members helped provide the scientific vision for the development of novel beamline or endstation instrumentation. These grew out of two projects supported by the Department of Energy's FY96 Scientific Facilities Initiative (SFI). The projects necessitated the creation of a new beamline at the ALS with high spectral resolution in the 20- to 350-eV photon energy range. Programs in highly correlated electron systems and atomic and molecular physics, led by Professor Z.X. Shen of Stanford University and Professor Nora Berrah of Western Michigan University, respectively, required the high resolution and high flux that an undulator beamline at the ALS can provide. Construction of the new beamline was carried out by members of many different groups at the ALS and overseen by members of the SSG. SSG members also participated in the design, fabrication, commissioning, and operation of the new endstations.

The New Beamline

Beamline 10.0.1 was built from many existing components. The spherical-grating monochromator (SGM) from Beamline 9.0.1, which had shared access to undulator radiation with Beamline 9.0.2, was moved to become the heart of the new system. New vacuum components and optics were constructed as required to replace parts left in the shared regions of the previous beamline. A new 4.5-m-long, 10-cm-period undulator was constructed from many existing parts. Magnets, a support and drive system, and even a vacuum tank were salvaged from other projects and used in the construction of the undulator. Performance was not compromised in this recycling effort, and components were replaced as necessary when required. The horizontal focusing, for example, was changed through the installation of new mirrors to provide a 100-μm focus in one of the side branches of the new beamline.

Construction of the beamline proceeded rapidly following the shutdown of Beamline 9.0.1 in March 1998. The new U10 undulator was installed during the June 1998 machine shutdown, and beam was passed into the new beamline at the end of this shutdown. Commissioning and optics scrubbing continued through mid-July, when the beamline became ready for use. New endstations provided by the SFI funds are now permanently installed on two branchlines. A third branchline provides access for additional experiments.

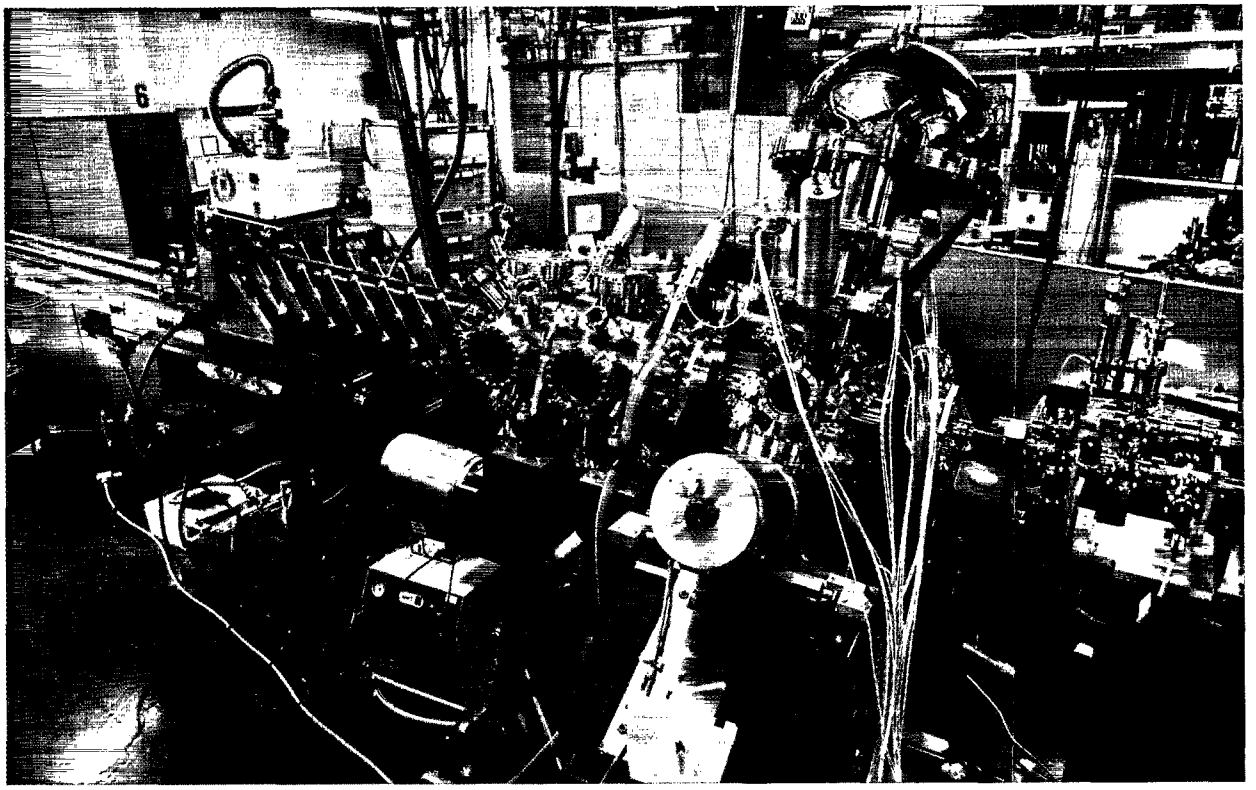

Figure 1

The high energy resolution spectroscopy (HERS) endstation uses undulator light from Beamline 10.0.1 for angle-resolved photoemission experiments on highly correlated electron systems.

High Energy Resolution Spectrometer (HERS)

A collaborative effort between members of the SSG and the Mechanical Engineering Group was undertaken to develop a high energy resolution spectrometer (HERS, Figure 1) for angle-resolved photoemission experiments on highly correlated electron systems. The spokesperson for this project is Z.X. Shen of Stanford University. The heart of the experiment station is a state-of-the-art, angle-resolved electron energy analyzer (Scienta SES-200) mounted on a chamber that rotates about the photon-beam axis. The combination of an analyzer with an angle-resolving mode, a high-precision low-temperature sample goniometer, and the use of Beamline 10.0.1 allows photoemission experiments with ultrahigh energy and momentum resolution. A high-efficiency electron-spin detector is also under construction and will allow determination of all three components of electron spin with high energy resolution, comparable to kT.

Highly correlated electron systems, such as those in the d- and f-band materials, offer both intellectual challenges in physics and prospects for novel materials applications. Such systems, which include high-temperature superconductors as well as heavy fermion and Kondo systems, are not adequately described by either atomic physics or one-electron band theory. Photoemission is an ideal tool to study highly correlated electron systems and has the potential to have a major impact on our understanding of these materials.

High-Resolution Atomic and Molecular Electron Spectrometer (HiRAMES)

The high-resolution atomic and molecular electron spectrometer (HiRAMES, pronounced "higher aims"), built by Professor Nora Berrah of Western Michigan University with funding from the SFI, was designed and constructed with the assistance of collaborator John Bozek of the SSG. The HiRAMES endstation was designed to study electronic processes in atoms and molecules in the greatest detail. The complexities of electronic structure in atoms and molecules are often only made clear when highly differential spectra are obtained.

The endstation (Figure 2) was constructed with a state-of-the-art Scienta SES-200 electron energy analyzer mounted on a chamber that rotates about the photon-beam axis. A rotatable seal maintains the vacuum integrity of the system when it is rotating, allowing quick changes in the angle of the spectrometer. Gaseous samples are introduced into a gas cell mounted on the end of the electron lens. The cell has differentially pumped openings for the photon beam and a slit that allows electrons to leave the cell in the direction of the analyzer. Sample pressures as high as 10^{-5} Torr are isolated from the ultrahigh vacuum requirements of the beamline by windowless differential pumping. Provisions have also been made for other sample introduction systems that will extend the utility of the endstation to systems other than simple gases.

The high electron-energy resolution and angular selectivity of the HiRAMES spectrometer, together with the high flux and spectral resolution of undulator Beamline 10.0.1, is utilized to measure spectra that are highly differential in excitation energy, emission energy, de-excitation energy, and angle. These spectra help to provide a clear understanding of the photoionization processes in atoms and molecules. Knowledge gained from such studies increases our understanding of electronic structure and photoionization in general.

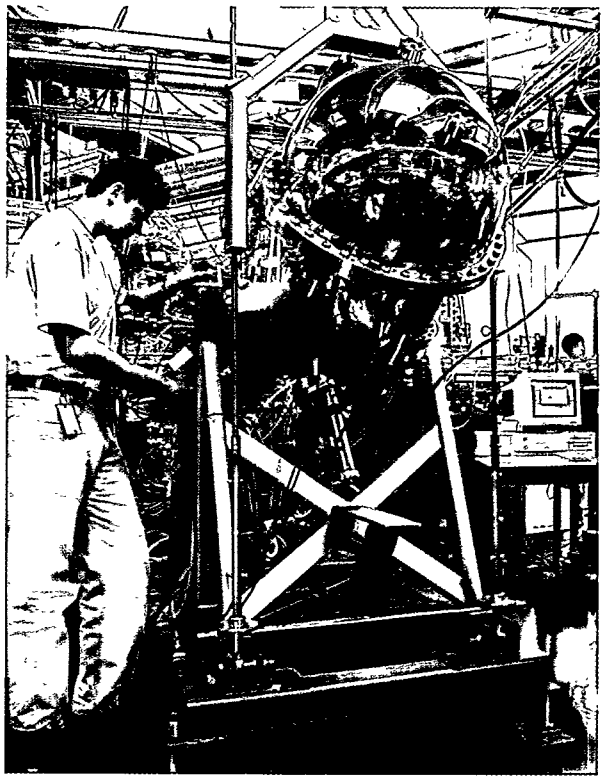

Figure 2

The high-resolution atomic and molecular electron spectrometer (HiRAMES), also on Beamline 10.0.1, was designed to study the complexities of electronic structure in atoms and molecules.

USER SERVICES

Gary Krebs

User Services Group Leader

The User Services Group's main function is to provide an interface between the user community and the ALS facility. To better serve the users of the ALS, the group was reorganized this year into three sections: User Services Administration, Beamline Coordination, and Technical Information.

Conveniently located in the new User Services Office on the ALS mezzanine (Figure 1), User Services Administration assists users in every way possible. Administration section members coordinate all requests for independent-investigator beamtime, provide new-user orientation, and assist throughout each user's run. They also assist users in obtaining lodging in the new ALS user apartments (Figure 2). This section is led by Ruth Pepe and includes Sharon Fujimura, Bernadette Dixon, and Jane Tanamachi (Figure 3).

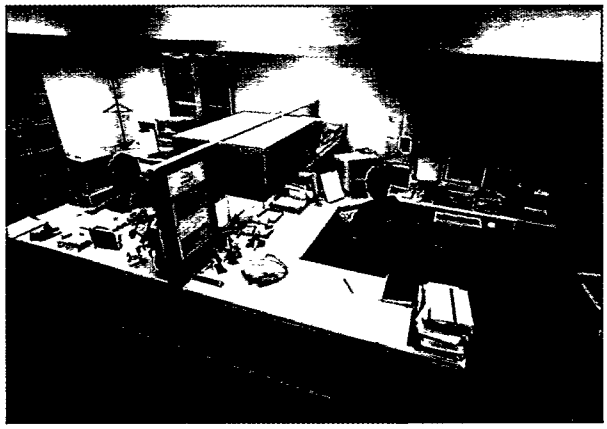

Figure 1

The ALS User Services Office has moved to its new quarters on the mezzanine of the ALS building.

Figure 2

The new ALS user apartments, located along the Berkeley Lab shuttle bus route, provide short- and long-term housing for users.

Our Beamline Coordination section assists users with shipping and receiving and various other on-the-floor needs. Section members help with experiment setup and make sure users' equipment meets ALS safety standards. They serve as liaisons between users and available ALS and Berkeley Lab resources. Led by Ray Thatcher, the section includes Gary Giangrasso and Cheryl Hauck.

The Technical Information section is responsible for the document you are reading and many others. Besides publishing the annual ALS Activity Report, this section compiles user results in an annual Compendium of User Abstracts and Technical Reports. Both publications are available in hard copy and on our World Wide Web site. The Technical Information section also publishes special reports, writes proposals for new initiatives, creates illustrations and graphic designs, maintains the ALS Web site, writes and edits the electronic ALSNews, and manages a multifaceted outreach program to the local community. This section is led by Art Robinson and includes Annette Greiner, Elizabeth Moxon, Greg Vierra, and Lori Tamura.

One of the priorities for User Services this year has been to make full use of the capabilities of the World Wide Web to make information available to users and to permit electronic submittal of forms. Thanks to a cooperative effort across User Services sections, we now have a suite of interactive pages, which can be reached through the main ALS Web site.

Figure 3

The staff of the ALS User Services Office, pictured at the new user work area on the ALS mezzanine, includes (left to right) Bernadette Dixon, Jane Tanamachi, Ruth Pepe, and Sharon Fujimura.

World Wide Web Resources

Main ALS Web site	http://www-als.lbl.gov/
1996/97 Activity Report	http://www-als.lbl.gov/als/actrep/
1997 Compendium of User Abstracts and Technical Reports	http://alspubs.lbl.gov/compendium/
ALSNews	http://www-als.lbl.gov/als/als_news/
Instructions for Submitting a Beamtime Proposal	http://www-als.lbl.gov/als/quickguide/becomealsuser.html
On-Line New User Registration	http://www-als.lbl.gov/als/quickguide/comingtoals.html

Special Events

Workshop on Scientific Directions at the ALS

In March 1998, the ALS held a workshop to identify the elements of the most compelling scientific program for the facility and to make recommendations for the implementation of that program. Internationally recognized scientists in each of the many disciplines that make up the spectrum of ALS research were invited to convene in Berkeley. Working in plenary sessions and in smaller groups organized by specialty, the participants created a road map for ALS science well into the new millennium.

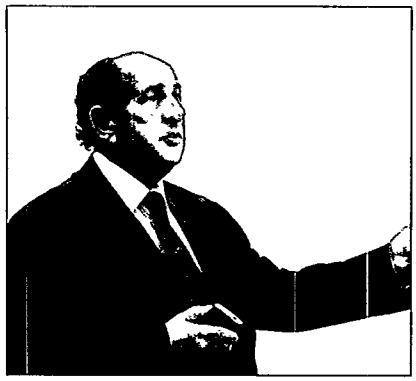

Yves Petroff, Director-General of the European Synchrotron Radiation Facility, chaired the workshop. He began the morning session with a European perspective on synchrotron radiation research.

Patricia Dehmer, head of the U.S. Department of Energy's Office of Basic Energy Sciences, gave the formal charge to the workshop: to determine the most compelling research topics within each specialty, assess how the ALS can be used to further that research, and determine what beamlines and instrumentation will be needed.

Z.X. Shen of Stanford University presented recent work in high-temperature superconductivity.

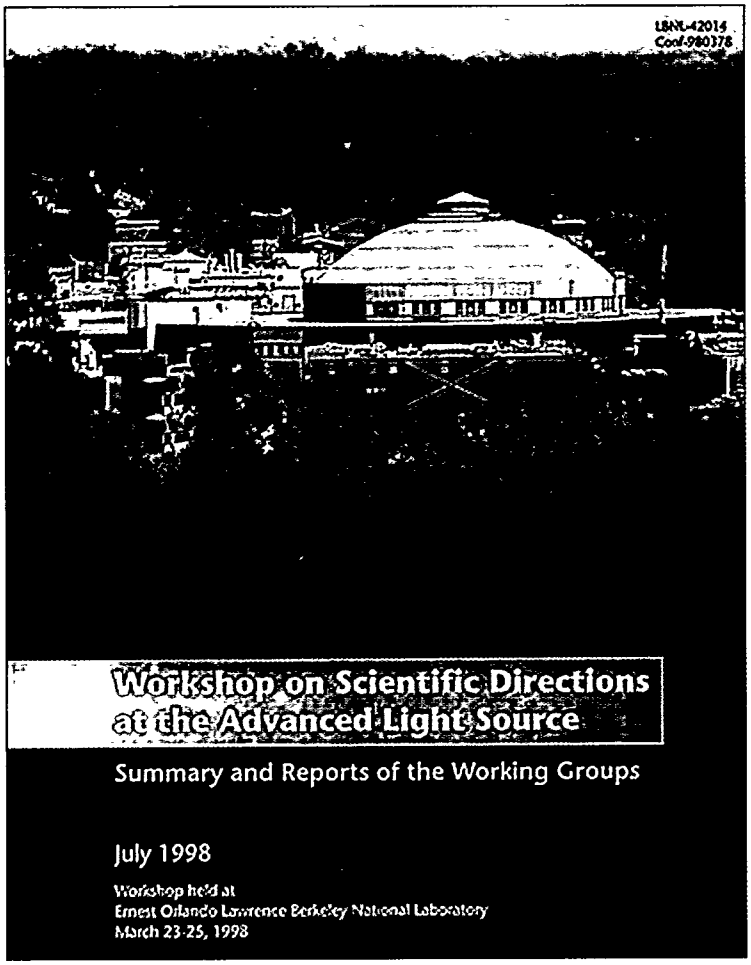

Participants prepared chapters for the workshop report in informal breakout sessions.

VUV-XII

The 12th International Conference on Vacuum Ultraviolet Radiation Physics was held August 3–7, 1998, in San Francisco. Hundreds of scientists from around the world gathered at the Grand Hyatt Hotel on Union Square. Hosted by the ALS, the triennial conference featured more than 500 poster presentations and 45 invited speakers. The scope of the conference included all theoretical and experimental studies of the interaction of ultraviolet and soft x-ray radiation with matter over a photon energy range of 5 eV to several keV.

As host of this major international meeting, the ALS offered tours to scientists from around the world. Here, visitors chat with ALS users on the experiment floor near Beamline 7.0.

During the tours, curious guests filled the walkways inside the storage-ring shield wall. The scientists got a close-up view of the vacuum chamber as well as the magnet lattice and insertion devices that might illuminate their next experiment.

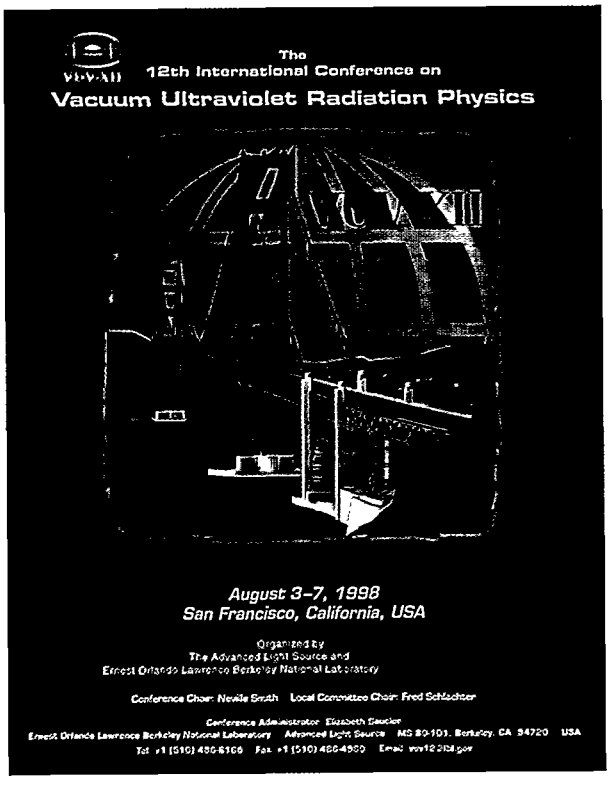

Guests enjoyed good food and stimulating conversation at the post-tour reception, held on the ALS patio.

VUV-XII Conference Chair Neville Smith handed over the ceremonial gavel to the Interim Chair for VUV-XIII, Giorgio Margaritondo, representing Italy's ELETTRA Synchrotron Light Source.

ALS Users' Association Annual Meeting

The 1997 meeting of the ALS Users' Association, October 13–14, attracted more than 225 users, staff, vendors, and other participants. The meeting included a full complement of talks on scientific results, new beamlines, and opportunities for research.

Cathie Magowan explained her results to fellow user Raul Beguiristain.

ALS users Jeffrey Kortright and Uwe Bergmann shared thoughts at the poster session.

Patricia Dehmer, head of the U.S. Department of Energy's Office of Basic Energy Sciences, discussed high-resolution atomic, molecular, and optical physics with researcher Nora Berrah. At the meeting, Dehmer spoke about the Basic Energy Sciences Advisory Committee Report on Synchrotron Radiation Sources and Science and held a forum with ALS users.

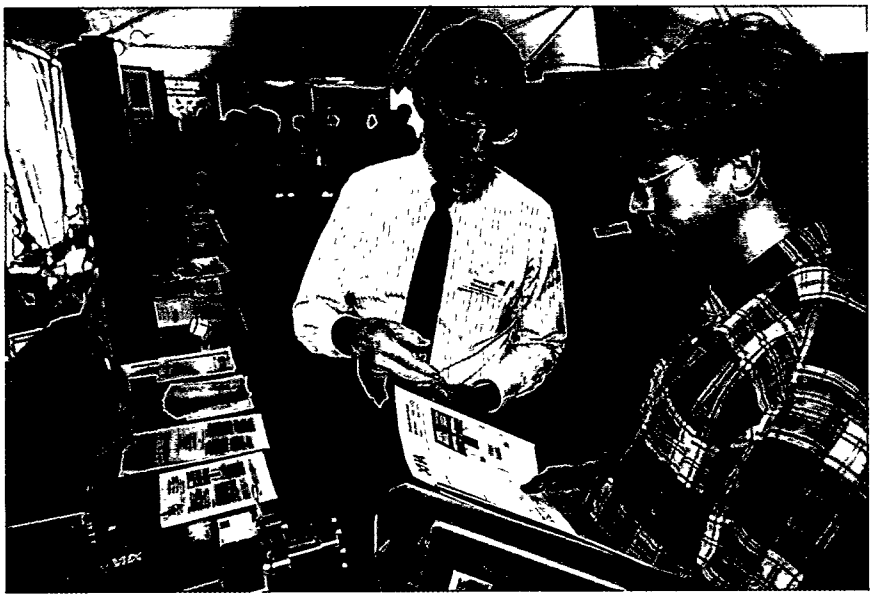

Vendor exhibits were held in conjunction with the poster session, giving users the opportunity to study the latest developments in instrumentation.

Dedication of Macromolecular Crystallography Facility

On September 19, 1997, the Macromolecular Crystallography Facility (MCF) was officially dedicated as a national user facility. The event celebrated the completion of Beamline 5.0.2 and the taking of the MCF's first diffraction patterns. Funding for this initial beamline and for two additional branchlines now under construction has been contributed by the Office of Biological and Environmental Research of the U.S. Department of Energy; Berkeley Lab; the University of California, Berkeley; Roche Bioscience; Amgen; the Genetics Institute; the University of California, San Francisco; Lawrence Livermore National Laboratory; and the National Institutes of Health.

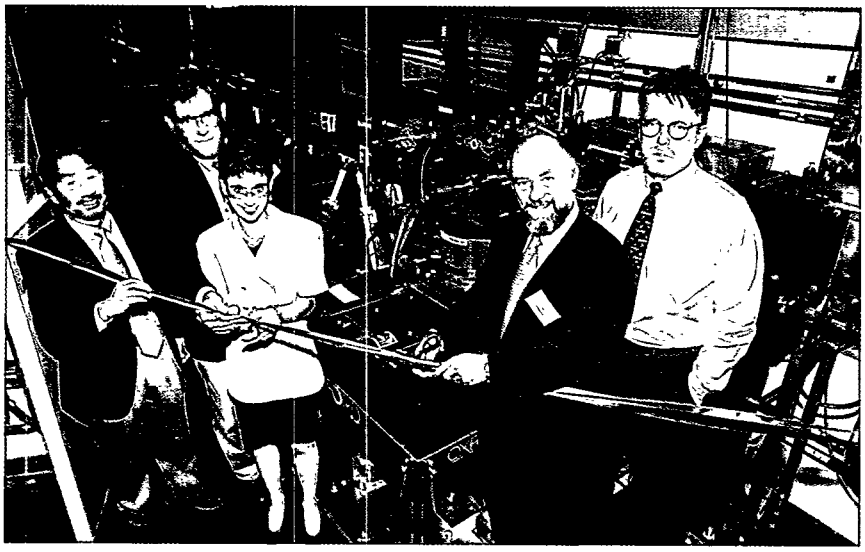

Guests at the ribbon cutting included (left to right) researcher Sung-Hou Kim, then-ALS-Director Brian Kincaid, Michelle Broido of the DOE Office of Biological and Environmental Research, Deputy Berkeley Lab Director Pier Oddone, and MCF Director Thomas Earnest.

Oddone addressed the overflow crowd in front of the Beamline 5.0.2 hutch.

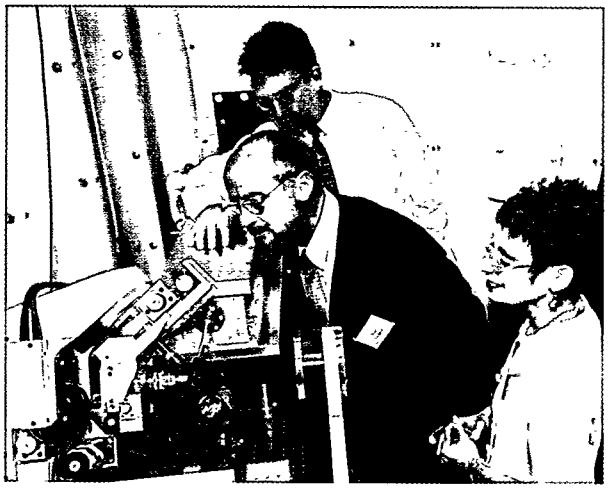

Broido and Oddone inspected the endstation as Earnest pointed out key features .

Distinguished Visitors

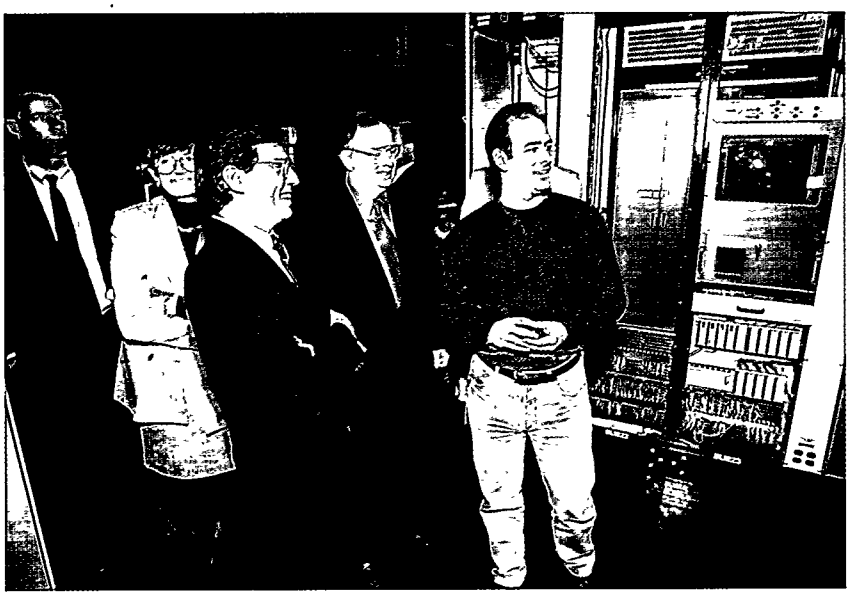

In December 1997, Secretary of Energy Federico Peña (third from left) visited the ALS. He was accompanied by Martha Krebs (second from left), Director of the U.S. Department of Energy's Office of Science, and Berkeley Lab Director Charles Shank (fourth from left). Ken Goldberg (right), of the Center for X-Ray Optics, showed the secretary around Beamline 12.0.1.2, where Goldberg makes interferometric wavefront measurements of optics for extreme ultraviolet lithography.

As the ALS user community grows, links are being forged with industry. In May 1998, the ALS played host to one of its largest industrial tour groups—Sun Microsystems managers from around the world.

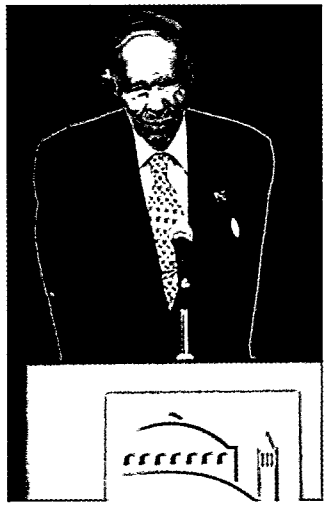

Glenn Seaborg, Nobel Laureate and Associate Laboratory Director At Large, spoke to the Sun Microsystems tour participants.

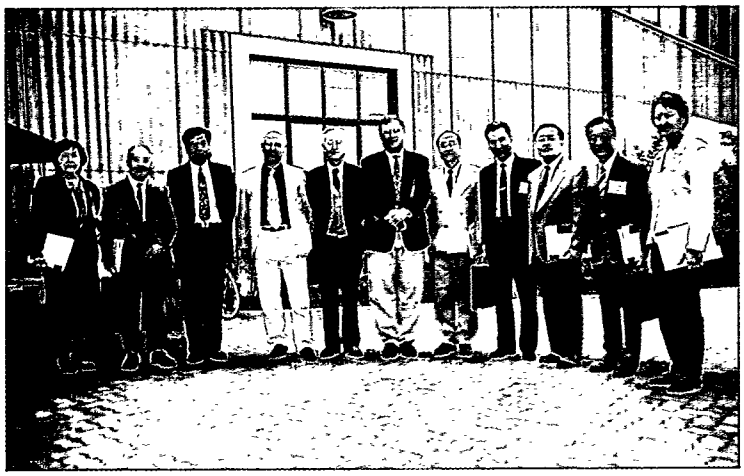

A delegation from the Chinese Academy of Sciences also visited the ALS in May 1998. The group came to the U.S. to attend meetings with representatives of the U.S. National Academy of Sciences and the U.S. energy industry.

Open House

Good fortune provided a splendid, sunny day in October 1997 for the second Berkeley Lab Open House, and the public turned out by the busload to take it all in. More than 5000 enthusiastic visitors enjoyed a day of discovery and exploration. Having established itself as a major attraction at the 1995 Open House, the ALS again found itself a center of attention. The day was a tremendous success, thanks to the help of ALS users and CXRO and ALS staff, including more than 100 generous volunteers.

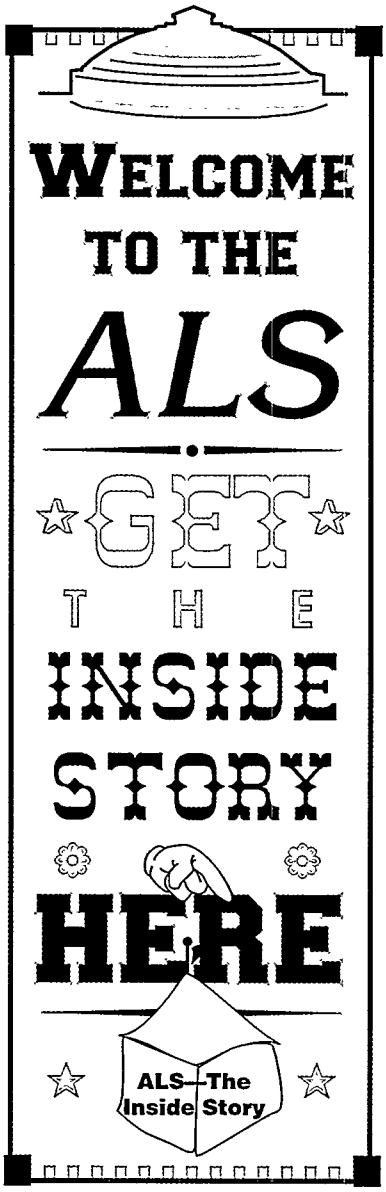

The patterns of magnetic fields interacting with the electrons in an old computer monitor gave insight into how electrons in the ALS can be controlled by magnets.

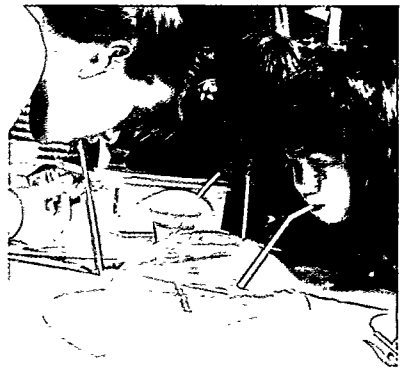

Young visitors were dazzled by interference effects in thin films of soap.

Visitors to the ALS stopped by the control room to see how the ALS is operated.

Educational Outreach

The ALS strives to maintain strong links with the local educational community as well as with students and teachers around the world. Through our summer programs, students and teachers from nearby schools come to learn by observing real science in action. ALS staff also participate in the annual Daughters and Sons to Work Day as well as the Berkeley Lab Science Exploration Camp. As part of the UC Berkeley academic community, the ALS participates in the yearly Cal Day open house. On a worldwide scale, the Web magazine MicroWorlds reaches students and teachers as far away as the former Soviet Union.

On Cal Day, the ALS opened its doors to UC Berkeley alumni, friends, and prospective students. Here, Andreas Stonas of Berkeley Lab's Materials Sciences Division conducts a beamline tour.

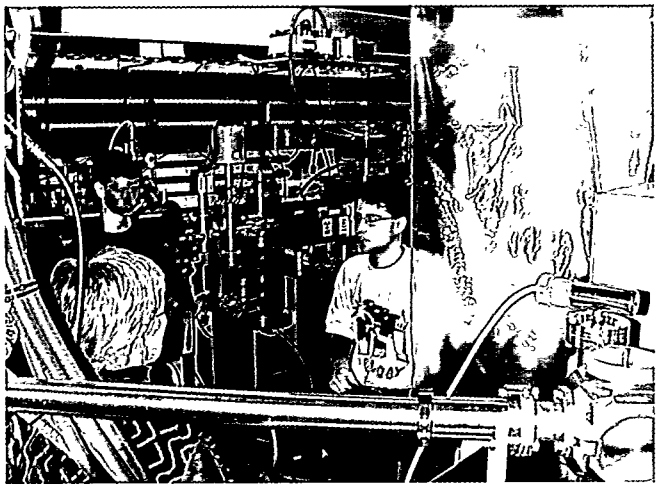

Summer student Dana Nelson worked with the ALS Technical Information Section, deveoping a new component for the MicroWorlds educational Web site. Here, Dana (left) presents her accomplishments at the annual student poster session.

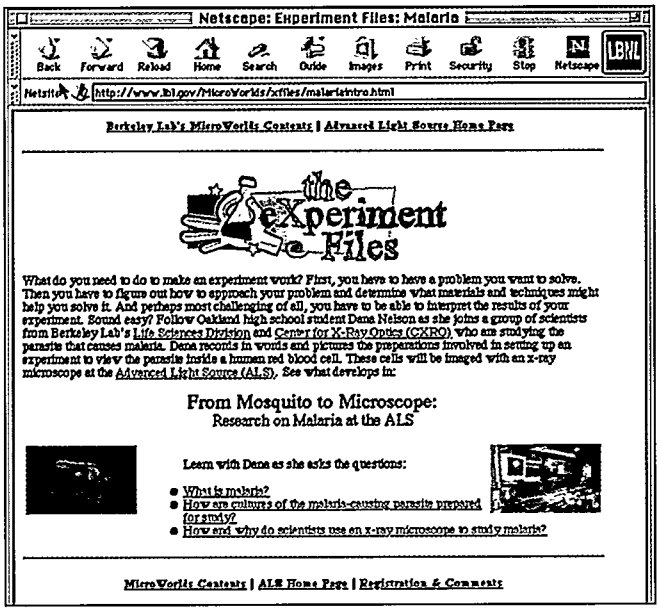

Dana created the eXperiment Files, which gives a student's-eye view of research being done at the ALS. The first article for this new section of MicroWorlds focused on malaria studies conducted at the x-ray microscope on Beamline 6.1.2.

ALS Advisory Panels 1997/98

Scientific Advisory Committee

Advises Berkeley Lab and ALS management on issues relating to ALS operations, resource allocation, strategic planning, and Participating Research Team proposals and performance.

1997

Daniel Chemla, Berkeley Lab

Chien-Te Chen, Synchrotron Radiation Research Center, Taiwan

Roger Falcone, University of California, Berkeley

Keith O. Hodgson, Stanford Synchrotron Radiation Laboratory

Janos Kirz, State University of New York at Stony Brook

Robert C. McDonald, Intel Corporation

David A. Shirley, Berkeley Lab

Neville V. Smith, Berkeley Lab (*ex officio*)

Joachim Stöhr, IBM Almaden Research Center (Chair)

Robert Stroud, University of California, San Francisco

1998

Gordon E. Brown, Jr., Stanford University

Daniel Chemla, Berkeley Lab

Chien-Te Chen, Synchrotron Radiation Research Center, Taiwan

Roger Falcone, University of California, Berkeley

Janos Kirz, State University of New York at Stony Brook

David A. Shirley, Berkeley Lab

Neville V. Smith, Berkeley Lab (*ex officio*)

Joachim Stöhr, IBM Almaden Research Center (Chair)

Robert Stroud, University of California, San Francisco

Baylor Triplett, Intel Corporation

Science Policy Board

Advises the Berkeley Lab Director on major policy issues concerning the ALS.

Robert J. Birgeneau, Massachusetts Institute of Technology

William Brinkman, Lucent Technologies/Bell Laboratories

John Carruthers, Intel Corporation

Chien-Te Chen, Synchrotron Radiation Research Center, Taiwan

Peter Eisenberger, Columbia Earth Institute

Paul Fleury, University of New Mexico

Franz J. Himpsel, University of Wisconsin-Madison

Yuan T. Lee, Academia Sinica, Taiwan

Users' Executive Committee

Elected by the members of the Advanced Light Source Users' Association to act as the official voice of the user community in its interactions with ALS management.

1997

Jeffrey Bokor, University of California, Berkeley

Thomas Earnest, Berkeley Lab

Adam P. Hitchcock, McMaster University

Duane H. Jaecks, University of Nebraska-Lincoln

Stephen D. Kevan, University of Oregon

Bengt Jörgen Larsson, Berkeley Lab

Werner Meyer-Ilse (Vice Chair), Berkeley Lab

Eli Rotenberg, Berkeley Lab

Mahash Samant, IBM Almaden Research Center

Arthur Suits, Berkeley Lab

Louis J. Terminello (Chair), Lawrence Livermore National Laboratory

1998

Nora Berrah, Western Michigan University

Thomas Earnest, Berkeley Lab

Charles S. Fadley, University of California, Davis

David L. Hansen, University of Nevada, Las Vegas

Adam P. Hitchcock, McMaster University

Duane H. Jaecks, University of Nebraska-Lincoln

Stephen D. Kevan (Vice Chair), University of Oregon

Werner Meyer-Ilse (Chair), Berkeley Lab

Arthur Suits, Berkeley Lab

Louis J. Terminello, Lawrence Livermore National Laboratory

James H. Underwood, Berkeley Lab

ALS Staff 1997/98*

Management

D. Chemla
B. Feinberg
B. Kincaid
N. Smith

Accelerator Physics

J. Byrd
W. Decking
S. DeSantis
A. Jackson
R. Keller
C. Kim
D. Massoletti
H. Nishimura
G. Portmann
D. Robin
H. Zyngier

Administrative Support

T. Aitkens
M. Barry
K. Gonzalez
J. Minton
W. Mitchell
R. Nelson
B. Phillips
E. Saucier
J. Toby
L. Williams

Electrical Engineering

B. Bailey
M. Balagot
K. Baptiste
B. Bingham
A. Biocca
J. Bishop
K. Bolin
W. Brown, Jr.
J. Burch
R. Candelario
P. Casey
M. Chin
J. DeVries
J. Elkins
A. Lindner
C.C. Lo
J. Meng
K. Moeller
P. Molinari
R. Mueller
F. Ottens
D. Peterson
A. Ritchie
A. Robb
S. Rogoff
B. Samuelson
D. Sandler
K. Scott
M. Fahmie
K. Fowler
J. Gardner
R. Gassaway
R. Gervasoni
A. Geyer
J. Gregor
P. Himmel
J. Hinkson
S. Jacobson
J. Johnston
J. Julian
R. Kerns
A. Kruser
H. Lancaster
L. Shalz
J. Spring
R. Steele
G. Stover
S. Stricklin
M. Szajbler
B. Taylor
C. Timossi
J. Velasco
K. Woolfe
E. Wong
R. Ybarra
E. Yee
J. Zelver

Environment, Health & Safety

K. Heinzelman
G. Perdue

Experimental Systems

S. Anders
S. Cerasari
R. Celestre
C.H. Chang
B. Cho
A. Cossy
K. Eun
A. Garcia
E. Glover
F. Gozzo
E. Harvey
P. Heimann
C. Hirschmugl
M. Howells
S. Irick
S. Lindaas
A. Lindenberg
S. Locklin
A. MacDowell
V. Martynov
W. McKinney
H. Padmore
J. Patel
S.-Y. Rah
T. Renner
S. Sasaki
S. Seal
J. Spence
T. Stammler
A. Warwick
A. Young

Mechanical Engineering

T. Akins
J. Akre
D. Anderson
N. Andresen
G. Andronaco
R. Armstrong
W. Baldock
D. Baum
J. Bonifas
D. Calais
A. Catalano
D. Colomb
J. Comins
C. Corradi
C. Cummings
D. Davis
M. Decool
R. DeMarco
D. DiGennaro
T. Downs
R. Duarte
K. Franck
W. Gath
A. Gavidia
B. Gee
D. Gibson
J. Guigli
K. Halbach
T. Henderson
E. Hoyer
D. Hull
D. Humphries
D. Jones
N. Kellogg
S. Klingler
M. Knolls
C. Knopf
M. Kritscher
T. Lauritzen
B. Lew
A. Lim
R. Low
B. MacDonell
S. Marks
P. McGowan
P. McKean
H. Meyer
Y. Minimahara
V. Moroz
G. Morrison
D. Munson
F. Ochoa
W. Oglesby
A. Paterson
R. Patton
P. Piperski
D. Plate
K. Rex
B. Rude
R. Schlueter
N. Searls
K. Sihler
M. Stuart
J. Thomson
G.W. Thur
W. Wong
R. Zager
F. Zucca

* This is a cumulative list of all those who worked at the ALS at any time between mid-1997 and mid-1998. The number of ALS employees at any one time during this period averaged 170.

Operations

D. Bentsen
T. Byrne
S. Daly
O. Jones
J. McDonald
R. Miller
M. Monroy
J. Pusina
T. Scarvie
M. Wolfe

Planning and Development

J. Harkins
J. Krupnick
J. Zelver

Procedure Center

R. Jones

Quality Assurance

E. Lampo

Scientific Support

G. Ackerman
J. Bozek
Z. Hasan
C. Heske
Z. Hussain
A. Johnson
R. Kawakami
S. Kellar
M. Martin
S. McHugo
G. Meigs
E. Moler
R. Perera
E. Rotenberg
A. Schlachter
X. Zhou
X.J. Zhou

User Services

J. Cross
R. Decker
B. Dixon
D. Dixon
S. Fujimura
G. Giangrasso
A. Greiner
C. Hauck
G. Krebs
L. Moxon
R. Pepe
A. Robinson
M. Sibony
R. Thatcher
G. Vierra

Facts and Figures

Using the Advanced Light Source

The ALS, a Department of Energy national user facility, welcomes researchers from universities, industry, and government laboratories. Qualified users have access either as members of participating research teams (PRTs) or as independent investigators. PRTs (groups of researchers with related interests from one or more institutions) construct and operate beamlines and have primary responsibility for experiment endstation equipment. They are entitled to a certain percentage of their beamline's operating time according to the resources contributed by the PRT. Through a proposal process, the remaining beamtime is granted to independent investigators, who may provide their own endstation or negotiate access to a PRT-owned endstation.

The ALS does not charge users for beam access if their research is nonproprietary. Users performing proprietary research are charged a fee based on cost recovery for ALS usage. All users are responsible for the day-to-day costs of research (e.g., supplies, phone calls, technical support).

The nominal operating energy of the ALS storage ring is 1.9 GeV, although it can run from 1.0 to 1.9 GeV, allowing flexibility for user operations. At 1.9 GeV, the normal maximum operating current is 400 mA in multibunch operation. The spectral range of undulator and wiggler beamlines extends from photon energies of roughly 5 eV to 21 keV. Bend magnets produce radiation from the infrared to about 12 keV.

The ALS is capable of accommodating approximately 46 beamlines and more than 100 endstations. The first user beamlines began operation in October 1993, and there were 27 operating beamlines, with several more under construction, by March 1999.

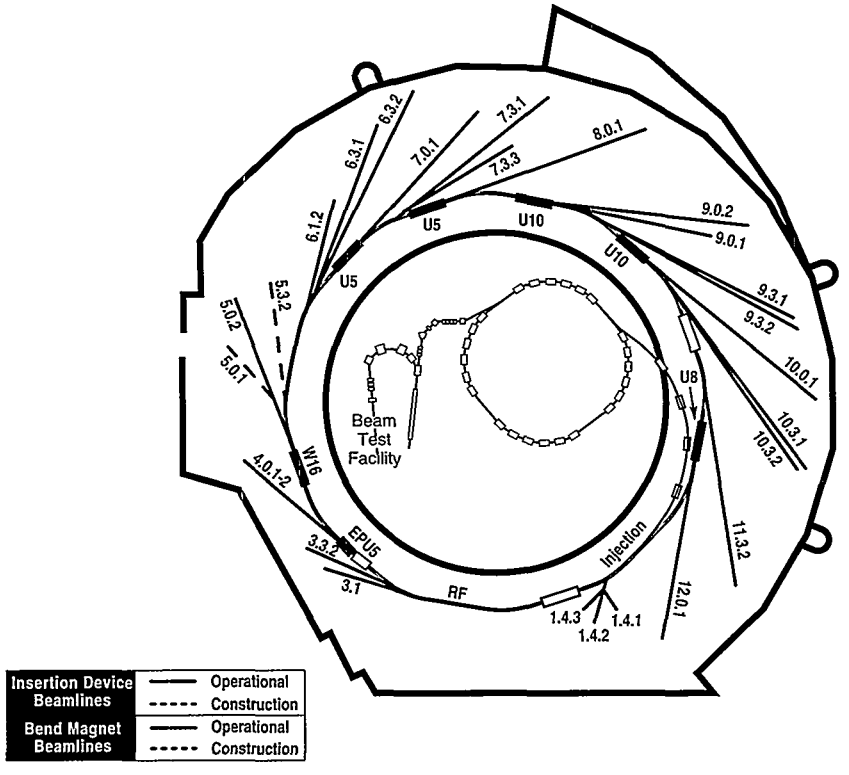

ALS Beamlines*

Beamline	Source	Areas of Research	Energy Range	Monochromator	Available
BTF	ALS linac	Beam Test Facility	50 MeV (electrons)	None	Now
1.4.1	Bend magnet	Ultraviolet photoluminescence	1.6–6.2 eV	None	Now
1.4.2	Bend magnet	Visible and infrared Fourier transform spectroscopy	0.006–3 eV	None	Now
1.4.3	Bend magnet	Infrared spectromicroscopy	0.05–1 eV	None	Now
3.1	Bend magnet	Diagnostic beamline	200–280 eV	Mirror/filter	Now
3.3.2	Bend magnet	Deep-etch x-ray lithography (LIGA)	3–12 keV	White light, four crystal	Now
4.0.1	EPU5 Elliptical polarization undulator	Magnetic spectroscopy	100–1500 eV	PGM	Now
4.0.2	EPU7.5 Elliptical polarization undulator	Magnetic microscopy	100–1500 eV	SGM	2000
5.0.1	W16 Wiggler	Monochromatic protein crystallography	5–21 keV	Curved crystal	1999
5.0.2	W16 Wiggler	Multiple-wavelength (MAD) and monochromatic protein crystallography	5–21 keV	Double crystal	Now
5.3.2	Bend magnet	STXM for polymer research	150–650 eV	SGM	1999
6.1.2	Bend magnet	High-resolution zone-plate microscopy	500–800 eV	Zone-plate linear	Now
6.3.1	Bend magnet	Calibration and standards, EUV/soft x-ray optics testing, solid-state chemistry	500–2000 eV	VLS-PGM	Now
6.3.2	Bend magnet	Calibration and standards; EUV optics testing; atomic, molecular, and materials science	50–1300 eV	VLS-PGM	Now
7.0.1	U5 Undulator	Surface and materials science, spectromicroscopy, spin resolution, photon-polarization dichroism	80–3000 eV	SGM	Now
7.3.1.1	Bend magnet	Magnetic microscopy, spectromicroscopy	260–1500 eV	SGM	Now
7.3.1.2	Bend magnet	Surface and materials science, micro x-ray photoelectron spectroscopy	260–1500 eV	SGM	Now
7.3.3	Bend magnet	Micro x-ray diffraction, micro x-ray absorption spectroscopy	0.1–12 keV	White light, four crystal	Now
8.0.1	U5 Undulator	Surface and materials science, spectromicroscopy, imaging photoelectron spectroscopy	80–3000 eV	SGM	Now
9.0.1	U10 Undulator	Coherent optics experiments	8–1500 eV	SGM	Now
9.0.2.1	U10 Undulator	Chemical reaction dynamics, photochemistry	8–1500 eV	None	Now
9.0.2.2	U10 Undulator	High-resolution photoelectron and photoionization spectroscopy	8–1500 eV	Off-plane Eagle	Now
9.3.1	Bend magnet	Atomic, molecular, and materials science	2.2–6 keV	Double crystal	Now
9.3.2	Bend magnet	Chemical and materials science, circular dichroism, spin resolution	30–1500 eV	SGM	Now
10.0.1	U10 Undulator	High-resolution atomic, molecular, and optical physics; photoemission of highly correlated materials	12–1500 eV	SGM	Now
10.3.1	Bend magnet	X-ray fluorescence microprobe	3–20 keV	White light, multilayer	Now
10.3.2	Bend magnet	X-ray optics development, materials science	3–20 keV	White light, four crystal	Now
11.3.2	Bend magnet	Inspection of EUV lithography masks	50–1000 eV	VLS-PGM	Now
12.0.1.1	U8 Undulator	Surface and materials science, spectromicroscopy	30–1900 eV	VLS-PGM	Now
12.0.1.2	U8 Undulator	EUV lithography optics testing, interferometry	30–1900 eV	VLS-PGM	Now

**This table is valid as of March 1999. The most current information on ALS beamlines is available on the World Wide Web (http://www-als.lbl.gov/als/als_users_bl/bl_table.html).*

ALS Storage Ring Parameters

Parameter	Value
Beam particle	electron
Beam energy	1.0–1.9 GeV
Injection energy	1.0–1.5 GeV
Beam current multibunch mode two-bunch mode	 400 mA 2 × 25 mA
Filling pattern (multibunch mode)	288 bunches (variable)
Bunch spacing multibunch mode two-bunch mode	 2 ns 328 ns
Circumference	196.8 m
Number of straight sections	12
Radio frequency	500 MHz
Beam size in straight sections, rms	250 microns horiz. × 20 microns vert.
Natural emittance	6 nm-rad at 1.9 GeV
Energy spread ($\Delta E/E$, rms)	8×10^{-4} at 1.9 GeV

Parameter	Value at 1.5 GeV	Value at 1.9 GeV
Beam lifetime multibunch mode* two-bunch mode	 ~4.0 hours at 400 mA not used	 ~4.0 hours at 400 mA ~0.5 hours at 40 mA
Horizontal emittance	4 nm-rad	6 nm-rad
Vertical emittance**	2.0 nm-rad	0.1 nm-rad

**In multibunch mode, the storage ring is typically filled every four hours or as requested by our users.*
***Vertical emittance can be deliberately increased to improve beam lifetime.*

ALS Insertion Device Parameters

Device	Beamline	Status	Energy Range (at 1.5 GeV)	Energy Range (at 1.9 GeV)	Period Length	No. of Periods	Operating Gap Range	Peak Effective Field Range
U5 Undulator	8.0	Operational	50–1900 eV	80–3000 eV	5.0 cm	89	1.4–4.5 cm	0.85–0.10 T
U5 Undulator	7.0	Operational	50–1900 eV	80–3000 eV	5.0 cm	89	1.4–4.5 cm	0.85–0.10 T
U8 Undulator	12.0	Operational	18–1200 eV	30–1900 eV	8.0 cm	55	2.5–8.3 cm	0.80–0.07 T
U10 Undulator	9.0	Operational	5–950 eV	8–1500 eV	10.0 cm	43	2.4–11.6 cm	0.98–0.05 T
U10 Undulator	10.0	Operational	8–950 eV	12–1500 eV	10.0 cm	43	2.4–11.6 cm	0.80–0.05 T
EPU5 Elliptical Polarization Undulator	4.0	Operational	60–1000 eV*	100–1500 eV*	5.0 cm	37	1.45–5.5 cm	0.79–0.10 T (vertical field) 0.54–0.10 T (horizontal field)
W16 Wiggler	5.0	Operational	5–13 keV	5–21 keV	16.0 cm	19	1.4–18.0 cm	0.03–2.1 T

** Elliptical polarization mode*